# Design Methodology for Engineering Multifunctional Mesoscale Robots

**Thèse N° 7265**

**Présentée le 25 novembre 2019**

**à la Faculté des sciences et techniques de l'ingénieur**
**Laboratoire de robotique reconfigurable**
**Programme doctoral en robotique, contrôle et systèmes intelligents**

**pour l'obtention du grade de Docteur ès Sciences**

**par**

**Zhenishbek ZHAKYPOV**

**Acceptée sur proposition du jury**

**Prof. H. Shea, président du jury**
**Prof. J. Paik, directrice de thèse**
**Prof. M. Sitti, rapporteur**
**Prof. M. Kovac, rapporteur**
**Prof. S. Coros, rapporteur**

**2019**

ÉCOLE POLYTECHNIQUE
FÉDÉRALE DE LAUSANNE

Perhaps, we begin to *crawl* toward our dreams.
It takes courage to *walk* across countless obstacles
and even a stronger will to *take the leap* of faith.
©

To my parents...

# Acknowledgements

I would like to express my sincere gratitude to my advisor Prof. Jamie Paik for welcoming me to Reconfigurable Robotics Laboratory, seeing potential in me, supporting my efforts and vision, and guiding me through my PhD studies. Her leadership and unwavering enthusiasm for high standards by never settling for less, truly inspired me and encouraged my professional and personal development.

Besides my advisor, I would like to thank the rest of my thesis committee: Prof. Herbert Shea, Prof. Metin Sitti, Prof. Mirko Kovac, and Prof. Stelian Coros for their insightful comments, questions and encouragement that greatly improved my dissertation.

I am grateful to number of friends and colleagues who made my PhD life joyful and memorable. I very much thank Harshal for his friendship and great support in various challenging situations, for delicious Indian food and fascinating philosophical discussions. I thank Matt for memorable hiking journeys together and for sharing his wisdom. I thank RRL family for all the fun and hard times working shoulder to shoulder, keeping the lab running and productive. Many of you inspired me and stimulated my development.

Most of all, I am indebted to my family. I would like to thank my wife Ainura and my wonderful daughter Aliya for enormous support, care, joy and understanding throughout my studies. I am grateful to my sisters Dilbara and Meerim for support and taking care of my mom, while I was away for seeking knowledge. I would like to express my deepest gratitude to my parents for guiding me to the path of education and science. My mom is the real hero behind the scenes, whose efforts in providing a good quality of life to me despite health and financial challenges is priceless.

*Bishkek, 23 August 2019* Z. Z.

# Abstract

In nature, small-scale organisms are capable of complex physical and collective behaviors to adapt to diverse tasks and environments by multifunctionality, multiplicity, and communication. Creating these abilities in mesoscale robotic systems, that measure from few hundreds of micrometers to few centimeters opens new opportunities to utilize them for several applications. They can be deployed for emergency mitigation in open and confined environments, for monitoring and exploration by sensing and gathering large data, emulating diverse insect biomechanics, studying complex collective behaviors and even for training new behaviours. Engineering this in mesoscale robotic systems without deterring miniaturization, multifunctionality and multiplicity poses significant challenges to both design and manufacturing of robotic hardware. The conventional design methods are impractical for constructing small-scale robots due to physical limitations of downsizing the conventional actuators and gears, whereas alternative compact actuation mechanisms are underdeveloped and not available off-the-shelf. In addition, assembly process of several small parts is difficult and expensive, requires meticulous and intensive labour, and currently, there is no automated process for building mesoscale robots from the ground up.

This grand challenge requires development of novel, unconventional design methodologies and fabrication techniques that allow for more efficient, customizable and fully automated mass-production processes, while addressing the miniaturization, as effortless as printed-circuit assembly. It necessitates robot discrete mechanical components and materials selectively composed automatically in layers by embedding functionality, including mechanisms and actuation. One prominent paradigm that explores this is smart composite manufacturing of robotic origami, also called *Robogami*. Robogami is foldable quasi-2D crease patterned composite robots and machines built from functional materials that can reconstruct various 3D shapes and mechanisms, theoretically, with infinite degrees-of-freedom (DoF). Composite robots inherit their functionality from active and passive material layers that allow for great design freedom for actuation and mechanism design being compact, minimal and multifunctional. However, active materials display highly complex behaviors that pose substantial challenges to their design. This is difficult to predict even for a single isotropic material, whereas anticipating their combined behavior in multi-layer, multimaterial structure is even more challenging due to layer interactions that can cause unpredictable impact on performance. Though multifunctionality and mass-producibility is the real potential of a robogami platform, the research has frequently focused on the development of robots with fixed functionality using specific materials and components without a clear, systematic design

methodology. Despite the material design freedom of robogami, a vast number of prototypes still utilize conventional servos and mechanisms, which limits functionality, miniaturization and assembly.

In this thesis our research goal is to develop, study and demonstrate multifunctional multi-robot systems in mesoscale. Particularly, our goal is to study and demonstrate terrestrial multi-locomotion and collective behaviours with mesoscale robots, similar to small-scale natural systems, by feeling the gap in the field. Our research objective is to develop, evaluate and demonstrate minimal, compact, variable power and efficient actuation mechanisms for multi-locomotion and rapid fabrication methods for robot multiplicity employing functional materials and composite design. In doing so, we intend to establish a comprehensive and systematic design methodology for designing multifunctional, mass-producible mesoscale robots for various applications. This dissertation first attempts to explore and answer the following key research question: *how to achieve variable power, efficient and compact actuation in mesoscale?* The relation between performance and physicality is significant for especially mesoscale robot design and is poorly studied. Our goal is to achieve high power, variable speed and high efficiency actuation in mesoscale. We attempt to address this by exploring unconventional active material-based actuation methods using shape memory alloy and composite material. In doing so, we quest of the following: *what are the compromises should be made between force, speed, efficiency and size of functional material-based actuators?* We investigate and demonstrate new, compact multimaterial actuators and mechanisms that possess power density superior to conventional motors, produce high speed and high force actuation and achieve multifunctionality when distributed and actuated selectively, all with minimal and compact forms and integrity.

While we study and develop design methods at the component level, like actuation, based on performance and physical features, we look for the same at the composite level or robotic system level. The next research question we attempt to address is *what, if any, is the general design methodology for constructing composite robots?*. To address this we formulate and analyze robogami design in terms of *mechanisms, geometry, functional components, materials* and *fabrication* to highlight their relation, potential and the challenges, as well as to structure the knowledge in the field. This leads to a systematic design approach that consolidates these critical design features and facilitates robot design and fabrication process. To ensure applicability of our methodology, we analyze the design process of composite robots reported in the literature and design a multi-locomotion mesoscale robot, called Tribot, as a case study.

We further investigate the application of the proposed actuation and rapid composite robot design methods by questing of *how to achieve multifunctional multi-robot behaviors in mesoscale?* We address this by constructing a unique, untethered, multi-locomotion robotic collective to study locomotion and cooperative behaviors. We investigate minimal, compact and tunable mechanisms that generate high power jumping and low power crawling locomotion. We overcome the key trade-off between the actuation power and weight and construct a 10 g palm-sized prototype, the smallest and lightest self-contained, multi-locomotion robot to date, by folding a quasi-2-D *mechamatronic* composite with locomotion mechanisms, smart actuation and sensing layers, enabling robot multiplicity by assembly-free

mass-manufacturing. The presented unique mesoscale robotic platform is capable of operating in collective to manipulate objects and overcome obstacles together, addressing the locomotion limitations of existing robotic swarms with great scalability. Our research and unique demonstrations reach beyond the robotics research community to *consumer robotics*, industrial production, computer science and biology.

# Résumé

Dans la nature, les organismes à petite échelle sont capables de comportements physiques et collectifs complexes pour s'adapter à des tâches et à des environnements variés par la multifonctionnalité, la multiplicité et la communication. La création de ces capacités dans des systèmes robotiques de moyenne échelle, allant de quelques centaines de micromètres à quelques centimètres, ouvre de nouvelles possibilités pour les utiliser dans plusieurs applications. Ils peuvent être déployés pour des mesures d'atténuation d'urgence dans des environnements ouverts et confinés, pour la surveillance et l'exploration en captant et recueillant des données volumineuses, en émulant diverses biomécaniques d'insectes, en étudiant des comportements collectifs complexes et même en formant de nouveaux comportements. Cette ingénierie dans des systèmes robotiques de moyenne échelle sans dissuader la miniaturisation, la multifonctionnalité et la multiplicité pose d'importants défis pour la conception et la fabrication de matériel robotique. Les méthodes de conception conventionnelles ne sont pas pratiques pour la construction de robots à petite échelle en raison des limitations physiques liées à la réduction de la taille des actionneurs et des engrenages conventionnels, tandis que d'autres mécanismes d'actionnement compacts sont sous-développés et ne sont pas disponibles dans le commerce. En outre, le processus d'assemblage de plusieurs petites pièces est difficile et coûteux, nécessite un travail méticuleux et intensif et, à l'heure actuelle, il n'existe aucun processus automatisé pour la construction de robots de mésoéchelle à partir de la base.

Ce grand défi nécessite le développement de nouvelles méthodologies de conception non conventionnelles et de techniques de fabrication permettant des processus de production en série plus efficaces, personnalisables et entièrement automatisés, tout en prenant en compte la miniaturisation, aussi simple qu'un assemblage de circuits imprimés. Cela nécessite des composants mécaniques discrets et des matériaux composés automatiquement de manière sélective en couches, en incorporant des fonctionnalités, y compris des mécanismes et des actionnements. Un paradigme important qui explore cette question est la fabrication intelligente de composites d'origami robotique, également appelée *Robogami*. Robogami est un robot composite et des machines composites à plis quasi 2D pliables, construits à partir de matériaux fonctionnels, capables de reconstruire diverses formes et mécanismes 3D, théoriquement, avec une infinité de degrés de liberté. Les robots composites héritent de leurs fonctionnalités des couches de matériaux actifs et passifs qui permettent une grande liberté de conception pour l'actionnement et la conception des mécanismes est compacte, minimale et multifonctionnelle. Cependant, les matériaux actifs présentent des comportements très

complexes qui posent des problèmes de conception considérables. Cela est difficile à prévoir, même pour un seul matériau isotrope, alors qu'anticiper leur comportement dans une structure multimatière multicouche est encore plus difficile en raison des interactions de couche qui peuvent avoir un impact imprévisible sur les performances. Bien que la multifonctionnalité et la possibilité de fabrication en série constituent le potentiel réel d'une plateforme robogami, les recherches ont souvent porté sur le développement de robots à fonctionnalité fixe utilisant des matériaux et des composants spécifiques sans méthodologie de conception claire et systématique. Malgré la liberté matérielle de robogami en matière de conception, un grand nombre de prototypes utilisent encore des servos et des mécanismes classiques, ce qui limite la fonctionnalité, la miniaturisation et l'assemblage.

Dans cette thèse, notre objectif de recherche est de développer, étudier et démontrer des systèmes multi-robots multifonctionnels à méso-échelle. En particulier, notre objectif est d'étudier et de démontrer des comportements collectifs terrestres multi-locomotion et collectifs avec des robots de moyenne échelle, similaires aux systèmes naturels à petite échelle, en détectant l'écart sur le terrain. Notre objectif de recherche est de développer, évaluer et démontrer des mécanismes d'actionnement minimaux, compacts, à puissance variable et efficaces pour des méthodes de locomotion multiples et rapides, ainsi que des méthodes de fabrication rapide pour la multiplicité des robots utilisant des matériaux fonctionnels et une conception composite. Ce faisant, nous avons l'intention d'établir une méthodologie de conception complète et systématique pour la conception de robots mésoéchelles multifonctionnels, pouvant être produits en série, pour diverses applications. Cette thèse tente d'abord d'explorer et de répondre à la question de recherche suivante : *comment obtenir une puissance variable, une activation efficace et compacte à l'échelle moyenne ?* Notre objectif est d'obtenir une activation à mésoéchelle de haute puissance, à vitesse variable et à haute efficacité. Nous tentons de résoudre ce problème en explorant des méthodes d'actionnement non conventionnelles à base de matériau actif utilisant un alliage à mémoire de forme et un matériau composite. Pour ce faire, nous recherchons les éléments suivants : *quels compromis faut-il faire entre force, vitesse, efficacité et taille des actionneurs fonctionnels basés sur des matériaux ?* La densité supérieure aux moteurs conventionnels permet un actionnement à grande vitesse et à grande force et permet une multifonctionnalité lorsqu'elle est distribuée et actionnée de manière sélective, le tout avec des formes et une intégrité minimales et compactes.

Alors que nous étudions et développons des méthodes de conception au niveau des composants, telles que l'actionnement, basées sur les performances et les caractéristiques physiques, nous recherchons la même chose au niveau composite ou au niveau système robotique. La prochaine question de recherche que nous tentons de traiter est *quelle est, le cas échéant, la méthodologie de conception générale pour la construction de robots composites ?*. Pour résoudre ce problème, nous formulons et analysons la conception de robogami en termes de *mécanismes, géométrie, composants fonctionnels, matériaux* et *fabrication* afin de mettre en évidence leur relation, leur potentiel et les défis à relever, ainsi que pour structurer les connaissances sur le terrain. . Cela conduit à une approche de conception systématique qui consolide ces caractéristiques de conception critiques et facilite la conception et le processus de fabrication des robots. Pour améliorer l'applicabilité de notre méthodologie, nous analysons le processus de

conception de robots composites repris dans la littérature et concevons un robot mésoéchelle multi-locomotion, appelé Tribot, comme étude de cas. Nous étudions en outre l'application des méthodes de conception de robots composites rapides et d'activation proposées en interrogeant *comment obtenir des comportements multi-robots multifonctionnels à l'échelle méso ?* locomotion et comportements coopératifs. Nous étudions des mécanismes minimaux, compacts et réglables qui génèrent des sauts de puissance élevés et une locomotion de faible puissance. Nous avons surmonté le compromis clé entre la puissance d'actionnement et le poids et avons construit un prototype de la taille d'une paume de 10 g, le robot le plus petit et le plus léger, multi-locomotion autonome à ce jour, en pliant un quasi-2D *mechamatronic* composite avec mécanismes de locomotion, couches intelligentes d'actionnement et de détection, permettant la pluralité de robots par une fabrication en série sans assemblage. La plate-forme robotique mésoéchelle unique présentée est capable d'opérer collectivement pour manipuler des objets et surmonter les obstacles ensemble, tout en tenant compte des limitations de locomotion des essaims robotiques existants avec une grande évolutivité. Notre recherche et nos démonstrations uniques vont au-delà de la communauté de recherche en robotique pour *la robotique grand public*, la production industrielle, l'informatique et la biologie.

# Contents

# List of Figures

# List of Tables

# Introduction

Design in nature generates intricate, ever-improving biological structures and mechanisms to facilitate diverse functionality and adaptation for survival. From the tropical forests of South America where tiny collective animals like trap-jaw ants [1] display physical intelligence by using quick mandible snaps to catch prey [2], as well as to escape-jump predators [3] by charging them against the ground and perform leg-jumps to overcome obstacle in cluttered tropical forests (see Figure 1), to the African deserts where Moroccan flic-flac spiders [4] walk and quickly run through the hot sand by continuously flipping forward, design in nature has evolved to inspire a myriad of multifunctional robots and machines for serving our purpose.

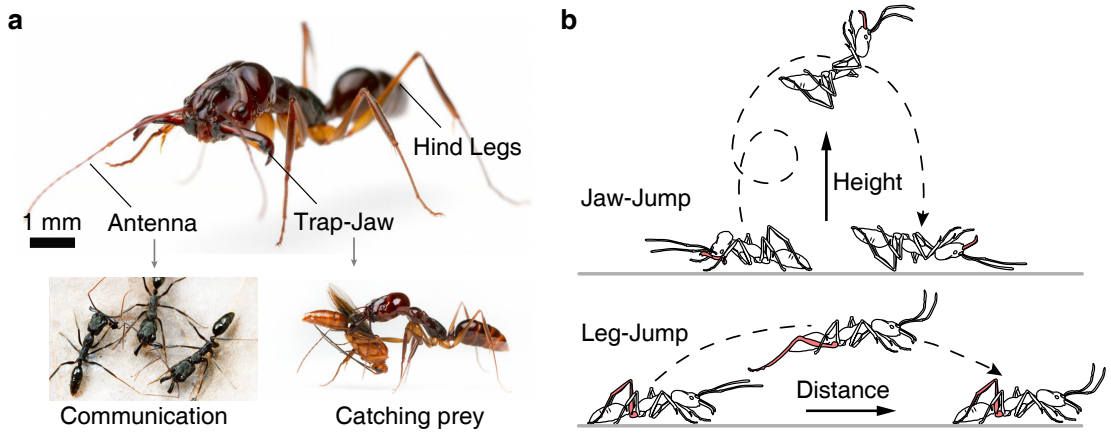


Figure 1 – **Trap-jaw ant, a remarkable example of a collective and multifunctional small-scale physical system.** **a**, the trap-jaw ant, which possesses both collective and physical intelligence to communicate and forage by catching prey using mandible snap closure. **b**, they adapt jaw snaps to leap away from predators by charging them against the ground and use hind legs to navigate in tropical forests by jumping and avoiding obstacles.

Creating these abilities in insect-sized or mesoscale terrestrial robots, ranging from a few millimeters to several centimeters, create a great potential to utilize them for far remote applications, including search and rescue by traversing narrow passages, exploring diverse environments [5, 6, 7] by sensing and collecting data, and even non-invasive surgery [8, 9], impossible with large scale robots. Like a colony of insects, a collective of autonomous mobile millirobots can deploy, move freely on the textured surfaces, communicate and cooperate

toward a common task (Figure 2). Increasing the robot population will maximize space coverage and ensure communication efficiency via sensor networks, thus, their miniaturization will be a key for reduced material usage, compact storage, transportation and deployment. Moreover, millirobot collectives will allow collecting large amounts of intrinsic and extrinsic physical data about to further teach and optimize their designs and behaviours, unfeasible with simulations. These developments would in turn motivate new research into natural organisms, like insect swarms by emulating their intricate social and physical behaviors, as well as diverse biomechanics, from locomotion to manipulation, by employing multifunctional robotic platforms.

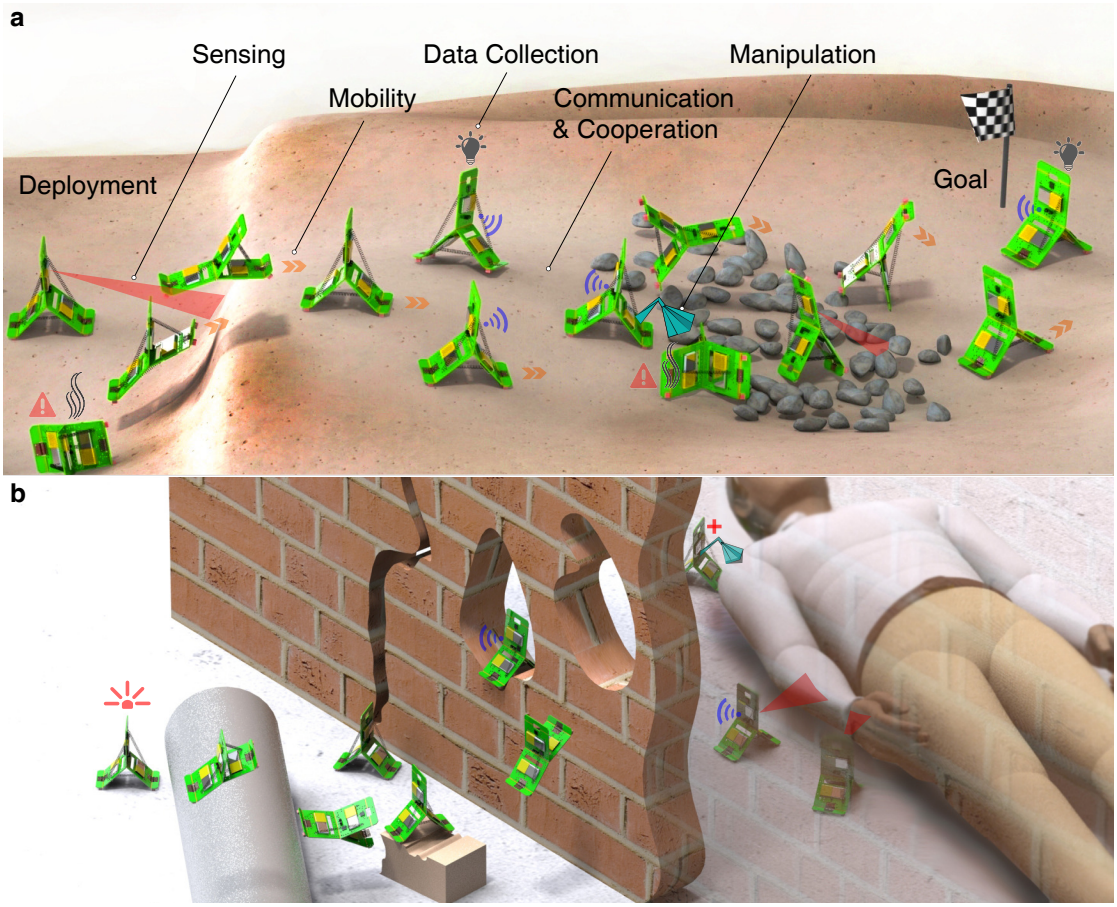


Figure 2 – **The artistic impression of multifunctional mesoscale robotic collectives.** **a**, mesoscale robots can deploy as a colony, move and navigate freely over the challenging terrains, overcome obstacles, sense environment and collect data, communicate with each other, take decisions and cooperate towards a common goal. Although some robots fail, the redundancy and cooperation compensate losses, expanding coverage and allowing disposability. **b**, the search and rescue application scenario with mesoscale robotic collectives that can easily traverse and access confined environments, such as building cracks and crumbles, and signal to rescuers after finding victims. Millirobots could also check-up and provide first medical aid.

However, achieving multifunctionality in mesoscale and robot mass-producibility for collective implementations pose substantial challenges to hardware design and manufacturing due to the complexity and downsizing limitations of the conventional actuation and mechanism design approaches.

## Challenges of Mesoscale Robot Design

Collective operation of autonomous mesoscale robots in large numbers as a "superorganism" necessitates communication, sensing and control hardware. This is now possible thanks to the off-the-shelf, compact, integrated electronic components. However, notably, they require adept physical locomotion mechanisms for mobility in unstructured environments [10]. As the robots shrink in size, the terrain roughness and obstacles grow proportionally, which deter their mobility. Many terrestrial insects such as trap-jaw ants [1], locusts [11], jumping spiders [12], among others have developed multi-locomotion mechanisms, like walking and jumping. Jumping is the most effective and efficient locomotion method for small-scale animals and robots for overcoming obstacles several orders of magnitude larger than their bodies [13, 14]. However, jumping necessitates high power actuation [15] to achieve high take-off velocities, whereas walking requires relatively low power and combining them into a compact robotic body with multifunctional mechanism is challenging. For instance, power generated by conventional motors alone is insufficient to cause instant take-off and requires power amplification [15] by means of a spring element. Spring is charged to store potential energy and released instantly by a locking mechanism. A stiffer spring stores higher potential energy ($PE = \frac{1}{2}kx^2$) and uncharged quicker, hence generates more power ($P = PE/t$). It requires a high torque motor to charge the spring with high transmission gear ratio, hence increased number of gears, which results in the increased robot mass and size. Downsizing the conventional DC motors and gears to produce high torques is unfeasible, whereas compact actuator alternatives are underdeveloped and not available of-the-shelf. This is the fundamental limitation of the conventional robotic mechanism design. Natural systems, like trap-jaw ants, however, does not face this issue: they are as tiny as fingernails yet capable of biting and jumping using the same set of mandibles, walking and jumping using the same pair of legs and rapidly scale population and reproduce at high rates at the "queen factories". Missing or sacrificing some of the colony members does not seemingly deter work; tasks are fulfilled continuously thanks to collective efforts. Then this leads to the real question

***If small-scale animals can carry multifunctionality and reproduce sustainably, how can we create multifunctionality in mesoscale robots and manufacture them en masse?***

Finding a compromise between hardware *multifunctionality*, *manufacturability* and *miniaturization* is a key scientific and engineering challenge to overcome before faithfully answering this question.

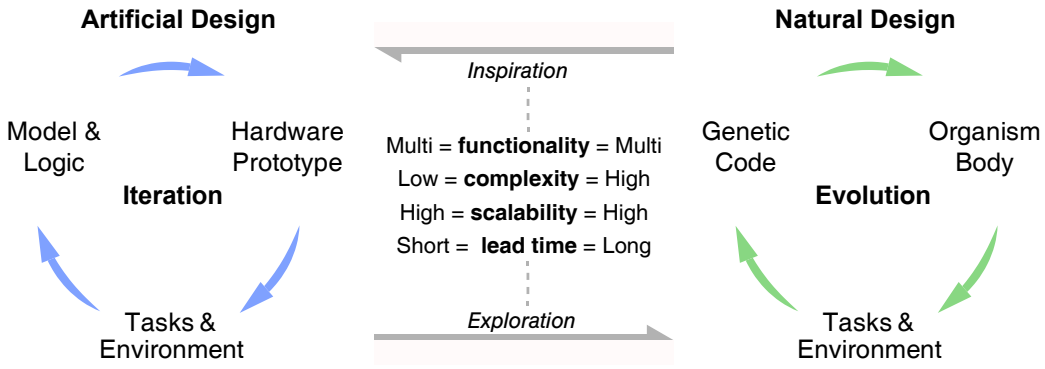


Figure 3 – **Artificial machine design process vs natural design of organisms.** The natural organisms evolve by updating their genetic codes and bodies in response to changing tasks and environment. Engineering design approach is similar in that we set models and logic to build prototypes and test them for different tasks and environments. Natural machines often inspire artificial designs and research into the latter enables new explorations and comprehension of natural systems. Natural machines posses multifunctionality at high design complexity, but can reproduce rapidly to scale up and evolve in a long period. To achieve the same artificially, multifunctionality should be attained with low machine complexity or minimality that in turn leverages scalability in short time by mass-production.

## Natural vs Engineering Design

Unlike the technological artifacts [16], natural organisms including us, underwent complex, selective evolutionary processes over the eons, both physical and genetic [17, 18], by multiplying and diversifying in species and obeying the rule of survival of the fittest. Direct translation of the natural design handbook to engineering design methodology is difficult or often impossible physically owing to limitations of synthetic hardware and material. It is rather uncomplicated to remark and observe functional natural design and acquire inspiration for engineering robots.

In nature, organisms update their genetic codes and bodies in response to changing tasks and environment over a long-term evolutionary process as in Figure 3. Engineering robotic design approach is similar in that we set models and logic, build prototypes and test them for different tasks and environments by progressively iterating designs, however in short-term. The synergy between model, prototype and environment is essential for converging to a successful robot design, while earlier versions are disposed deliberately or at best recycled. Natural systems often inspire synthetic designs and research into the latter instigates new explorations and comprehension of natural systems. Natural machines can achieve multifunctionality even at small-scale with high design complexity and are able to proliferate rapidly by reproduction. To achieve the same synthetically, multifunctionality should be attained with low design complexity or *minimality* that would enable robot miniaturization and mass-production owing to minimal number of mechanisms, components and reduced assembly steps. This is fundamentally unfeasible with conventional mechanical components and mechanisms as

the number of elements grow proportionally to the added functionality, aggregating mass and volume. For instance, passive revolute joints impart two kinematic elements, such as pin and socket, active joints necessitate inclusion of a motor, increasing torque of a joint requires addition of a gearbox, whereas variable stiffness joints require an extra spring element, and so on. If the traditional electro-mechanical design approach is unsuitable for creating multifunctional mechanisms in mesoscale, then the only viable option is to explore synthetic functional materials.

## Multimaterial Design of Mesoscale Robots

While the conventional mechanisms are characterized by integration of several discrete rigid components, functional or smart material create a potential for minimal and compact design. Smart material can fuse multifunctionality within a single isotropic and composite material. For instance, a shape memory alloy (SMA) material acts as a passive flexure joint when inactive and actuates to produce motions without a need for extra joint elements. Thickening the material increases output force without using additional transmission gears, whereas varying temperature stimulus between cold (martensite) and hot (austenite) transformation temperatures can vary actuator stiffness without employing an extra spring. Compliant SMA material can store and release potential energy to amplify mechanical power by inducing unstable shapes and activate for quick shape reversal. This creates a great design freedom for building minimal, multifunctional actuators and mechanisms directly applicable to mesoscale robots.

Mesoscale robot hardware design for mass-production should ideally be composable and customizable as printed circuit boards (PCB), where we not only can assemble diverse layouts of integrated circuit (IC) components, but also embed diverse materials for multifunctionality, including joints, links and actuators, automatically in a matter of seconds. Such an integrated design paradigm will enable tailored construction of versatile robots and their fully automated mass-production at the push of a button from a single manufacturing file and deployment toward different tasks, as illustrated in Figure 4.

Engineering this ability, however, necessitates development of novel techniques beyond one-dimensional PCB design without diminishing the design minimality. It requires robot discrete mechanical, material and electronic ('mechamatronic') components be selectively composed by embedding diverse functionality, including actuation, mechanisms and sensing similar to microelectromechanical systems (MEMS) fabrication [19]. MEMS-based design explores functional materials to construct various micro-devices in bulk, however, with limited size and functionality due to the photo-lithographic processes and dependency on masks. A potential solution for building multimaterial robots in mesoscale is the Smart Composite Microstructure (SCM) manufacturing approach [20]. SCM technique combines various functional material layers for actuation, sensing, flexible hinges and rigid links in 2D by multi-layer lamination process, just like printed circuit assembly. Each layer is processed by selective cutting, en-

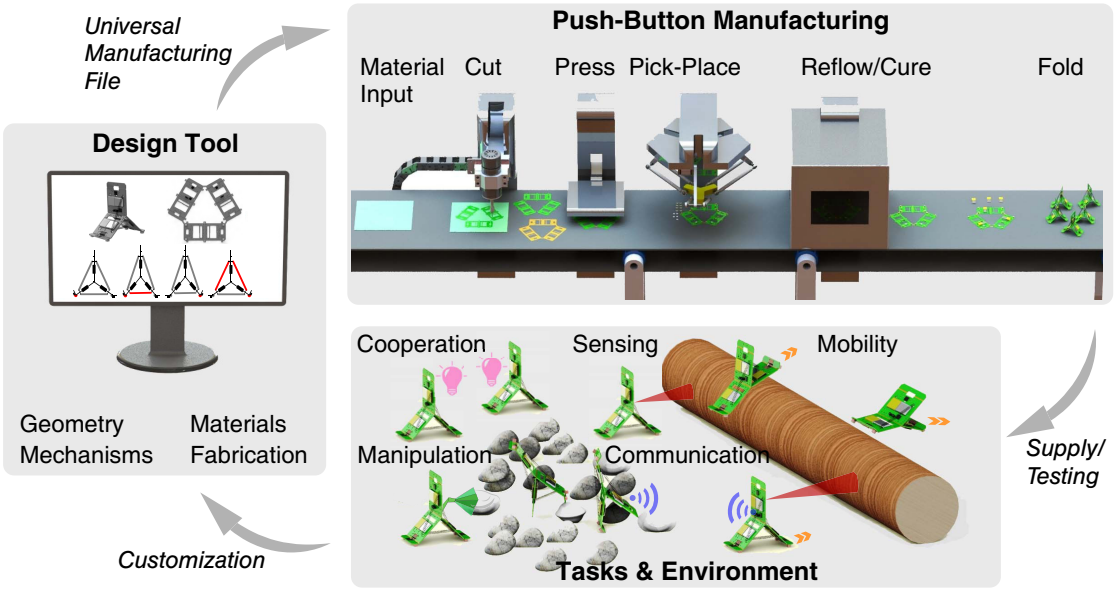


Figure 4 – **Our vision of rapid, customizable and multifunctional robot design paradigm.** Robots are mass-produced automatically, from material and components input to multi-layer, multimaterial robotic systems, at the push of a button from a single, universal manufacturing file generated by a design tool. The fully assembled prototypes are then characterized for diverse tasks and environment and supplied to target various applications. The design tool enables further customization of the robots depending on the performance results.

graving or etching of the relevant layer with extremely fine features. The sandwich is then assembled to 3D by folding, like Origami, making complex structures and mechanisms with minimal assembly effort. This foldable composite mesoscale robots are addressed as origami robots or *Robogamis* [21]. Quasi-2D composite, crease-patterned robogamis can reconstruct various 3D shapes and mechanisms both manually and automatically, theoretically, with infinite degrees-of-freedom (DoF) [22, 24, 25, 26, 27]. While traditional robot mechanical parts are manufactured in 3D, low-profile bodies and components of origami robots are processed in 2D [28, 29] allowing rapid, customized and inexpensive robot fabrication [30], as well as easy storage, transportation, and deployment [31]. These features make robogamis a highly versatile and auspicious platform for studying mesoscale robot multifunctionality and fabrication all together.

Accessibility and customizability of multifunctional, mass-producible mesoscale composite robots is the real potential for far remote applications, as well as robotic education and human-robot interactive devices. Mesoscale robots would allow investigations into a variety of insect bio-inspired behaviours and neuro-mechanics by employing a customizable, yet mass-producible hardware platform.

## Problem Statement

Composite robots inherit their functionality from active materials that allow for great design freedom for actuation design being compact, minimal and multifunctional. Addressing actuation, the very fundamental unit, will enable development of more complex mesoscale active structures and mechanisms. Many existing foldable mesoscale robots still rely on the conventional actuation and transmission components that pose fundamental challenges to miniaturization and assembly. The issue requires development of new, compact and controllable alternative actuation methods based on functional materials and their rapid integration by multi-layer composition. However, active materials display highly complex behaviors that pose substantial challenges to their design. This is difficult to predict even for a single isotropic material without extensive characterization. A piece of functional material actuator displays different behaviours depending on physical shape, compliance, stability, composition, fabrication process and stimulus, whereas anticipating their combined behavior in multi-layer, multimaterial structure is even more challenging due to layer interactions that can cause unpredictable impact on performance. So unlike with classical actuators and rigid mechanisms, currently there is no standard design method and it requires investigations into the mechanics of materials and their composites to achieve desired actuation in terms of performance, such as *speed, force, motion range* and physical features, such as *size, weight, shape* and *integrity*. Research into new actuation methods will expand capabilities of existing mesoscale composite robots and equip them with new functionality previously unfeasible or unexplored.

Multimaterial robot mechanical design is highly integrated since there is no apparent division between their *mechanisms*, *geometry*, *discrete components*, and *materials*. To this end, the research in the field focused on the development of specific components by utilizing specific design methods, without exploring a general design methodology. Investigating components, their composition into functional structures and mechanisms both qualitatively and quantitatively along with consolidating design techniques by creating a clear and repeatable design methodology will improve mesoscale robot design practice and enable development of universal design tools (Figure 4) [32, 33]. This should be backed by the development of rapid and effective fabrication techniques to enable composite robot mass-production. The design methodology should incorporate fabrication as a design parameter that requires studying integration of several active and passive materials without deteriorating robot performance.

Research on both actuation components and robotic system integration should then be demonstrated and validated by constructing several robotic prototypes to ensure applicability of the methods. This requires addressing the critical challenge between *multifunctionality*, *mass-producibility* and *miniaturization* all together with multimaterial design. Conventional robots achieve multifuntionality at the cost of high design complexity that hinders robot miniaturization and assembly. Addressing these will allow to achieve multifunctional multi-robot systems for studying diverse, complex collective and physical behaviors in mesoscale and leverage their application for real-world problems.

## Thesis Statement

In this thesis our research goal is to develop, study and demonstrate multifunctional multi-robot systems in mesoscale. Particularly, our goal is to study and demonstrate terrestrial multi-locomotion and collective behaviours with mesoscale robots, similar to small-scale natural systems, by feeling the gap in the field. Our research objective is to develop, evaluate and demonstrate minimal, compact, variable power and efficient actuation mechanisms for multi-locomotion and rapid fabrication methods for robot plurality employing functional materials and composite design. In doing so, we intend to establish a comprehensive and systematic design methodology for designing multifunctional, mass-producible mesoscale robots for various applications.

This dissertation attempts to explore and answer the following key research question:

***How to achieve variable power, efficient and compact actuation in mesoscale?*** Actuators and mechanisms are the basic functional units of any robotic system and play critical roles in robot performance, including motion range, mechanical power, speed and efficiency, as well as directly influence robot physicality, such as size, weight and shape. The relation between performance and physicality is significant for especially mesoscale robot design and is poorly studied. Our goal is to achieve high power, variable speed and high efficiency actuation in mesoscale. We attempt to address this by exploring unconventional active material-based actuation methods using SMA and composite material. In doing so, we quest of the following: *What are the compromises should be made between force, speed, efficiency and size of functional material-based actuators?* We investigate and demonstrate new, compact multimaterial actuators and mechanisms that possess power density superior to conventional motors, produce high speed and high force actuation and achieve multifunctionality when distributed and actuated selectively, all with minimal and compact forms and easy integrity.

***What, if any, is the general design methodology for constructing composite robots?*** While we study and attempt to generalize design methods at the component level, like actuation, we attempt to look for the same at the composite level or robotic system level. To this end, the research in the field focused on the development of specific mesoscale robotic designs, without exploring a general design methodology. To achieve this we formulate and analyze the robogami design in terms of *mechanisms, geometry, functional components, materials* and *fabrication* to highlight their relation, potential and the challenges, as well as to structure the knowledge in the field. This leads to a systematic design approach that consolidates these critical design features and facilitates robot design process. To demonstrate applicability and ensure generality of our methodology, we analyze the design process of composite robots in the literature and design a multi-locomotion mesoscale robot, called Tribot, as a case study.

***How to achieve multifunctional multi-robot behaviors in mesoscale?*** The research in the field of composite robots has frequently focused on equipping robots with single and fixed functionality that limits their capability and application. Though mass-producibility of composite robots by multi-layer integrated processes is the real potential for multi-robot

implementations, this was vastly disregarded owing to challenges of integrating multiple functionality into minimal assembly processes. To achieve multifunctionality and mass-manufacturability of mesoscale robots, the final part of the thesis consolidates earlier studies on actuation and composite design methodologies into a versatile robotic platform for studying both physical and collective behaviors. We address this by constructing a unique, untethered, multi-locomotion robotic collective to study locomotion and cooperative behaviors. We investigate minimal, compact and tunable mechanisms that generate high power jumping and low power crawling locomotion. We overcome the key trade-off between the actuation power and weight and construct a 10 g palm-sized prototype, the smallest and lightest self-contained, multi-locomotion robot to date, by folding a quasi-2-D *mechamatronic* composite with locomotion mechanisms, smart actuation and sensing layers, enabling robot scalability by assembly-free mass-manufacturing.

## Thesis Outline

**CHAPTER 1. Robot Design Overview**
In this chapter, we provide a general overview of robot design methods and challenges. First, we give insights into the conventional robot design method and macro-manufacturing techniques, challenges and potential along with the state of the art. Then we analyze the challenges of multifunctional mesoscale robot design and manufacturing. Specifically, we motivate the need for minimal design of millirobot multi-locomotion mechanisms and their mass-manufacturing to create robotic collectives. We demonstrate why composite design could address this challenge by taking a glimpse at the state of the art in origami-inspired robotics. We finally identify the robogami four mechanical features such as *geometry*, *mechanisms*, *functional materials* and *fabrication*, and summarize their relation, potential and the challenges in comparison to the conventional robot design.

**CHAPTER 2. Actuation Design for Mesoscale Mechanisms and Robots**
In this chapter, we design, model and experimentally validate four novel actuation methods for mesoscale robots based on functional material: three SMA-based and based on fluid. Each actuator design targets multifunctionality, miniaturization, easy assembly for mass-production and minimality and addresses several challenges:

- **Helical spring SMA-based high power and high speed actuation.** We present a novel compact, high speed minimal mechanism driven by coil-type SMA actuators with variable power output. We demonstrate the applicability of the mechanism for building mesoscale multi-locomotion robot Tribot. These work addresses the speed limitations of SMA actuators.

- **Bending sheet Omega-SMA actuator for high torque and power efficient actuation.** We present a novel, compact, high torque torsional SMA actuator design. We model the thermo-mechanical behavior of the actuator and perform different characteriza-

tion experiments in different loading conditions. To demonstrate its applicability in distributed multi-actuator mesoscale robots, we construct a reconfigurable robotic surface to achieve several shapes in closed-loop. This work addresses the high torque generation with SMA actuators with low power consumption.

- **Linear flat spring Wave-SMA actuator for inlay integration with easy assembly and multi-layer composite actuation.** We present a new type of linear spring SMA actuator that overcomes challenges of coiling process of helical-type actuators by cutting a flat sheet of material in wave-forms, enabling minimal, yet customizable design that can be compactly embedded in composite fabrication with assembly-free process. We provide a mechanical model of the actuators and compare it with the characterization tests for loading. We also present a novel multi-layer composition method of several flat actuators for increasing the force capability with no power expense. This work advances the fabrication and integration of SMA actuators into composite robots.

- **Bending vacuum-powered actuator for high speed, distributed actuation.** We present a new fluid-driven actuation and selectively embedding method for constructing multi-joint, shape-morphing mesoscale robotic structures. Our design enables a single source, distributed actuation with multi-step actuation sequence by programming the fluidic channel networks. The tunable networks are compactly embedded in a multi-layer lamination process with minimal assembly. We present an analytic model for a single actuator unit, characterize and validate with several prototypes. We demonstrate implementation of several actuators in complex networks for folding multi-joint origami patterns, including Miura-ori and sequentially folding box.

Based on the studies of diverse SMA actuator designs, we present a generalized methodology for designing custom SMA actuators from the ground up to facilitate their design process and encourage accessibility of actuation methods for the development of mesoscale robots.

**CHAPTER 3. Design Methodology for Mesoscale Robots**
In this chapter, we present a comprehensive formulation of a mechanical design process of origami-inspired multimaterial robots and machines, (that we also call *Robogamis*, in terms of *geometry*, *mechanisms*, *functional materials* and *fabrication*. We highlight their relation, potential and the challenges, and finally we present a systematic design methodology to facilitate their design process. We demonstrate applicability of our generalized methodology to the majority of robogamis presented in the literature; making it generic and extendable. We also demonstrate the validity and effectiveness of the method by designing a latest version of the jumping and crawling origami robot, Tribot. Tribot's design follows our proposed design process and for each step we evaluate design choices, qualify and characterize them. We close the loop by implementing a locomotion controller to accurately regulate Tribot's locomotion and compare it to the theoretical models. This work not only facilitates the design process of robogamis, but also leverages development by filling gaps in the research field and invites potential contributors from diverse areas of research.

**CHAPTER 4. Design of a Multi-Locomotion Mesoscale Robotic Collective**
In this chapter, we demonstrate the capability of our design methodology for constructing *push button* mass-manufacturable origami robots with mechanisms, material and electronic layers readily-composed to produce untethered, self-contained, multifunctional *mechamatronic* robots. Here, we design the latest version of an autonomous, multi-locomotion millirobot Tribot, inspired by trap-jaw ants, that addresses the locomotion mechanism design and scalability challenges of small-scale terrestrial robots. We present a unique example of minimal, compact and tunable mechanism that generates five distinct locomotion gaits: height (vertical), distance (horizontal) and somersault jumping to clear obstacles, flic-flac walking on textured terrains and inchworm crawling on flat surfaces. The untethered, battery-powered millirobot can selectively switch gaits to transit diverse terrains and operate collectively to manipulate objects and overcome obstacles in tandem. We constructed the 10 g palm-sized prototype (see Figure 4.1), the smallest and lightest self-contained, multi-locomotion robot to date, by folding a quasi-2-D mechamatronic composite with locomotion mechanisms, smart actuation and sensing layers, enabling robot scalability by assembly-free mass-manufacturing.

**CHAPTER 5. Conclusion and Contributions**
Here, I conclude and provide contribution statements along with the list of publications. I share future visions on multifunctional, mass-producible robots related to current technological trends, such as digital manufacturing, machine learning and biology.

# 1 Robot Design Overview

In this chapter, we provide a general overview of robot design methods and challenges. First, we give insights into the conventional robot design method and macro-manufacturing techniques, challenges and potential along with the state of the art. Then we analyze the challenges of multifunctional mesoscale robot design and manufacturing. Specifically, we motivate the need for minimal design of millirobot multi-locomotion mechanisms and their mass-manufacturing to create robotic collectives. We demonstrate why composite design could address this challenge by taking a glimpse at the state of the art in origami-inspired robotics. We finally identify the robogami four mechanical features such as *geometry*, *mechanisms*, *functional materials* and *fabrication*, and summarize their relation, potential and the challenges in comparison to the conventional robot design.

## 1.1 Conventional Robot Design

Conventional robot designs characterize artificial machines made of rigid links, joints, transmission, actuators, sensors and electronic hardware components; all run synergistically by control logic. Kinematics of rigid bodies define robot motion, such as rotation, translation, or simultaneous combination of both with respect to a fixed or floating reference frame [34]. Linkages are the basic elements of robot mechanisms arranged in closed, open or mixed multi-body chains. Links and joints make up the linkages and their class, configuration and population decide degrees of freedom (DoF). Classical joints combine kinematic pairs, such as pin-hole, ball-socket, slider-slot among others that enable relative motion of one element or link with respect to another. Robot rigid body dynamics relates robot kinematics to internally (actuation) and externally (interaction) acting forces and energies, described by Newton's second law of motion ($F = \sum_{i=1}^{n} ma_i$) and Lagrangian mechanics ($\frac{\mathrm{d}}{\mathrm{d}t}\left(\frac{\partial L}{\partial \dot{q}}\right) = \frac{\partial L}{\partial q}$), respectively. From the stationary multi-link, serial and parallel industrial robots that perform highly accurate and heavy duty repeated tasks in controlled environment to mobile robots that move freely and interact with uncontrolled, cluttered domain or media, the universal rules of rigid body mechanics can describe their motion.

Recent advancements in readily available low cost, off-the-shelf mechatronic devices and development kits, like motors, gears, joints, sensors and electronic break-out boards, have further fueled engineering design of robot by enabling flexibility and customizability through standardization. Progresses in manufacturing technologies, like CNC machining and multi-material 3D printing have facilitated hands-on prototyping of robot parts inside and outside factories for research, education and personal use.

Conventional robots and machines have mechanical parts and structures assembled in 3D, which is only a viable option at macro scale for reasons of functionality, structural strength, materials and manufacturing processes. The main objective for robot material selection is to ensure structural resilience to carrying not only their own weight but also handling external forces and vibrations. Therefore, robot materials do not directly bring functionality and are the least critical and come last in the design chain (Figure 1.1, left). While the material selection for functional components such as actuation, sensing and joints are designed and standardized by vendors, the custom-made robot passive rigid links and specific mechanisms, like transmission gears, combine discrete rigid elements that are well-studied and might at worst require structural analysis rather than look into mechanics of materials, like compliance. The material choices are standardized and are limited by the well-established manufacturing processes, be it metal CNC machining, multimaterial 3D printing or more costly carbon fiber lamination.

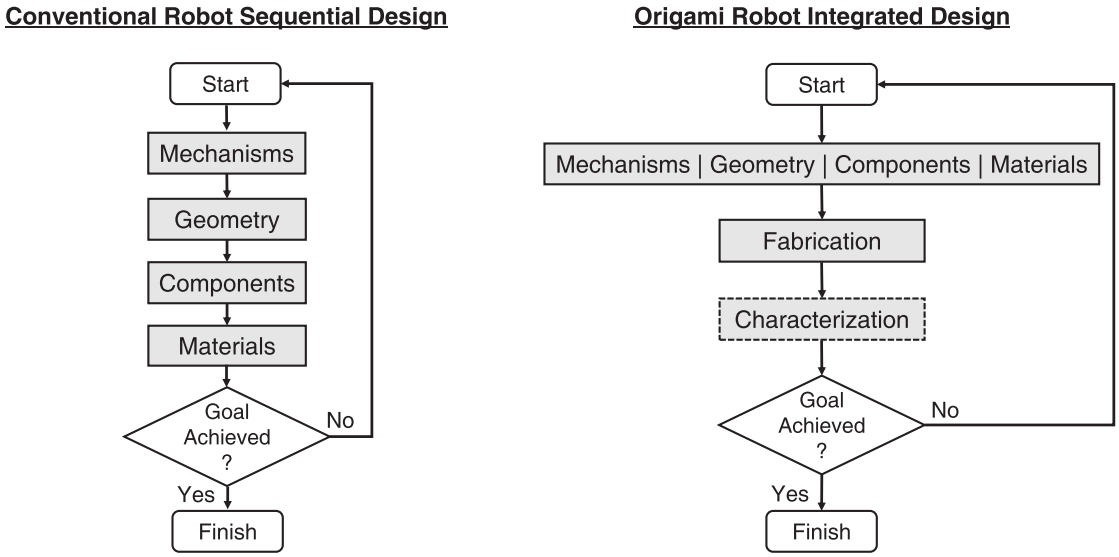


Figure 1.1 – **Conventional vs Robogami mechanical design.** The conventional robot design scheme follows a sequential design and each sub-block is well-studied and standardized by models of mechanisms, 3D geometric structures, mechanical elements, as well as employed materials. The composite design requires concurrent design and simultaneous development, and there is no standard model. As the functionality of origami robots depends highly on materials, whose properties greatly vary with composition, geometry, and fabrication process, there is no single solution and the design necessitates iterative fabrication and characterization tests to achieve desired functionality.

The laws of classical mechanics describe how robots move, however, they do not explain how robots should be constructed. This knowledge is acquired and learned rather empirically from robotics practice sessions and handbooks [35], emerging industrial applications, challenges and competitions and rapidly growing makers communities. Albeit the hands-on robot design process is still tedious and requires several iterations by trial-and-error to achieve a satisfactory design and even more for a fully functional one. Recent advancements in computational tools have improved robot design methodologies by bringing them into simulation [36] and virtual environments [37]. Such tools allow an intuitive drag-and-drop and assemble experience of diverse robot designs [38] for producing various motions from component libraries. While such tools are valuable to optimize robot morphologies and motions, often in non-intuitive ways and systematically test control algorithms, they still rely on fabricated prototypes for recreating them digitally at the outset and validating in the real world environment to further optimize and bolster the design intuition. Another non-intuitive design approach in the field of evolutionary robotics [39] uses genetic algorithms to evolve robot morphologies and control by constructing them from selectively moving infinitesimal unit cells [40, 41]. These algorithms not only can generate several robot morphologies with optimized locomotion, they also provide valuable insights into how natural systems evolved using a digital platform. The main downside of the approach is that it often produces complex morphologies and behaviors that are difficult or even impossible to fabricate and reproduce physically. In that sense, simulation environments face a common challenge of predicting robot intrinsic mechanical behaviors, such as friction losses and deformations, and extrinsic effects such as interaction with unstructured environments, which hinders their faithful reproduction in real world environments. Therefore, rapid hardware prototyping of robots and interfacing them with the entire intricacy and variation of the physical environment is inevitable for optimizing and validating computational models and is as vital as for living organisms, which evolve their genetic codes in response to natural environments they thrive in.

Macro-manufacturing allowed to automate assembly processes and revamp the mechanism and actuation designs of industrial robots that can now lift payloads exceeding a ton, four times larger than the elephant's trunk, with accuracy and repeatability superior to animals and continuous operation capability for all day long [42]. Robotic manipulators are soon to assemble themselves in a fully automated ABB factories in Shanghai, which significantly improves efficiency, cuztomization by machine learning algorithms and use of space [43]. Mass-manufacturing of electromechanical components also enabled prototyping autonomous mobile robots with various locomotion strategies from wheeled [44], walking [45], running [46] to flying [47] machines that are a prominent remedy for day-to-day assistance, search and rescue, exploration, environmental monitoring, delivery and transportation. Mobile robots as big as the Tesla Semi trucks assembled by smart robot co-workers at Gigafactory are soon to assist human transportation with full autonomy at high speeds [48]. For such robotic products, design for mass-manufacturing[49] is critical, which leverages systematic design methodologies, standardization, and efficient usage of materials and resources with the aid of software algorithms. The digital manufacturing trend has a great potential to push the technological

boundaries of robotic hardware design and eventually merge the considerable gap between the software and hardware capabilities. Currently, conventional mass-manufacturing and assembly processes are still semi-automated and require human intervention for reasons robots are yet incapable of handling complex manipulation tasks. This, however, is not labor intensive as the macro-scale parts do not necessitate special equipment and skills to assemble, and processes are semi-automated, well-optimized and tailored to workers' capacity.

## 1.2 Mesoscale Robot Design and Challenges

Mesoscale robots or millirobots, create a great possibility to utilize them for far remote, mobile applications, including search and rescue by traversing narrow passages, exploring diverse environments [5, 6, 7] by sensing and collecting data, and delivering drugs [8, 9], impossible with macro-scale robots. Increasing the millirobot population will maximize space coverage and ensure communication efficiency via sensor networks, thus, their size and weight is crucial for material usage, transportation and deployment. However, as the robots shrink in size, the terrain roughness and obstacles grow proportionally, which creates challenges to their hardware design.

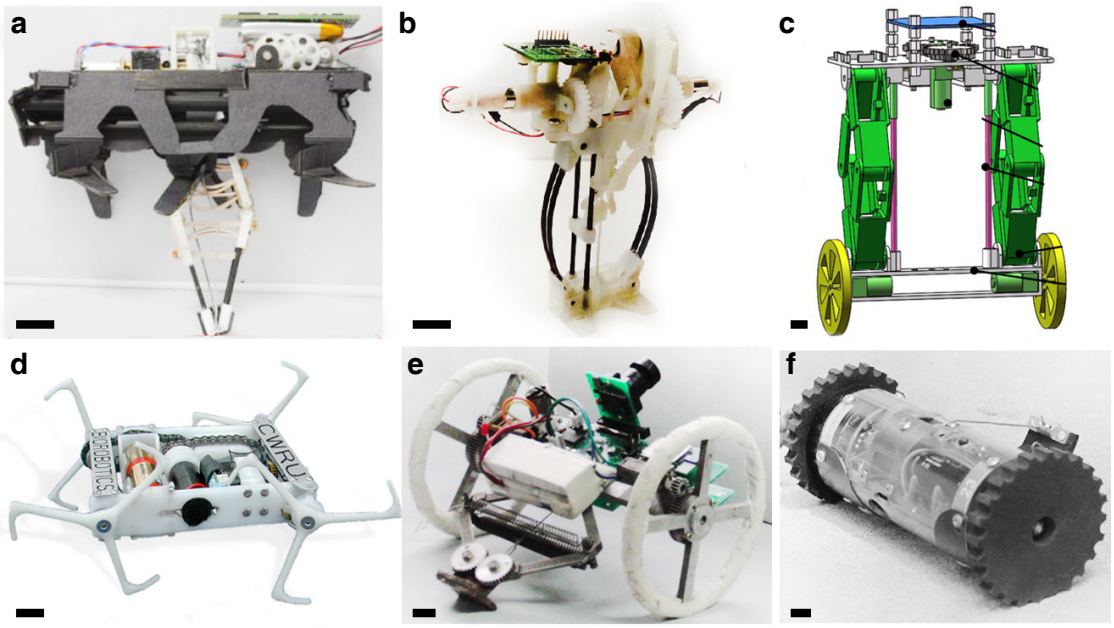


Figure 1.2 – **The smallest, battery-powered, terrestrial multi-locomotion robots in the literature.** The scale bars correspond to 10 mm. **a**, walking and jumping robot JumpRoach [50], **b**, MSU jump-runner [51], **c**, Wheel-hopper [52], **d**, running and jumping robot MiniWhegs [53], **e**, wheeled jumping surveillance robot [54], and **f**, rolling and jumping robot Scout [55]. All robots use conventional motor and transmission mechanisms allocated for each locomotion.

Many terrestrial insects possess multi-locomotion strategies, such as walking and jumping [1, 11, 12]. Jumping is the most effective and efficient locomotion strategy for small-scale

animals and robots for overcoming obstacles several orders of magnitude larger than their size [13, 14]. However, jumping necessitates high power actuation [15] to achieve high take-off velocities, whereas walking requires relatively low power and combining them into a compact robotic body with minimal, yet tunable power mechanism is challenging. Power generated by motors alone is insufficient and slow to cause instant take-off and requires power amplification [15] by means of a spring element. Spring is charged to store potential energy and released instantly by unlocking. A stiffer spring stores higher energy ($PE = \frac{1}{2}kx^2$)) and uncharged quicker, hence generates more power ($P = PE/t$). It necessitates a high torque motor to charge the spring with high transmission gear ratio, hence increased number of gears, which results in increased robot mass and size. Downsizing the conventional DC motors and gears is unfeasible, whereas compact actuator alternatives are underdeveloped and not available of-the-shelf. Existing self-contained, battery powered multi-locomotion robots (Figure 1.2) use conventional individual mechanisms and components for each locomotion [50, 51, 52, 53, 54, 55], which not only deter miniaturization, but also hinder their assembly and mass production.

## 1.3 Mesoscale Robot Manufacturing

Mass-manufacturability and customizability of millirobots create potential for low cost and on-demand deployment into cluttered environments with disposability. Albeit, the conventional robot design and manufacturing methods are effective at macro-scale, they are impractical for constructing robots at mesoscale for physical, cost and manufacturing reasons. Scaling down the traditional "nuts-and-bolts" design approach has physical limitations, where their assembly is extremely difficult. Hence, this is one of the reasons luxury watches are costly as their mechanisms are rather meticulously crafted than mass produced. The most current commercially available multimaterial 3D printers based on stereolithography [56] face limitations for achieving very fine resolutions, robustness and the printable material is limited to polymers. NEMS and MEMS micro-fabrication techniques enabled miniature electronic devices and mechanisms with extremely high resolution. However, the photo-lithography-based processes face limitations in geometry and material choices due to high dependency on masks and substrates, hindering design flexibility.

Manufacturing of mesoscale components that lie between macro- and micro-scale requires the development of novel techniques that allow for more efficient and flexible mass manufacturing while maintaining the micro-scale features for mechanism elements. One of the promising directions is a SMC manufacturing process and folding inspired by origami design [20]. The process allows for micromachining material sheets in 2-D and assembling them by folding, generating complex mesoscale geometries. Various layers for smart actuation, sensing, flexible joints and rigid backing are processed by selective engraving, cutting and etching of the relevant layer and composed in additive process with minimum intervention. The sandwich is then assembled by folding. Such manufacturing methods are immediately applicable to multimaterial composite mesoscale robots, also addressed as origami robots or robogamis.

## 1.4 Composite Robot Design

Robogamis are multimaterial composite machines that embed several layers of functional material for actuation, sensing, flexible hinges, rigid tiles among others, sandwiched and folded or self-folded to make different 3D robotic structures with high DoF. This allows for rapid prototyping of robots with reduced assembly effort. Numerous origami robot prototypes have a wide volumetric scale range, from micro-scale drug delivery robots [57] folded by hydrogel, millimeter scale mobile robots [58, 28, 21, 72, 59, 60, 61], centimeter scale reconfigurable sheets [25, 27, 62] and robotic grippers [63, 64] that utilize shape changing properties of alloys like Nitinol as actuation, also known as shape memory alloy (SMA), or various other polymers, like shape memory polymer (SMP) as an actuator or variable stiffness joints. Some of the prototypes are depicted in Figure 1.3. Actuation methods, especially SMA, provide extremely high power output weighing few tenths of mg [78], ideal for miniaturization.

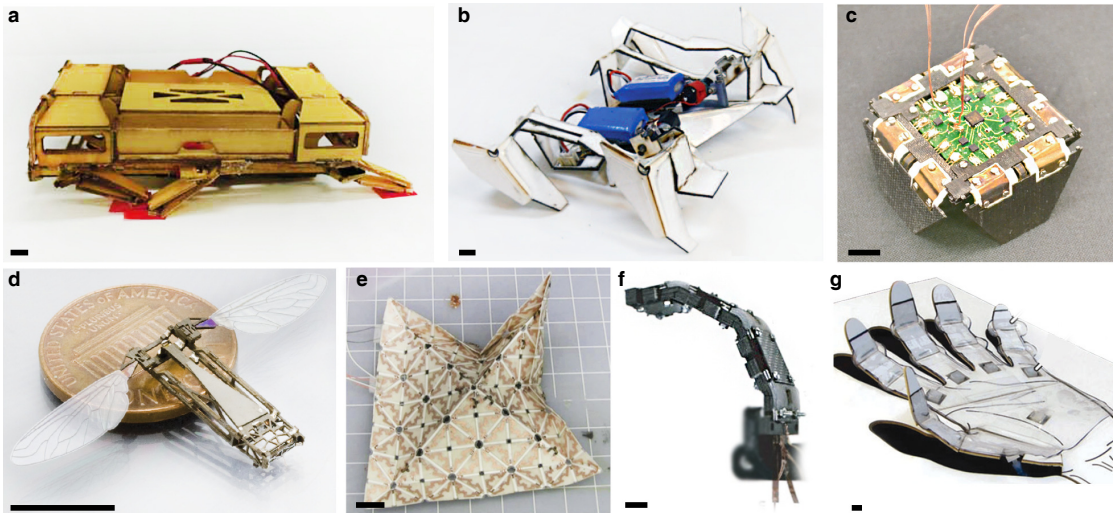


Figure 1.3 – **Selected examples of robogami prototypes in the literature**. The scale bars correspond to 10 mm. **a**, high payload bearing walking Roach robot that utilizes conventional actuation and transmission [58], **b**, the battery-powered self-folding and walking origami robot that uses SMP material for self-folding and DC motors for walking [28], **c**, fully active material-powered, tethered robogami crawler with embedded SMA actuators and strain sensors for gait control [21], **d**, piezo-powered, tethered flapping wing robot Mobee [72], **e**, self-folding reconfigurable sheet with embedded SMA actuators [25], and **f**, three-joint, tendon-driven origami finger that uses SMP material for locking DoF and adjusting stiffness at each joint [64] and **g**, a self-folding hand powered by fluidic pouch actuators [65].

Despite the material design freedom of robogami platform, a vast number of prototypes still utilize conventional servos and mechanisms for driving origami-based passive structures. While this expands freedom of reconstructing 3D shapes by folding thin, creased sheets, miniaturization and customizability are deterred. Creating such specific structures is now possible using computational tools [66, 67, 68] with ready libraries of various origami geometries that facilitates the design process. Such tools are education-oriented, therefore, lack multimaterial

features and do not alleviate manual assembly.

## 1.5 Composite Design Challenges

Unlike conventional robots, they inherit functionality from the multimaterial layers, which poses challenges to design due to their complex nature. Beyond classical rigid-body mechanics, it requires investigations into the mechanics of materials. This is difficult to predict even for single isotropic material without characterization, whereas anticipating their combined behavior in multi-layer, multimaterial structure poses even greater challenges due to layer interactions. The structural compliance between layers can cause in the worst-case failure, and in the best-case, unpredictable impact on discrete components. Moreover, multimaterial machines are highly integrated since there is no apparent division between mechanisms, geometry, functional components and materials (Figure 1.1, right). For instance, a traditional mechanism is a combination of multiple active and passive mechanical components, like motors, bearings or springs, whereas the material-based systems are different, in that a piece of functional material can generate a complex mechanism, like, for example, the variable stiffness joints constructed from shape memory polymer (SMP) [64, 69], or a SMA actuator component alone can be a bi-directional folding mechanism [70]. Moreover, in origami robots the characteristics of a material vary greatly, not only with composition and geometry, but also with the fabrication process. For instance, a SMA material with the same composition and geometry displays different behavior if annealed at different temperatures or duration [78], or a stretchable sensor's resistance varies with the machined and etched mesh resolution [71]. So, there is no single and standardized fabrication method, which is an important design parameter when defining multimaterial machine and robot performance. To this end, design requires an iterative approach for integrated layout, fabrication and characterization process to achieve satisfactory results as depicted in Figure 1.1, right.

## 1.6 Conventional Robot vs Composite Robot Design

Streamlining the robogami design process requires insight into the nature of the essential mechanical design features that we categorize as geometry, mechanisms, functional materials and fabrication process, with first comparison to conventional robot design approach to set a common base. The all-inclusive comparison of robogami mechanical design in terms of geometry, mechanisms, materials and discrete components and fabrication process to conventional robot design is listed in Table 1.1, summarizing technologies and methods, as well as challenges for both. The defined sub-features, such as shape, kinematics, joints, or actuation help to create analogy between the two. While some of the conventional design considerations are still applicable to robogami construction, robogamis possess greater design versatility in creating multiple 3D functional shape transformations or low-profile compliant joints, that if patterned accordingly, produce motions like bending, compression or elongation otherwise unfeasible with the conventional rigid kinematic pairs. Robogamis also enable usage

of a vast number of functional materials from active metals to polymers and their rapid 2D fabrication in multiple layers, programming some of them by chemical or thermal treatment and pile-up into a single monolith. Novel methods and techniques are still being developed and adding on, expanding the robogami design space. This requires further quantification, standardization and integration of the design process. The comprehensive definitions of the above-mentioned features for robogamis are described next.

Table 1.1 – Comparison of the four essential mechanical design features between conventional and origami robots.

| | Sub-Features | Conventional Robot Mechanical Design | Origami Robot Mechanical Design |
|---|---|---|---|
| **Geometry** | Shape | 3D body, 3D multi-parts | Single or multiple 3D bodies, 2D crease patterns and multi-layers |
| | Kinematics | Jacobian matrix, joint angles, Cartesian position | Fold sequence, fold angles, Cartesian position, shape |
| | Challenges | Inverse kinematics of redundant systems | 3D to 2D unfolding, modeling of non-zero surface area (smooth) folds and deformations |
| **Mechanisms** | Joints | Revolute, prismatic, spherical | Bending, torsion, lateral bending, shear, compression, elongation |
| | Linkages | Serial or parallel configuration | Open chains, closed chains, tree configuration |
| | Challenges | Friction, backlash, other disturbances | Non-linear fold elasticity and deformation, smooth fold dynamics, high-dimensional fold space |
| **Material Components** | Actuation | Electric, magnetic, hydraulic, pneumatic, piezoelectric | Electric, magnetic, pneumatic, piezoelectric, thermal, ionic, light, chemical |
| | Angle sensing | Optical, magnetic | Magnetic, resistive, capacitive, inductive |
| | Material | Metal, plastic, carbon fiber, glass, silicone | Metal solid and liquid, plastic, paper, glass, silicone, polymers and composites, ceramics, carbon ink, fabric, and more |
| | Challenges | Low customization and high cost at milli-scale | Material non-linearity, hysteresis, parameter estimation and characterization |
| **Fabrication** | Methods | CNC and laser machining, 3D printing, molding, forming | CNC and laser micro-machining, multimaterial 3D printing, 3D deposition, molding, layer-by-layer lamination, pressing, heat treatment, forming, stamping |
| | Challenges | Assembly time and effort | Multimaterial composite manufacturing, standardization, process automation |

## 1.7 Conclusion

Conventional robots are known for their rigid forms that combine hard components, such as conventional motors, joints, gears, etc. They are built for specific tasks and are proven

especially for macroscale, heavy-duty applications. While the material selection for functional components such as actuation, sensing and joints are designed and standardized by vendors, the custom-made robot passive rigid links and specific mechanisms, like transmission gears, combine discrete rigid elements, materials and their design processes are well-studied and standardized. Composite material-based robots create a potential for mesoscale robot design with minimal and compact forms. Smart material can fuse several functionality within a single isotropic or composite material that is directly applicable to multifunctional mesoscale robots, enabling miniaturization and mass-manufacturing for multi-robot applications.

# 2 Actuation Design for Mesoscale Multi-material Composite Robots

Actuators and mechanisms are the fundamental functional units of any robotic system and play critical roles in robot performance, including power, speed and efficiency, as well as directly influence robot physicality, such as size, weight and shape. The relation between the performance and physicality is significant in the conventional robot design. For instance, direct drive electro-mechanical motors reach higher speeds and are more compact and lighter than the ones with gear box, suitable for flying robots. In order to achieve high power actuation, for instance for jumping locomotion, it requires both high force and high speed actuation ($P = Fv$), which is contradictory for traditional motors for earlier mentioned reasons. It requires additional components, such as high stiffness spring to charge it by high torque motor, store energy by locking and uncharging it quickly by unlocking. This mechanism with single functionality requires several mechanical elements, resulting in increased robot size, weight and complexity, whereas attaining multifunctionality is highly challenging. This is the fundamental limitation of conventional actuation methods that makes them inappropriate for building multifunctional robots in mesoscale, which opens an important question: *How to achieve high power, high speed and high efficiency actuation in mesoscale?*. This part of the thesis attempts to answer this research question by exploring alternative, unconventional actuation methods using functional active materials and composites that have challenging characteristics to design. We demonstrate new multimaterial actuators and mechanisms that are superior to conventional actuation methods in terms of power density with comparable efficiency, capable to achieve high speed, high power actuation and produce multifunctionality

The material presented in this chapter is adopted from the following publications:

**Zhakypov, Z.**, Falahi, M., Shah, M., and Paik, J. The design and control of the multi-modal locomotion origami robot, Tribot, IEEE IROS, pp. 4349-4355, 2015.
**Zhakypov, Z.**, Belke, C.H., and Paik, J. Tribot: A deployable, self-righting and multi-locomotive origami robot. IEEE IROS, pp. 5580-5586, 2017.
**Zhakypov, Z.**, Huang, J.L. and Paik, J. A novel torsional shape memory alloy actuator: Modeling, characterization, and control. IEEE Robotics and Automation Magazine, 23(3), pp.65-74, 2016.
**Zhakypov, Z.**, Heremans, F., Billard, A. and Paik, J., An origami-inspired reconfigurable suction gripper for picking objects with variable shape and size. IEEE Robotics and Automation Letters, 3(4), pp.2894-2901, 2018.
**Zhakypov, Z.**, Mete, M., Fiorentino, J. and Paik, J., Programmable Fluidic Networks Design for Robotic Origami Sequential Self-Folding. IEEE RoboSoft, pp. 814-820, 2019

when distributed, all with minimal and compact forms.

In this chapter, we present four novel actuation methods for mesoscale robots: three SMA-based actuation approaches for continuous rotational, linear and high speed discrete motions and a fluid-driven rotational motion. Each actuator design targets multifunctionality, miniaturization, easy assembly for mass-production and minimality. We design, model and experimentally validate them and demonstrate a variety of applications.

- **Helical spring SMA-based high speed actuation.** We present a novel compact, high speed minimal mechanism driven by coil-type SMA actuators with variable power output. The Y-shaped mechanism is folded from multi-layer composite material, embedding three rigid links connected by a compliant joint and when adjusted properly produces continuous bending and discrete snapping motions. We demonstrate the applicability of the mechanism for building mesoscale multi-locomotion robot Tribot. These work addresses the speed limitation of SMA actuators.

- **Bending sheet Omega-SMA actuator for high torque actuation.** We present a novel, compact, high torque torsional SMA actuator design. We model the thermo-mechanical behavior of the actuator and perform different characterization experiments in different loading conditions. To demonstrate its applicability in distributed multi-actuator mesoscale robots, we construct a reconfigurable robotic surface to achieve several shapes in closed-loop. The low-profile actuator consumes half-Watt power, produces high range of motion ($\approx 180^\circ$), weighs only 0.07 g, and generates 34.1 mNm torque, demonstrating superior performance over the similar-sized actuators. This work addresses the high torque generation with SMA actuators at low power.

- **Linear flat spring Wave-SMA actuator for inlay integration.** We present a new type of linear spring SMA actuator that overcomes challenges of coiling process of helical-type actuators by cutting a flat sheet of material in wave-forms, enabling minimal, yet customizable design that can be compactly embedded in composite fabrication with assembly-free process. We provide a mechanical model of the actuators and compare it with the characterization tests for loading. The actuator is 150 um thick, weighs only and produces force up to 1 N. We also present a novel multi-layer composition method of several flat actuators for increasing the force capability with no power expense. This work advances the fabrication and integration of SMA actuators into composite robots.

- **Bending vacuum-powered actuator for distributed actuation.** We present a new fluid-driven actuation and selectively embedding method for constructing multi-joint, shape-morphing mesoscale robotic structures. Our design enables a single source, distributed actuation with multi-step actuation sequence by programming the fluidic channel networks. The tunable networks are compactly embedded in a multi-layer lamination process with minimal assembly. We present an analytic model for a single actuator unit, characterize and validate with several prototypes. We demonstrate implementation of

several actuators in complex networks for folding multi-joint origami patterns, including Miura-ori and sequentially folding box.

Based on the studies of diverse SMA actuator designs, we finally present a generalized methodology for designing custom SMA actuators from the ground up to facilitate their design process and encourage accessibility of actuation methods for the development of mesoscale robots.

## 2.1 Mesoscale Actuators Overview

Actuators play critical roles in achieving composite robot functionality in otherwise static and passive structures. Customizability of the material components is an important asset. Besides being compact and lightweight to allow for distribution of several on a quasi-2-D lattice without overloads, the actuators should also be customizable and reversible in terms of force and motion to achieve flexibility in shape transformation and movement, such as locomotion or manipulation. They should produce sufficient range of motion and torque to perform motions with multiple flexure joints, so electric drives are not effective at mesoscale. Therefore, alternative approaches using functional materials could address this limitation being compact, customizable and obeying multi-layer composition design paradigm. Figure 2.1 depicts existing actuator solutions for mesoscale mechanisms and robots. Piezoelectric cantilever actuators generate low stroke high frequency deflection when activated by high voltage periodic waveforms useful for flapping-wing microrobots. Shape memory polymer (SMP) actuator [73] with embedded heater layer shrinks when heated thermally to generate a bending moment owing to offset from the neutral plane. Pneumatically-driven pouch actuators [65] with sealed four sides inflate to generate a bending moment due to the curvature induced at the rotational axis, whereas dielectric elastomer actuator [75] that comprise two layers of stretchable electrodes (black) and elastomer material sandwiched between them. The elastomer squeezes and expands due to electrostatic forces upon high voltage and the electrodes can be selectively distributed to produce various motions. Torsional sheet SMA actuator [74] programmed to cause twisting around the rotational axis. Some robots still utilize conventional small DC motors for driving revolute joints [76].

Shape memory materials transform from one shape to another upon thermal, electrical, light or chemical stimulation [77]. The typical shape memory materials are: shape memory alloys (SMA) [31, 78, 74, 70], shape memory polymers (SMP) [69, 73] and their composites such as polyvinyl chloride (PVC) [79], and pre-stretched polystyrene (PSPS) [27, 80]. Among these materials, SMA generates the highest force-to-weight ratio, being compact and customizable for embedding by multi-layer lamination processes with the trade-off of slow response rate ($\approx$1 Hz), typical of shape memory materials, and low efficiency due to Joule heating that we address in this thesis.

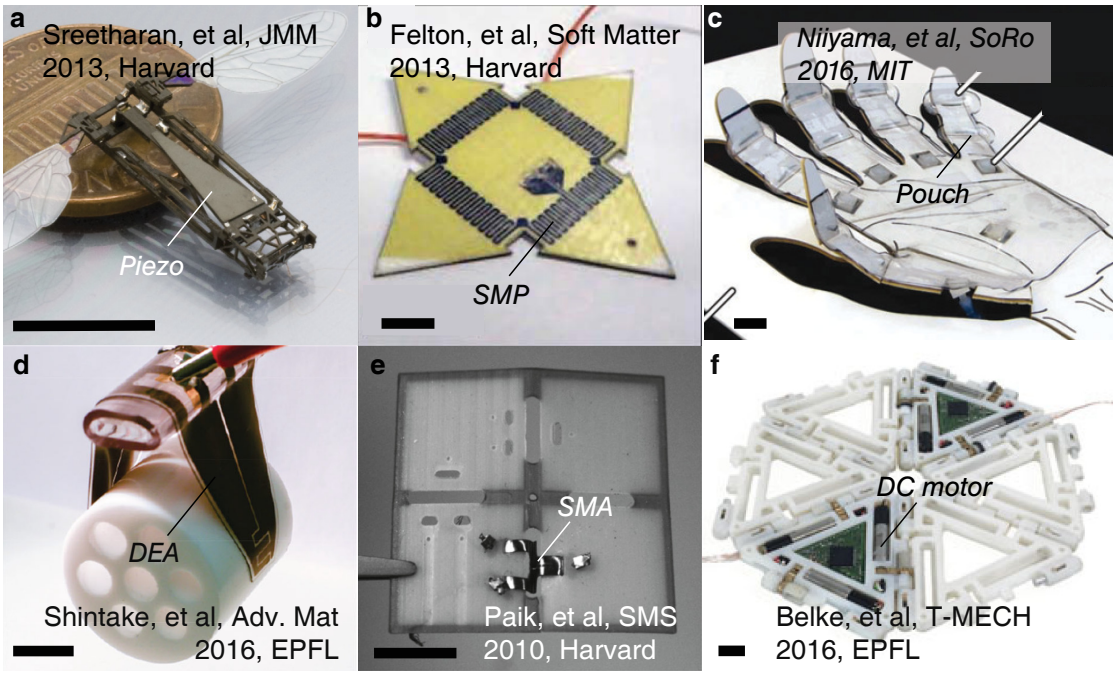


Figure 2.1 – **Existing actuator solutions for mesoscale mechanisms and robots. a**, the piezoelectric cantilever actuator that generates low stroke high frequency deflection when activated by high voltage periodic waveforms. **b**, SMP actuator with embedded heater layer shrinks when heated to generate a bending moment owing to offset from the neutral plane. **c**, the pouch actuators with sealed four sides inflate to generate a bending moment due to the curvature induced at the rotational axis. **d**, the dielectric elastomer actuator consist of two layers of stretchable electrodes (black) and elastomer material sandwiched between them. The elastomer squeezes and expands due to electrostatic forces upon high voltage and the electrodes can be selectively distributed to produce various motions.**e**, the torsional sheet SMA actuator programmed to cause twisting around the rotational axis. **f** the conventional approach for driving revolute joints using small DC motors. The scale bars correspond to 10 mm.

## 2.2 Shape Memory Alloy Actuators

SMA made of nickel and titanium compound (nitinol), has received wide interest from both research and industry due to its flexibility for programming various shapes, compactness, low weight and high force characteristics. Different types of SMA actuators have been developed, such as small stroke linear wire, large stroke helical linear spring [81], helical torsional spring [82] for angular deflection, twisting wire [83], twisting strips [84], bending torsional sheets [74] and their antagonistic arrangements for reversing motion [85] as an alternative to bulky conventional electric drives. SMA actuators are beneficial especially for applications concerning compact arrangements yet large displacement and forces in modular and self-reconfigurable robots [86], surgical tools [87], morphing wings [88], as well as for mesoscale origami robots [62].

### 2.2.1 SMA-based Minimal Mechanism Design

SMA actuators reproduce a wide range of mechanisms as they can be designed and programmed to generate desired motion and forces. While the conventional mechanisms are an integration of several discrete rigid components, such as motors, joints, gears and other elements, SMA actuators can fuse these all within a single, compliant, isotropic material or will require minimum number of components. Figure 2.2 shows the comparison of conventional mechanisms and their corresponding replication using SMA material. SMA actuator can act as a revolute or flexure joint when inactive and activate to actuate motion. Using a thicker material increases output torque or force without using additional transmission elements, whereas varying temperature stimuli between cold and hot states can vary stiffness. SMA material can store and release potential energy by means of additional locking and unlocking mechanisms, which is beneficial for power amplification.

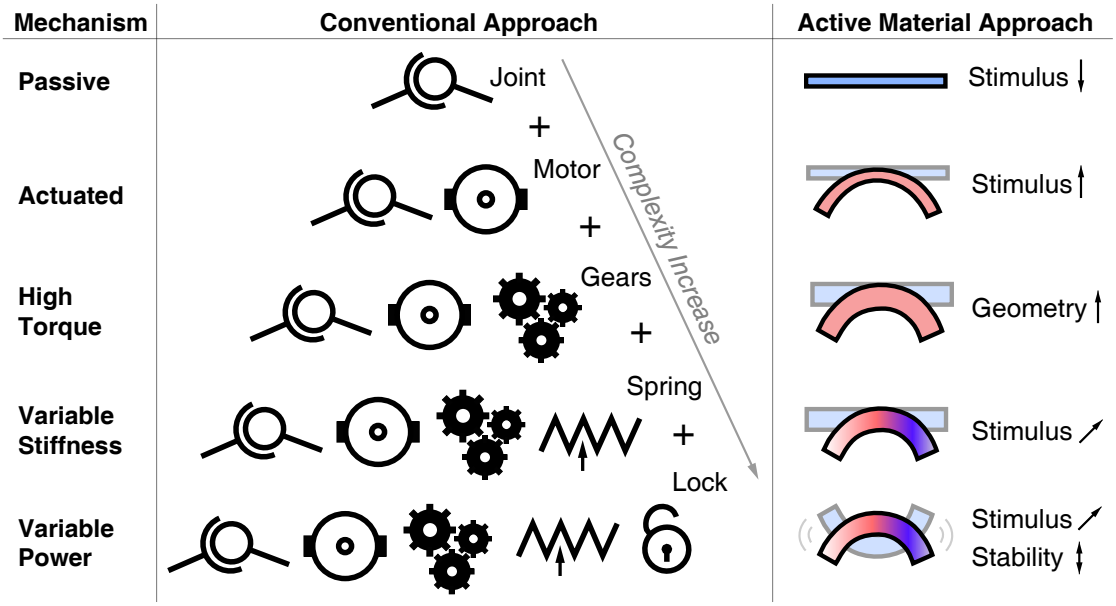


Figure 2.2 – **Conventional vs active material-based mechanisms design.** The conventional mechanisms are composed of multiple rigid components, such as joints, motors, gears etc. Depending on the functionality, the complexity can elevate as a result of increased number of components, which would hinder assembly. Active materials, like SMA, can act both as passive and active mechanisms depending on stimulus, geometry and mechanical instability owing to variable mechanical properties, shape and compliance, respectively. Hence, they enable minimal and compact actuation design for mesoscale robots.

### 2.2.2 Challenges of SMA-based Actuation

### 2.2.3 Performance

The performance of the SMA actuators is primarily related to their mechanical and material characteristics, such as metal composition ($N_i$-$T_i$ balance), geometry, fabrication process and

stimulus. While the metal composition defines austenite and martensite phase temperatures and usually set by the vendors, latter three parameters are vastly customizable to tailor force and motion. For instance, for a commonly employed helical spring SMA in Figure 2.3a, the number of turns defines its motion range, while the diameter of the wire influences the output force [81] expressed by

$$F_{Coil} = \frac{G(T)d^4}{8D^3N}\delta \tag{2.1}$$

Here, $\delta = \frac{ND\pi}{\cos\phi_i}(\sin\phi_f - \sin\phi_i)$ is the spring deflection, $d$ is the wire diameter, $D$ is the coil diameter, $N$ is the number of turns, $\phi_i$ and $\phi_f$ are the coil initial (compressed) and final (extended) pitch angles, and the shear modulus $G$ is the function of temperature $T$ and varies between the martensitic $G_M$ and austenitic $G_A$ values. Hence, SMA actuators stiffen proportionally to the applied heat stimulus between the martensite (cold) and austenite (hot) temperatures, whereas compression force increases exponentially with increasing $d$. Now, if we Joule heat the actuator, a wire with large cross-sectional area draws high current due to low resistance [97]. This reduces power efficiency as the vast amount of energy is dissipated as heat ($P = V^2/R$). This is an important consideration especially when using SMA actuators for untethered mesoscale robots owing to constraints on battery size, hence capacity.

The trade-off between power efficiency and force output is also applicable to other SMA actuator geometries, such as thin sheets [89], strips [84] among others [90] [91]. It is possible to convect heat employing heating chambers or ovens [84]. Although this method is useful for characterizing SMA actuators both thermally and mechanically, it is impractical for far remote applications concerning selective activation of multiple actuators. An alternative activation method based on heat conduction was proposed in [74] by means of an additional heater element with SMA torsional sheet actuator. The coiled heater element made of nickel-chromium wire faces the same limitations of helical SMA springs in terms limited resistance range and additional forming process.

Another shortage of SMA actuators is their limited actuation bandwidth to approximately 1 Hz. This is mainly due to slower cooling rate of the actuators compared to heating rate. Such slow response makes them inappropriate for high speed actuation required for jumping. The issue requires research into alternative methods to benefit from high force capacity of SMA actuators to produce high speed actuation.

#### Physical Form

For multi-layer mass-fabrication and folding assembly of mesoscale robots, the SMA actuator geometry plays a critical role for inlaying with minimal forming and mounting processes. Figure 2.3 depicts four typical functional layers that make up controllable composite joints: an

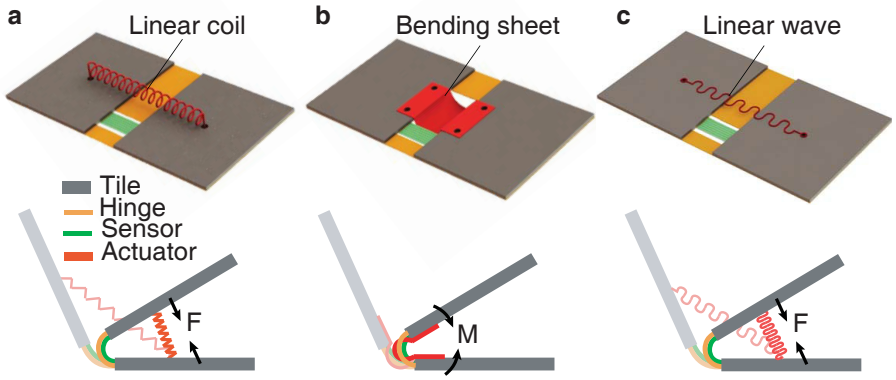


Figure 2.3 – **SMA-based actuation methods for driving mesoscale robot joints. a** compressible and extensible linear helical spring actuator mounted orthogonally to rotational axis of a flexible joint with sensor layer connecting two rigid tiles. **b**, the novel bending sheet Omega-SMA actuator placed in the same axis of rotation as the hinge for producing bending moment. **c**, the novel linear flat spring Wave-SMA actuator that overcomes limitations of helical actuators by low-profile design, no forming and assembly process. The latter two actuators are developed and studied as a part of the thesis work.

actuator, strain sensor, rigid tile and compliant hinge. SMA wire-based coiled actuators face limitations require meticulous winding process by inducing non-flat shape and adjusting pitch angles, which makes it challenging for assembly and integration into a multi-layer composite robots and mass-production. To overcome this limitation, the shape of the actuators should necessitates a minimal forming process and possess a low-profile shape to comply with layer-by-layer composition process.

### Modeling

Theoretically, SMA actuators can be programmed to generate any motion and force. From Equation 2.1 it is notable that SMA coil actuator is a complex mechanism that imparts intrinsic and extrinsic parameters such as shape, dimension, stress and temperatures. The motion can be reversed by introducing an antagonist pair [21, 74], designing a bidirectional motion [70], or relying on an elastic element. One key challenge is to set up a mechanism for producing desired forces and motion with reduced stress and strain, high efficiency and repeatability. For instance, SMA actuators designed for high motion range should not exceed the maximum austenitic strain of 1 % and martensitic strain of 6 % to avoid loosing memory over time.

Despite the extensive ongoing research on SMA material there are challenges in modeling thermo-mechanical characteristics of SMA since the material exhibits high non-linear hysteresis, essentially induced by temperature dynamics and stress [92]. Available constitutive models attempt to explain the thermal and mechanical relations along with SMA material properties. One of the most popular models is Tanaka's model [93], which considers phase transformation as an exponential function, whereas Liang-Rogers [92] improves the transformation term by

replacing it with a cosine function. The detwinned martensite case is further formulated by Brinson [94]. However, no model can relate temperature, load, and actuator geometry unless experimentally characterized. So designing a new type of SMA actuator necessitates modeling and characterization at different loading conditions to fully describe its behavior.

## 2.3 Helical Spring SMA-Based Minimal Mechanism for High Power Actuation

SMA actuators possess high power density at compact forms and achieve high deformations, however, their actuation speeds are limited (below 1 Hz) [95]. This creates substantial challenges for employing them for high speed mechanisms, such as robotic jumping, safety switches, or deployable systems. Jumping requires both high force and high speed actuation. Jumping is a common locomotion gait in small-scale terrestrial animals and is achieved by transferring muscle energy to elastic tendons, which can store this energy, and quickly release it through leg mechanism that interacts with the ground. This mechanisms is known as power amplification [15]. The main advantage of helical spring SMA actuators is that they envelop elasticity of spring and actuation in a single element, making a minimal design ideal for mesoscale locomotion mechanisms, creating a potential opposite to bulky, heavy, multi-component conventional approach described earlier in Section 2.2.1. While jumping is beneficial for clearing obstacles, adding other modes of locomotion, such as crawling or walking would allow terrestrial mobile robots to negotiate various terrain at reduced energy expense. If jumping requires high energy, crawling or walking requires relatively low power and combining them into a compact robotic body with minimal, yet tunable power mechanism suitable for mass manufacturing is a real challenge.

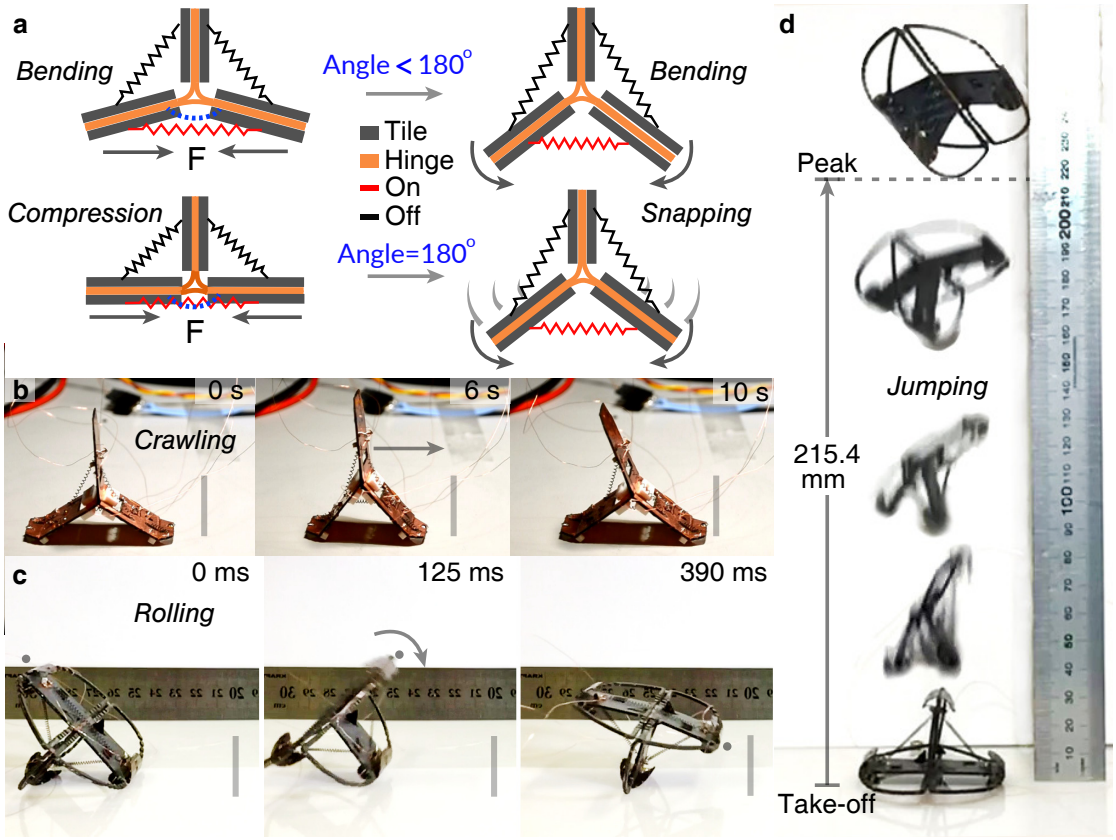


Figure 2.4 – **Bending and snapping fold mechanisms designed for inchworm crawling, walking and jumping locomotion of two versions of Tribot. a**, the robot legs close by compression force and the compliant joint, which connects the legs at the center, bends smoothly (continuous moment) at angles below 180° and snaps (discontinuous moment) to the side of the applied force at angles slightly greater than 180° due to instability. The smoothly bending property of the hinge produces inchworm crawling locomotion by stick-slip principle **b**, whereas the snapping mechanisms at the hinge right or left side generates walking locomotion by flipping onto two consecutive legs **c** and a vertical jump when the snap occurs at the hinge bottom **d**. The robot crawls with propagation of 6 mm on average, walks with 55 mm steps and jumps as high as 215 mm.

### 2.3.1 Variable Power Snapping Mechanism Design

We demonstrate for the first time, a mesoscale a versatile mechanism design capable of variable power output using spring SMA actuators. We utilize limit-point instability of compliant flexure hinges and bifurcation by selective activation of multiple actuators connected antagonistically as shown in Figure 2.4a. When a compliant joint is opened by a pair of spring SMA actuators slightly above $180^o$ and then compressed uni-axially by the third actuator, it experiences instability and snaps through to the applied force. The hinge generates a smoothly bending moment if the opening angle is less than $180^o$. The snapping power can be varied by adjusting the SMA temperature stimulus. In addition, the bending or snapping motions are

producible on any three sides of the joint. The minimal and compact snapping movement along with appropriate arrangement of the structure through selective activation of the actuators (red-ON or black-OFF) are adopted for inchworm crawling and jumping multi-locomotion mesoscale robot Tribot [61].

### 2.3.2 Minimal Multi-Locomotion Mechanism Design

The proposed Y-shaped mechanism requires three independently rotating rigid links connected by a single joint at the center. Using conventional revolute joints is not a viable option as it increases the size and complexity of the mechanism as each joint requires at least two kinematic pairs (pin and socket). Therefore, we designed a Y-shaped mechanism with rigid links and a flexure joint, which is folded from a composite of a rigid and flexible material to form the three-legged structure of Tribot as depicted in Figure 2.5.

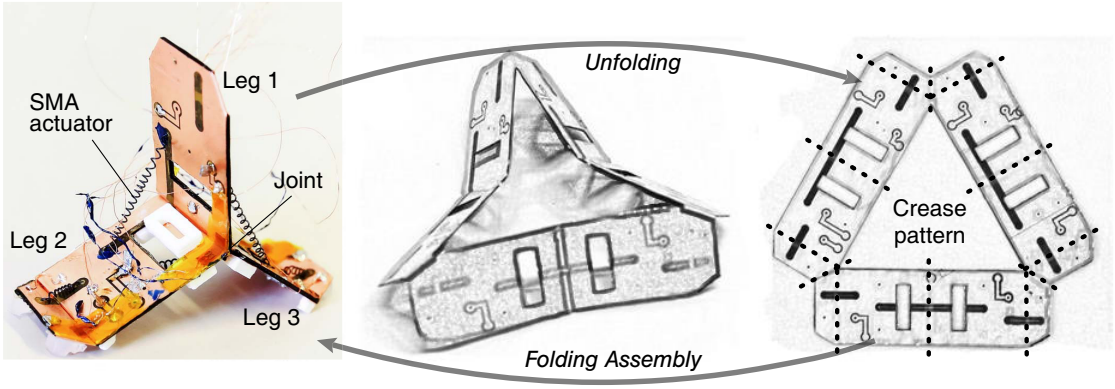


Figure 2.5 – **2D to 3D folding assembly process of a multi-locomotion origami robot Tribot.** The three-legged robot structure with planar rigid links and flexible joints are designed to embed a multi-locomotion mechanism driven by SMA spring actuators, then unfolded to a 2D crease pattern. The crease pattern is further decomposed into multiple functional layers with different geometry, such as flexible hinge, rigid tile, circuits, linear spring SMA actuators among others, each processed separately, combined together, and assembled by folding to make the robot body.

Robogami composite design of Tribot enables assembly of active, functional structures. This is essential to rapid manufacturing of complex shapes without assembling several separate 3D parts. We demonstrate this by folding assembly of Tribot, depicted in Figure 2.5. Owing to origami-inspired design, the robot addresses the key challenges of complex multi-locomotion mechanisms design with variable mechanical power. This complexity is originated from multiple mechanisms employed for performing different locomotion gaits and switching between them. However, since Tribot is made of a quasi-2D sheet of material, the design process is minimal and straightforward, while having several joints to perform different tasks and posses a scalable design. Initially, a 3D structure and mechanisms of the robot are defined and it is unfolded into multi-creased 2D pattern. Using a single material limits the functionality,

therefore, the pattern is decomposed into multiple functional layers for actuation, flexible hinges, structural backing, stopper among others. After processing each layer and stacking, the multimaterial composite is folded and assembled to produce Tribot's 3D structure with embedded mechanical functionality.

The final structure of the robot carries three legs, where leg 2 and leg 3 are used for maintaining contact with the ground while the upper leg helps to spread the lower legs when pushed downwards. To achieve bidirectional crawling, rubber pads under the foldable latches exert ground contact upon latch folding and unfolding. Hence, the crawling gait is generated by stick-slip movement of rubber latches in both direction (see Figure 2.4c). It uses the same compliant joints and set of SMA actuators for leaping up vertically by adjusting its body and producing a snap-through motion. The robot design benefits from symmetry, which allows having identical actuators on all joints. Tribot is a unique platform with minimal design and multifunctionality, assembled by folding. Tribot also flips to walk with average steps of 55 mm by snapping the side of the joint [96] (see Figure 2.4c) and hops vertically as high as 215 mm by snapping the joint bottom (see Figure 2.4d.)

Tribot is a unique mobile origami robot that can simultaneously choose between two modes of locomotion: jumping and crawling. When assembled, Tribot measures 64 x 34 x 20 $mm^3$, weighs 4 g, crawls at 17% of its body length per gait cycle and jumps seven times its height repeatedly without needing to be reset. To optimize the practicality of the nominally 2D design, we made two different approaches to build the prototypes. For one of them, we used the "traditional", monolithic, layer-by-layer robogami fabrication method and the second, we printed out most parts using a multimaterial 3D printer.

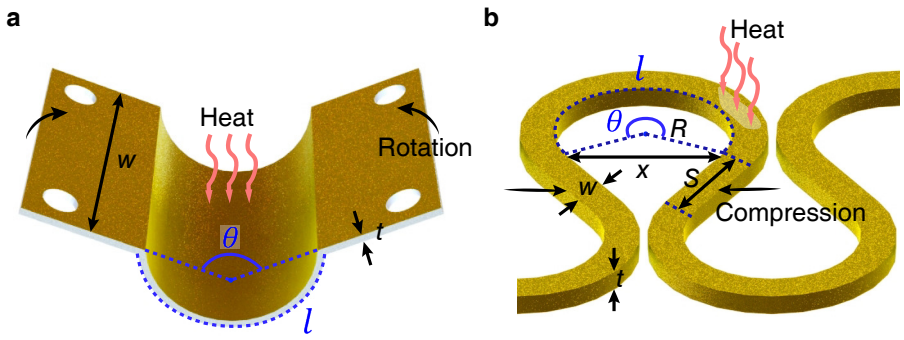


Figure 2.6 – **Two proposed SMA actuators and their operational principle.** **a**, the Ω-SMA torsional sheet actuator comprising planar and curved parts folds upon heat to generate a bending moment. **b**, the linear flat spring actuator is made of circular and planar regions with periodicity generates compression force in longitudinal direction due to circular part bending. **c**, the vacuum-driven folding actuator comprise a air-sealed chamber, closed with flexible membranes. The difference in rigid supports at the top and bottom membranes decides fold direction. The actuator folds upon negative pressure applied at the port connected to the chamber via a channel.

## 2.4 Bending Sheet Omega-SMA Actuator for High Torque and Power Efficient Actuation

In order to achieve high deflection angles for revolute motion and overcome the challenges of power consumption, we designed a bending sheet type SMA actuator as in Figure 2.3b. The proposed actuator is made of a thin sheet of $Ni_{50}Ti_{50}$ SMA (M alloy Memry GmbH) with 0.1 mm thickness. Its low-profile, slim, Ω-like shape has dimensions $12 \times 8 \times 2.5\ mm^3$, which closes upon heating as depicted in Figure 2.6a. It achieves approximately 180 ° of deflection when one end of the actuator is fixed and the other end is kept in plane at an angle of 0 °. The cylindrical hinge forms a circular curvature with a higher circumference compared to "U" geometry obtained by bending; resulting in a higher surface area for activation, a higher range of deflection and torque output and further the life-time of the actuator is prolonged [21]. Likewise, deformation of a U-shaped metal sheet to its initial flat form is not possible without large deformation due to small curvature at the hinge. Therefore, introducing curvature adds extra elasticity, while the two flat wings facilitate the actuator mounting in multi-layer lamination process as in Figure 2.3b.

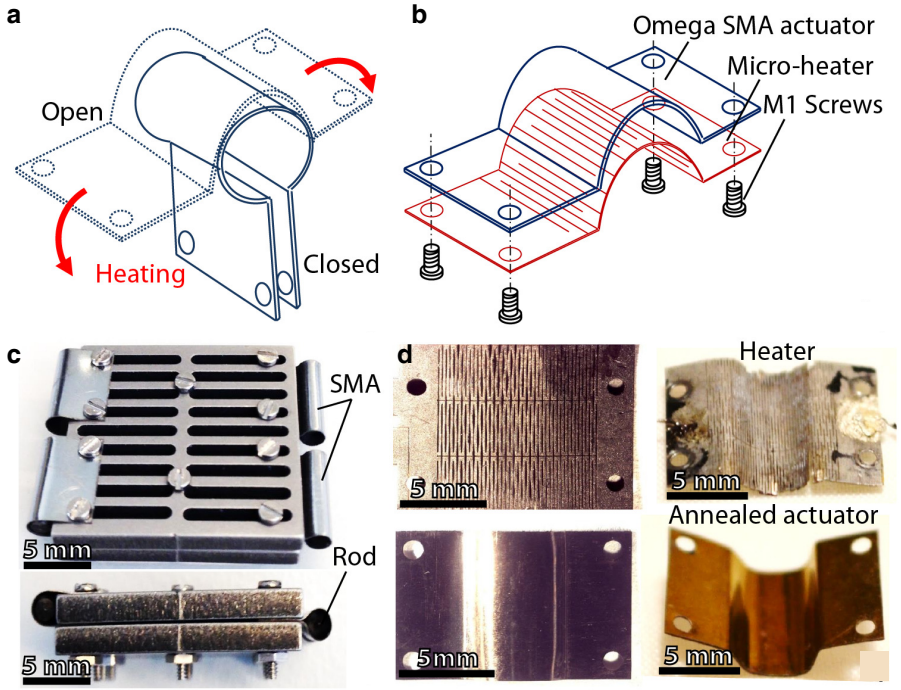


Figure 2.7 – **Omega-SMA bending actuator and heater design and fabrication.** **a** The Ω-SMA actuator is set to open configuration at room temperature and it closes when thermally activated. **b**, The actuator and flexible micro-heater layer assembly. **c**, clamping jig plates for annealing. **d**,the laser machined heater and actuator after annealing process.

As the Omega-SMA actuators possess low resistance, we use customized micro-heaters to conduct heat. The heaters are made of a Metal-polyamide (Kapton backed Ni-Cr alloy or

Copper) thin composite film and comprise several resistive paths, patterned in parallel to generate heat with current flow. This mesh design adds high flexibility to the film when folded or stretched, with negligible loading effect on the actuator. The heater layer eliminates dependencies on the SMA material resistance and can be tuned to deliver desired power output. The heater layer does not act as a short circuit, therefore the input power can simply be controlled by regulating the input voltage with no need for additional current amplifier electronics. Moreover, it allows allocating heat at specific sections, making it an effective activation method for multi-actuator systems.

Table 2.1 summarizes the available types of SMA-based torsion actuators in the literature without an antagonistic pair; their performance and the activation method is compared to the novel Omega (Ω) SMA torsional actuator we present in this paper. While the available actuators face challenges in certain aspects we discussed earlier, our Ω-SMA actuator, with its special design and micro-heater layer, outperforms the existing actuators. Given its miniature size, low weight of 0.07 g and consuming only 0.5 W of power, it has a high range of motion and a relatively high torque output of 34.1 mNm, with a torque-to-weight ratio of 486 mNm/g; filling the gap of trade-off between size, efficiency, range of motion and output torque.

Table 2.1 – Available SMA torsion actuators and their specifications

| **Actuator type** | **NiTi material** | **l × w × h (mm)** | **Activation and power** | **Range (deg)** | **Torque (mNm)** |
|---|---|---|---|---|---|
| Torsion coil spring [82] | wire d=0.5 mm | 10×7.2×7.2 | Joule heating, I not spec. | 138 | 0.7 |
| Torsion coil spring [97] | wire d=1 mm | 4×5×5 | Joule heating, 5 A | 120 | 350 |
| Twisting wire [90] | wire in PDMS d=0.2 mm | 70×15×3 | Joule heating, 1.25 A | 68 | 4 |
| Bending wires in parallel[91] | wire d=0.5 mm | 80×22×1.6 | Joule heating, 1.25 A | 40 | 55 |
| Twisting strip [84] | strip t=0.25 mm | 60×5×0.25 | Heating chamber | 180 | 70 |
| Torsion by linear motion[89] | sheet t=0.05 mm | 17×40×2.85 | Joule heating, 1.25 A | 120 | 3.75 |
| Y-shape torsion sheet [74] | sheet t=0.1 mm | 11×7×1.5 | Heater coil 0.19 A 13 V | 180 | 4.5 |
| Bidirectional torsion sheet [70] | sheet t=0.1 mm | 5×7×2.5 | Heater print-on 0.22 A 0.33 V | 180 | 4.2 |
| **Ω-SMA torsion sheet** | **sheet t=0.1 mm** | **12×8×2.5** | **Micro-heater 0.13 A 3.7 V** | **180** | **34.1** |

### 2.4.1 Omega-SMA Actuator Modeling

In this subsection we provide the analytic model of the Ω-SMA actuator, relating bending equations and the thermo-mechanical behavior of the SMA sheet.

#### Mechanical Model

For the Ω-SMA actuator, the curvature length of the hinge is much larger than the actuator thickness, therefore bending can be considered as pure bending. The strain, stress and the bending angle are given by:

$$\epsilon = \underbrace{\frac{y_n}{l}}_{C_1} \underbrace{atan2\left(\frac{y}{x}\right)}_{\theta}, \; \sigma = \underbrace{\frac{6}{wt^2}}_{C_2} \tau \tag{2.2}$$

where $\epsilon$ and $\sigma$ are the strain and stress, $\theta$ is the bending angle of the actuator moving arm on the $x-y$ Cartesian coordinate plane, $y_n$ is the distance from neutral plane approximated to actuator half-thickness, $l$ is the hinge curvature length, $\tau$ is the torque equivalent to moment generated by each infinitesimal layer on the hinge, $w$ and $t$ are the width and thickness of the actuator, respectively.

#### Thermo-Mechanical Model

We have adopted the Liang-Rogers SMA constitutive thermo-mechanical model [92] due to its relatively high accuracy in predicting material behavior. The one-dimensional model of SMA is given by:

$$\sigma - \sigma_0 = E(\epsilon - \epsilon_0) + \Omega(\xi - \xi_0) + \Theta(T - T_0) \tag{2.3}$$

where $E$ is the Young's modulus, and Ω and Θ are the transformation and thermal expansion coefficients respectively. $\sigma$, $\epsilon$, $\xi$, T are the stress, strain, martensite volume fraction and temperature with their initial conditions $\sigma_0$, $\epsilon_0$, $\xi_0$, $T_0$, respectively. (2.3) can be further simplified by omitting the thermal part since strain caused by thermal expansion is much smaller than that of phase transformation. For a shape memory alloy material, Young's modulus changes with phase transformation and is given by:

$$E = \begin{cases} E_M & \text{if } \xi = 1 \\ E_A & \text{if } \xi = 0 \end{cases}$$

here, $E_M$ and $E_A$ are the elastic modulus of the SMA at full martensite and full austenite phases, respectively. The phase transformation coefficient can be expressed as $\Omega = -\epsilon_L E$ where $\epsilon_L$ is the maximum recoverable strain. By substituting strain and stress expressions in (2.2) into (2.3), the model relating torque to material properties can be written in the following form:

$$\tau - \tau_0 = C_3 E(\theta - \theta_0) - C_3 \theta_L E(\xi - \xi_0) \tag{2.4}$$

where $\theta_L$ is the maximum recoverable angle and $C_3 = C_1/C_2$. In an unloaded condition ($\tau = \tau_0 \approx 0$) with initial phase at full martensite, the bending angle can be computed from (2.4) as:

$$\theta = \theta_0 + \theta_L(\xi - 1) \tag{2.5}$$

$E_A$ and $E_M$ can be computed by:

$$E_A = C_3^{-1}\frac{\tau_{max}}{\theta_0},\ E_M = C_3^{-1}\frac{\tau - \tau_0}{\theta - \theta_0} \tag{2.6}$$

and the stress induced coefficients $C_A$ and $C_M$ can be computed for both heating and cooling processes ($M \rightarrow A$ and $A \rightarrow M$) respectively by:

$$C_A = \frac{E_A}{A_f - A_s},\ C_M = \frac{E_M}{M_s - M_f} \tag{2.7}$$

Finally, the martensite fraction composition is given as cosine functions during the phase transformation from martensite to austenite and austenite to martensite in the following form:

$$\xi = \begin{cases} \frac{1}{2}\cos\left[a_A\left(T - A_s - \frac{C_2}{C_A}\tau\right)\right] + \frac{1}{2} & M \rightarrow A \\ \frac{1}{2}\cos\left[a_M\left(T - M_f - \frac{C_2}{C_M}\tau\right)\right] + \frac{1}{2} & A \rightarrow M \end{cases}$$

where the material constants $a_A = \frac{\pi}{A_f - A_s}$ and $a_M = \frac{\pi}{M_s - M_f}$. Here, $A_s$, $A_f$, $M_s$, $M_f$ are the austenite start, austenite finish, martensite start, martensite finish temperatures, $a_A$ and $a_M$, are the austenite and martensite material constants, respectively. These eight parameters along with $E_A$ and $E_M$ values can be determined through characterization experiments.

### 2.4.2 Actuator Characterization

Actuator choice requires a full understanding of the mechanical performance. We have thoroughly examined the Ω-SMA actuator for its response in various thermal and mechanical conditions. Experiments in this paper, shows three testing conditions: no load, applied load, and blocked load conditions. The unloaded tests define $A_s$ and $A_f$ temperatures of the actuator. The material elastic coefficient $E_M$ and stress induced coefficient $C_M$, can be determined by loading the actuator at room temperature, where $E_A$ and $C_A$ are characterized by a blocked test at $T > A_f$. Two test setups were designed for this purpose; the setup for angular rotation measurement at no load and the force measurement setup for loading conditions. In free rotation (see Figure 2.8a, two small rectangular tiles are mounted onto the actuator at both ends. The glass fiber-reinforced layer, fabricated via micro-laser machining system has an extremely low weight, alleviating load. In this arrangement, one of the arms is clamped and kept stationery while the other arm can rotate freely along the actuator torsion trajectory. Red mark on the moving arm enables tracking of the angular deflection of the actuator arm using a video camera (Nikon D3100) placed above the actuator axis of rotation while an IR thermal imaging camera (FLIR A35) is pointed at the back surface of the actuator hinge to measure its temperature. A microcontroller (Arduino Nano) is used for adjusting the level of the input power by PWM duty cycle modulation. A power source of 3.7 V DC output is connected to a transistor switch. The transistor is switched by the PWM signal from the microcontroller. Hence with this method, desired power flow to the micro-heater layer can be regulated in an efficient manner since the input power is directly proportional to the PWM duty value.

The force measurement apparatus depicted in Figure 2.8b consists of two rectangular metallic plates forming a closing or opening hinge. Similar to the previous arrangement, one of the arms is kept stationery and mounted on the high precision force sensor (Nano17 ATI Industrial Automation) while the moving arm is mounted on the moving plate driven by a DC motor with an embedded encoder (A-max16 Maxon Motor AG). The motor in the setup can be positioned at the desired angle using the commercial controller board (ESCON 36/2 DC, 4-Q Servocontroller). SMA loading can be performed by driving the motor at constant rate and blocked torque tests can be realized by halting the motor at various angles and activating the actuator. Here, real-time temperature measurement is performed employing the same thermal camera described in the first setup and force is measured using load cell and position data of the DC motor provided by the encoder.

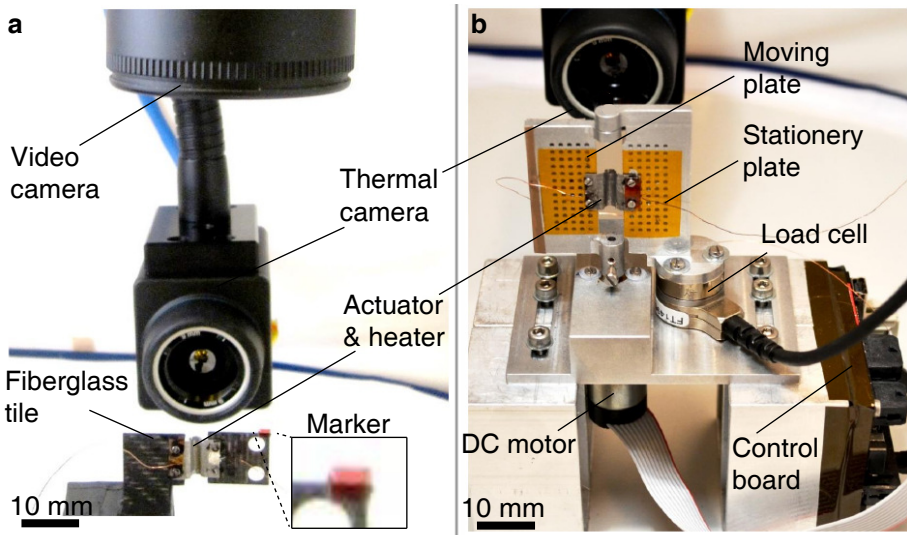


Figure 2.8 – Ω-**SMA actuator characterization setups. a**, the free load setup with temperature measurement using IR thermal camera and angular position tracking using video camera. **b**, the loading setup with temperature measurement using the IR thermal camera, angular position by the motor encoder and force measurement is done by load cell.

### Load-Free Test

We employed load-free angle-temperature measurement to determine $A_s$ and $A_f$ temperatures by heating the actuator with no load applied, and $M_s$ and $M_f$ temperatures in the cooling process of the actuator. The torque-free test setup is utilized and the procedure is as follows: first the actuator is manually set to open configuration at room temperature as in Figure 2.8a, then the heater is activated by giving input power and the actuator moves to a closed configuration. The video camera placed above the actuator captures the torsional angle of the actuator while the thermal camera concurrently records the hinge temperature. Different input power levels are tested in order to study power influence on actuator response time. Figure 2.9a shows the actuator angular displacement for three different input power levels and the corresponding measured temperature for each case in Figure 2.9b. Here, the actuator is activated until a closed configuration is reached then cooled down using a PC fan. The fan is employed to expedite the experimental process and does not alter actuator's $M_s$ and $M_f$ characteristic temperatures. However, for robotic applications with multiple actuators in the system, natural cooling can be considered with slower cooling rate which in our case was approximately 50 % slower than the cooling rate with the fan. From Figure 2.9a it is noticeable that the slope of the data curve steepens with higher power inputs since higher power increases the activation rate. This is even more evident when we deduce the velocity information given in Figure 2.9c by differentiation and filtering the angle data given in 4a. For each input power, the cooling process that involves turning off the heater and turning on the fan is initiated after full closed configuration of the Omega-SMA. Input temperature and output angular deflection for heating and cooling processes is summarized in Figure 2.9d.

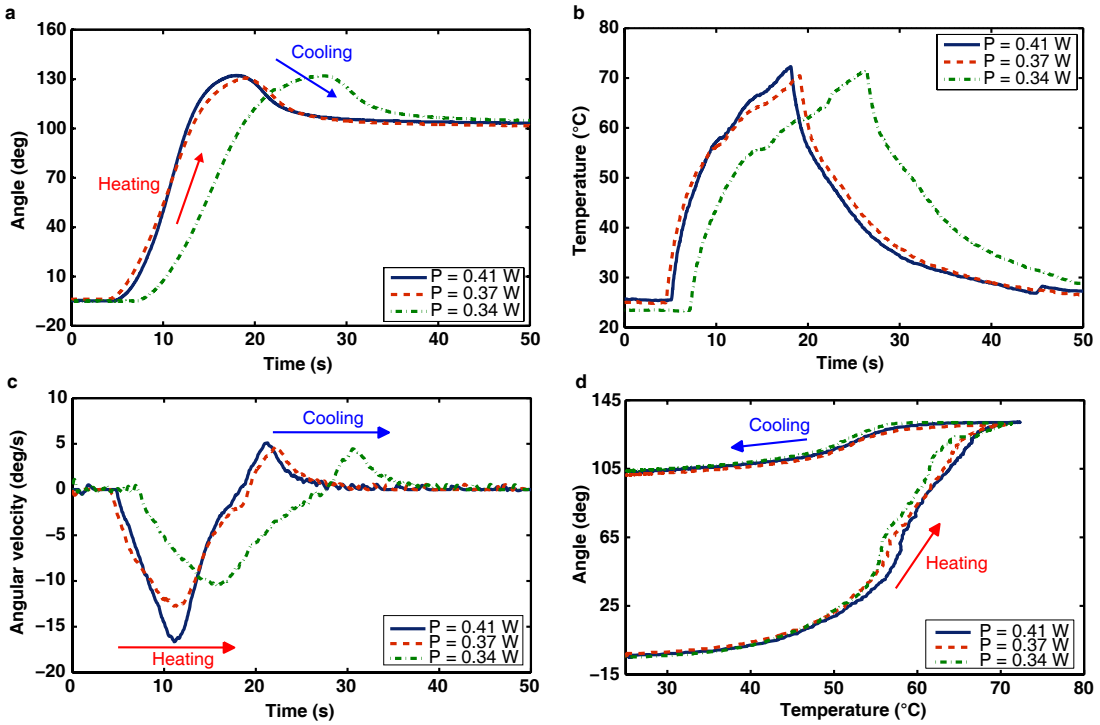


Figure 2.9 – **Ω-SMA actuator load-free characterization plots. a**, the angular displacement for different Joule heating powers that set different temperatures. **b**, the measured temperatures of the actuator. **c**, the angular velocities of the actuator. **d**, the angular deflection to temperature relation.

The maximum angle of deflection for heating is measured at $\theta$ = 132 ° due to mechanical constraints introduced by the screws used to mount the actuator-heater layer to the glass fiber tiles. The screw heads from both ends of the actuator make contact while closing. The maximum recoverable angle is measured at $\theta_L$ = 102 ° after cooling.

The experimental plot for heating and cooling processes along with the calculated model is given in Figure 2.9. Experimental data for input power P = 0.37 W is considered in this case. Approximate values of $A_s$ and $A_f$ are evaluated from the experimental plot for heating process ($M \rightarrow A$) where $M_s$, $M_f$ and $\theta_L$ values are determined from the cooling procedure ($A \rightarrow M$). These parameters are employed to compute the analytic relation in 2.5. Since this test considers no effect of load, stress-induced terms in the martensite volume fraction for phase transitions can be omitted by setting $\frac{C_2}{C_A}\tau = \frac{C_2}{C_M}\tau = 0$, and $T$ is taken as the actual measured temperature of the actuator for P = 0.37 W. As a result, the model complies relatively well with the experimental results with maximum deviation of 11.3 %. $A_s$, $A_f$, $M_s$, and $M_f$ values obtained from the model fit are summarized in Table 2.3.

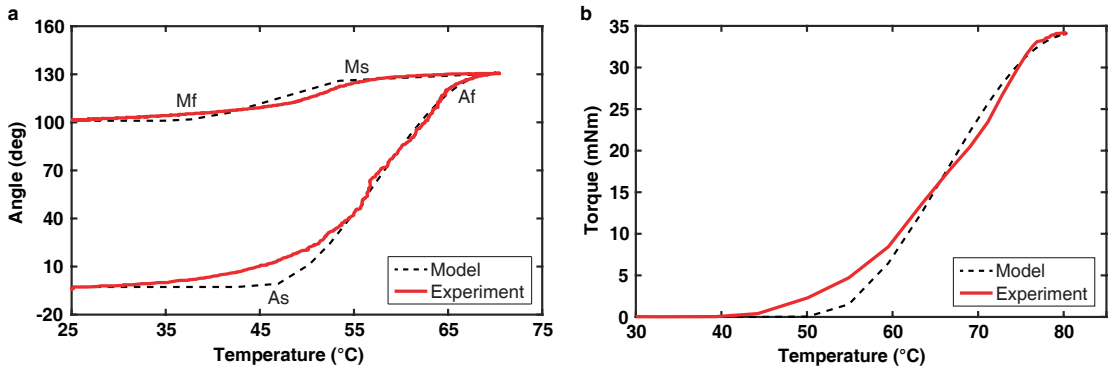


Figure 2.10 – **Load-free and loaded experimental vs analytic model comparison. a**, the experimental angular deflection for the load-free test and the computed using the model. **b**, the measured blocked torque at $\theta = 90\,^{\circ}$ and the calculated using the model.

### Blocked Torque Test in Austenite

The blocked torque test determines the maximum torque $\tau_{max}$ generated by the actuator at $T > A_f$. In this test, we performed blocked force measurements at different angles and then torques are calculated by multiplying by the length of the moment arm. Initially, the actuator is mounted from both sides to metallic plates onto the blocked force setup in open configuration. It is then heated to $T > A_f$ for approximately 22 seconds to maintain the maximum torque. The same procedure is repeated for angles $0\,^{\circ} \leq \theta \leq 150\,^{\circ}$ with concurrent force and temperature measurement. Figure 2.11 shows the maximum torque measured at each angle. The maximum torque is measured as $\tau_{max} = 34.1$ mNm at angle $\theta = 90\,^{\circ}$. Using the blocked torque measurement at this angle, $E_A$ and $C_A$ values are computed using (2.6) and (2.7), and included in Table 2.3.

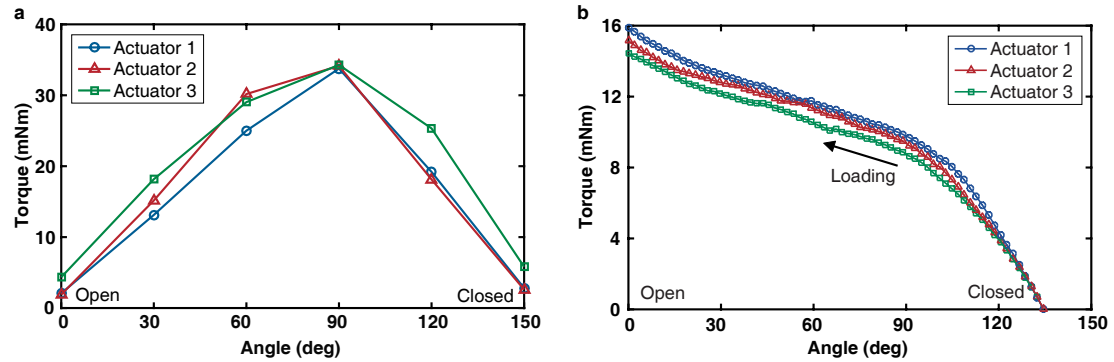


Figure 2.11 – **Loading characterization plots for three actuator samples. a**, the blocked torque measured at different angles with 30 ° interval **b**, the measured torque for loading at full martensite phase.

The experimental blocked torque for heating process at $\theta = 90\,^{\circ}$ and the corresponding computed model is depicted in Figure 2.10. The temperature of the actuator was limited to

Table 2.2 – Summary of the actuator parameters

| Parameter | Value | Unit |
|---|---|---|
| $M_s$, $M_f$, $A_s$, $A_f$ | 53.4, 37.8, 47, 67 | $°C$ |
| $E_A$, $E_M$ | 34.1, 19 | GPa |
| $C_A$, $C_M$ | 1.11, 0.44 | GPa/$°C$ |
| $\tau_{max}$ | 34.1 | mNm |
| $P_{max}$ | 0.47 | W |
| $\tau_{max}$/weight | 486 | mNm/g |

82 °C so that complete austenite phase is attained. The torque starts to gradually increase with the temperature increment until it settles at 34.1 mNm. Increase in phase transition temperatures can be observed due to the stress induced by blocking or maximum loading condition. This phenomena of the SMA transformation temperature changing properties due to stress, is included as stress induced terms $\frac{C_2}{C_A}\tau$ and $\frac{C_2}{C_M}\tau$ in martensite fraction equations given in the previous section. For $M \rightarrow A$ the formulation in (2.4) yields $\tau = \tau_{max}(1-\xi)$ where $T$ in $\xi$ is taken as the actual measured temperature of the actuator at $\theta = 90$ °. Approximate values of $A_s = 50$ °C and $A_f = 80$ °C from the experiment are substituted into the model given in (2.4) and the maximum error is computed as 9.4 %.

#### Loading Test in Martensite

In this test, mechanical properties ($E_M$ and $C_M$) of the actuator at room temperature ($\xi = 1$) are evaluated by loading at constant rate using the force measurement setup from the previous test. The procedure is as follows: one arm of the Ω-SMA actuator is kept clamped to one of the metallic plates while the other arm is left free to slide along the other plate, but constrained in the perpendicular direction to the plate using a 3D printed clamp with clearance as a guideway. Its initial position is set to $\theta$=135 °, then the moving arm is rotated applying load towards $\theta = 0$ ° at constant velocity, and the reaction force of the actuator is recorded as shown in Figure 2.11b. The maximum torque measures around 15.1 mNm at $\theta = 0$ ° which displays lower stiffness compared to those at complete austenite phase since $E_A > E_M$. Elastic modulus $E_M$ is determined using (2.6) where the linear region between $90 \leq \theta \leq 135$ ° is considered and $C_M$ is computed by (2.7). The calculated parameters of the result are summarized in Table 2.2.

### 2.4.3 Application: Self-Reconfigurable Robotic Origami Surface

In order to demonstrate the actuator's application in low-profile quasi-2D mesoscale robots or Robogamis, we designed, fabricated and assembled multiple modules, each consisting of the following functional elements: the actuator, heater, curvature sensor and the triangular tile as depicted in Figure 2.12a. A modular design approach for a robogami augments the

simplicity of the design and assembly process with modifiable elements. Each tile, made of glass fiber, contains two extra pairs of holes for attaching other modules. Hence, besides being able to change each functional component, the proposed method allows us to achieve additional freedom by altering the surface size and consequently increasing or decreasing DoF by mounting additional modules or dismounting them by two pairs of M1 screws, respectively.

We adopt commercial strain gauges (RS Components Ltd) for curvature angle measurement as depicted in Figure 2.12b. The sensor undergoes relatively high resistance changes for bending strains. Since the actuator has one-way deflection, the sensor layer here acts as a bias element to partially reverse the actuator motion while cooling. Thus, the sensor is sandwiched between 50 $\mu$m thickness Kapton tapes in order to improve stiffness and also thermal insulation. Characterization test results provided in Figure 2.12b show approximately linear resistance change of the sensor for angular deflection of the actuator upon activation. Here, a similar experiment as with the load free test is carried out with the sensor mounted across the actuator hinge as shown in Figure 2.12a and characterized in a single direction from open to closed configurations. The deflection angle is captured using a video camera where the resistance value is measured using a digital multimeter (NI USB-4065, National Instruments) interfaced with LabVIEW software (National Instruments). It is worth mentioning that due to the elasticity of the sensor layer, it adheres to the curved shape of the actuator and heater hinge after multiple bending cycles as shown in Figure 2.12b. However, there is no contact between the sensor and heater layers; therefore, the heat effect on the strain sensor is minimal.

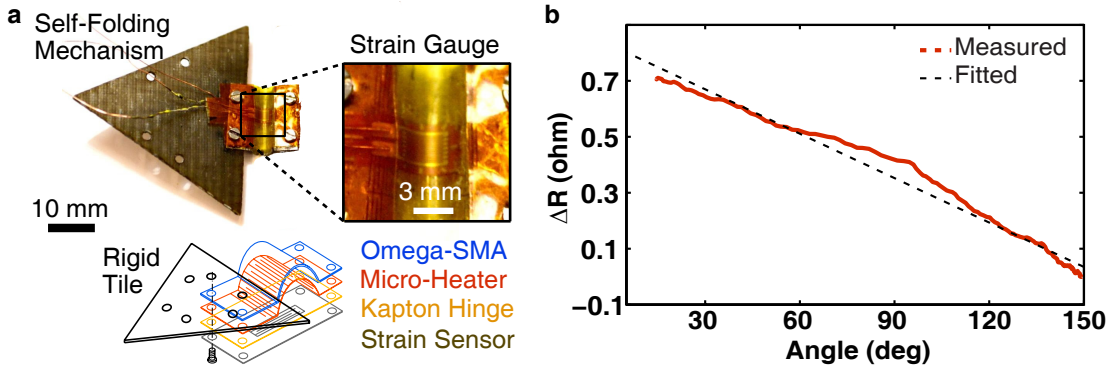


Figure 2.12 – **Multi-layer composite active joint design with Ω-SMA actuator and angular sensor. a**, the composite flexure joint emdeds Ω-SMA actuator, micro-heater, strain gauge sensor, flexible Kapton hinge and fiberglass rigid tiles. Each layer is stacked one on top of the other and mounted by M1 screws for integrity. **b**, the angular response of the strain sensor shows linear behavior and minimal effect of the heat dissipating from the micro-heater layer.

### Controller design

There are generally two control goals for SMA actuators: position and force. Control parameters can be resistance, temperature, position or force feedback. Our application focuses on the robogami system with multiple creases that can self-fold into different 3D shapes. Therefore,

accurate position control of the actuators is essential to achieve the versatile shapes. We present here angular position control of the Ω-SMA torsional actuator by PWM duty modulation of power input. Since we are only interested in accurate positioning of the actuator, we designed our controller based on angle feedback from the bending strain sensors described earlier. Different from our previous work on an on-off controller of SMA actuators [98], here a PI controller is adopted to achieve desired positions for each actuator.

The controller design is as follows: if a closing hinge with a measurable bending angle $\theta$ is considered, then the control goal within PI controller framework can be written as

$$D = K_p(\theta_{set} - \theta) + K_i \int (\theta_{set} - \theta) \tag{2.8}$$

where $D$ is the PWM duty value of the power supplied to the heater, $K_p$, $K_i$ are the proportional and integral gain constants to minimize the error in bending angle which is the difference between the set angle $\theta_{set}$ and the measured angle $\theta$ coming from the strain sensor. In order to avoid over-heating of the actuator, we introduced limiting functions for the controller duty value output as

$$D = \begin{cases} D_{lim} & \text{if} D > D_{lim} \\ 0 & \text{if} D < 0 \end{cases}$$

where the limiting duty value is a positive real number between $0 \leq D_{lim} \leq 1$.

**Results**

In order to evaluate the effectiveness of the method, the setup given in Figure 2.13 is employed to test a robogami surface with four tiles, illustrated in Figure 2.14. It consists of three actuated modules to demonstrate the capability of constructing various shapes in 3D space by the selective activation of three actuators and controlling the folding angles. The setup is as follows: three independent PWM duty control outputs from the microcontroller are supplied to control the switches S1, S2 and S3, hence regulating the power flow to the heaters at modules M1, M2 and M3. The resistance changes in the strain sensors R1, R2 and R3 are acquired by the digital multimeter. We overcome the limited number of channels available on the digital multimeter by including a multiplexer (MUX) for buffering and feeding data through a single channel to the digital multimeter communicating with the LabVIEW interface. The resistance data is extracted in LabVIEW then converted to angles using the characterization plots given in Figure 2.12b. Then these angle values are further represented as analog voltages V1, V2 and V3 and sent to the microcontroller through a data acquisition board (DAQ USB-6008, National Instruments) closing the loop. In this arrangement, we take advantage of using a single power

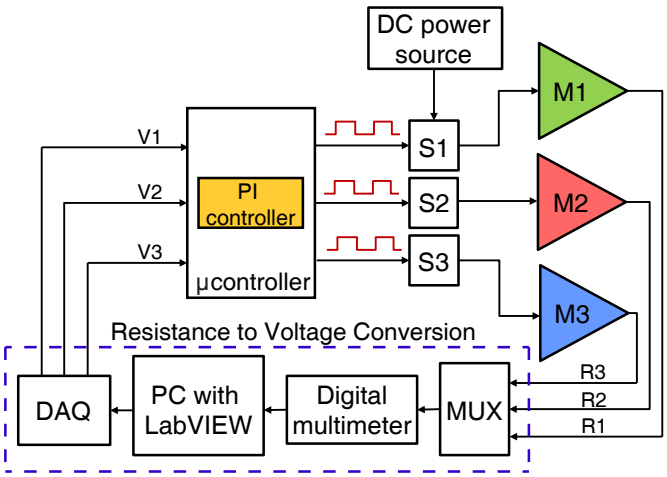


Figure 2.13 – **Control setup for self-reconfigurable robogami surface.** S1, S2 and S3 denote the transistor switches for regulating DC power flow to modules M1, M2 and M3 with PWM signals. Multiplexer MUX is employed for buffering three strain gauge resistance signals R1, R2 and R3 and sending to the digital multimeter through single channel. The signals are parsed, processed and then fed to the microcontroller circuit by means of data acquisition board DAQ as analog voltages V1, V2 and V3.

supply and handling multiple control and feedback signals independently.

The angular control response of each actuator at three modules along with the reference angle is shown in Figure 2.14b. The system is initially at rest then $\theta_{set} = 90\,^{\circ}$ is set as reference to SMA 1 and 3 while no reference is given to the SMA 2. Then a reference of $\theta_{set} = 110\,^{\circ}$ is given to all three actuators in order to form shape 3; the tetrahedron. Some variation in the actuator angles is due to minimization of the error when the set point is attained. Here, the duty cycle becomes close to zero, thus the heater becomes inactive for short time, the actuator cools down at that moment decaying from the reference angle until it is activated again to attain the set point.

## 2.5 Linear Flat Spring SMA Actuator: Wave-SMA

Conventional helical spring type actuators possess capability to store great amount of potential energy superior to bending actuators. However, they require meticulous manual shaping process and integration into a multi-layer composition process that hinders further use for mass-producable mesoscale robots. In order to address the shortage of helical spring actuators, we developed a novel flat spring SMA actuator, called Wave-SMA, depicted in Figure 2.15a. Cut from a thin sheet of nitinol sheet in the form of periodic waves with reciprocating circular loops, these actuators extend and contract in longitudinal direction to produce compression force by bending moment. It requires only cutting of an pre-annealed flat sheet of SMA into waveform with desired geometry enabling great customizability. Our approach allows

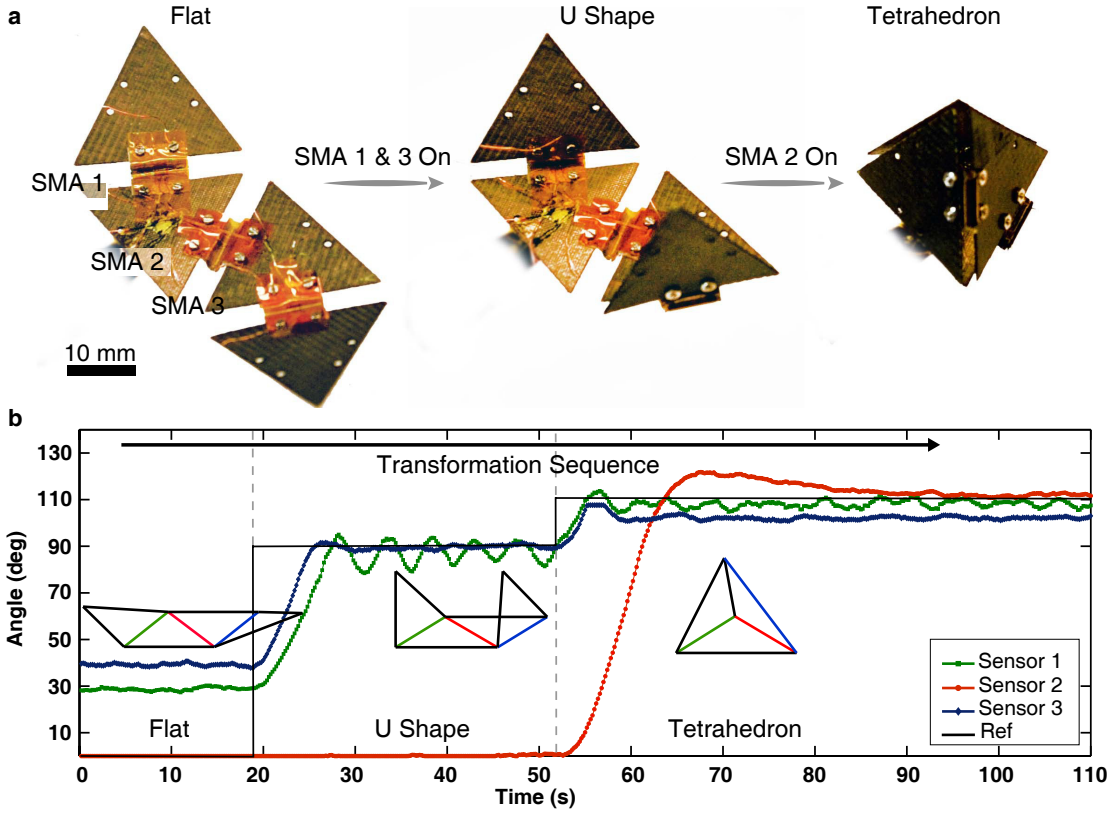


Figure 2.14 – **Transformation sequence of the robogami reconfigurable surface and controller performance. a** the robot undergoing a shape change from the initial resting flat shape to U-shape with 90 ° angle reference for two joints at the sides, then to the tetrahedron where all three joints reach a 110 ° angle forming a tetrahedron. The schematic shows the transformation sequence with hinges colored with respect to SMAs. **b** the closed-loop response of the SMA actuators at three joints along with reference angles.

for batch fabrication of several actuators without any assembly steps, therefore, it enables mass-production. We experimentally characterize their performance and demonstrate their application in a reconfigurable suction gripper.

### 2.5.1 Wave-SMA Characterization

To assess the force capability of the actuators, we performed characterization of different actuator geometries under uniaxial load. Figure 2.16 shows the forces measured for actuator samples with different width 200 $\mu$m and 250 $\mu$m, and radius of curvature 5 mm and 7.5 mm. The actuators are loaded to reach maximum of 30 % deflection to ensure only bending in the longitudinal direction without twisting out of plane in both martensite (room temperature) and austenite (65 $C^o$) phases. The results show that the samples with larger cross section area produce higher forces and the behavior is nearly linear for both phases.

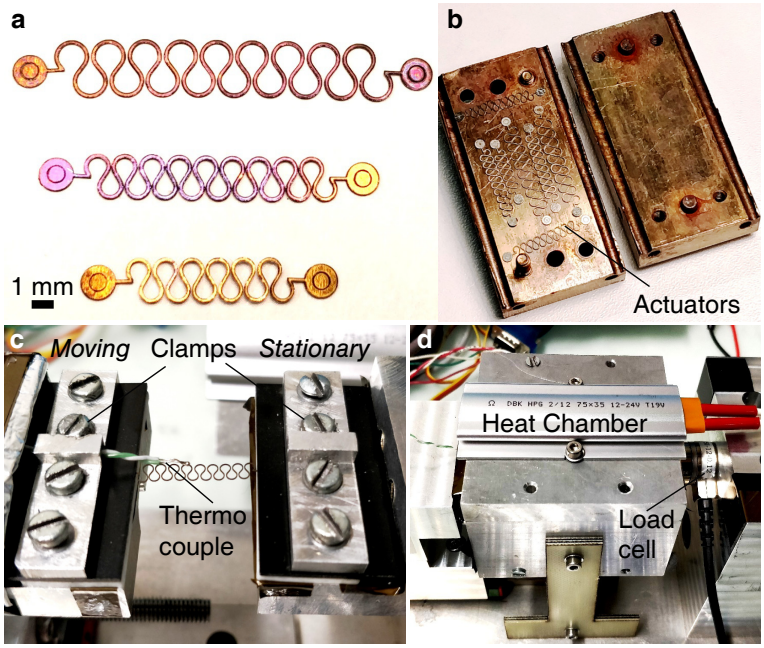


Figure 2.15 – **Wave-SMA actuator fabrication and characterization setups.** **a**, the actuator samples with different geometric parameters fabricated by laser cutting **b**, the batch fabrication setup made of two metal jig plates for thermally annealing of several flat actuators. **c**, the tensile tester setup with moving and stationary stages for loading actuator samples clamped between the stages. **d**, the testing machine is enclosed with a heater chamber for austenite setup and the temperature is controlled by feedback from the thermocouple element placed inside the chamber.

### 2.5.2 Wave-SMA Composite Design

Composite design enables embedding different functionality within material layers and expands design freedom. To this date, SMA actuators are designed and considered as a single isotropic material with functionality limited to mechanism parameters (Equation 2.1) that they impart. We noted that increasing the wire diameter for a helical spring actuator would elevate its pulling force, however, at the cost of high current consumption and slow cooling rate due to increased mass (energy to dissipate $Q = mc\Delta T$). So this is a fundamental trad-off for Joule-heated actuators. Our Omega-SMA actuator on the other side are compact and are relatively easier to integrate into composite structures, however, by only reciprocating the structure due to non-flat geometry. Fusing them into more complex composite mechanisms such as sandwiching multiple back-to-back in parallel to increase torque would deter performance owing to layer interference and non-uniformity of the neutral plane while bending. It is also impractical to manufacture multiple actuators, form the omega shape, anneal, and then combine.

To address the above-mentioned challenges, we propose a flat spring actuator composite design for building tunable actuation and mechanism layers as depicted in Figure 2.17. Figure

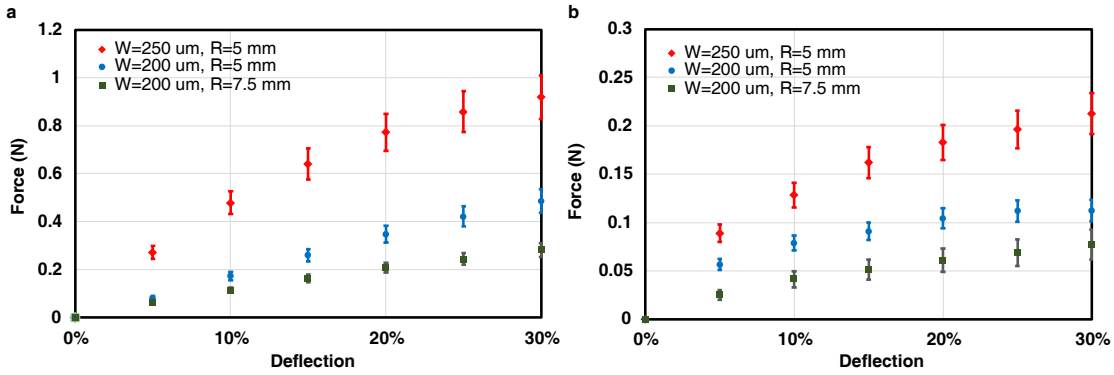


Figure 2.16 – **Wave-SMA actuator loading results vs model. a**, the loading results for actuator samples in austenite state with different width and curvature radius. **b**,the loading results for actuator samples in martensite state with different width and curvature radius. The measured tests validate the model.

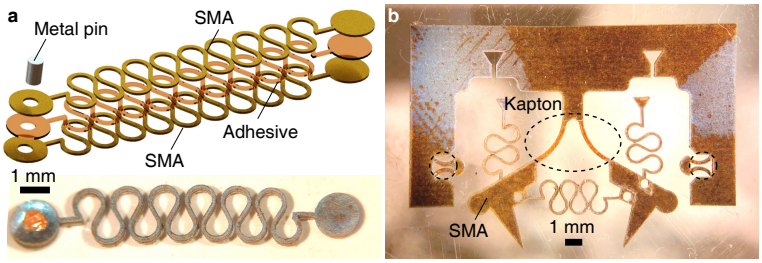


Figure 2.17 – **Wave-SMA actuator fabrication and characterization setups. a**, the actuator samples with different geometric parameters fabricated by laser cutting **b**, the batch fabrication setup made of two metal jig plates for thermally annealing of several flat actuators. **c**, the tensile tester setup with moving and stationary stages for loading actuator samples clamped between the stages. **d**, the testing machine is enclosed with a heater chamber for austenite setup and the temperature is controlled by feedback from the thermocouple element placed inside the chamber.

2.17a shows a multi-layer composite linear actuator cut out from a laminate of two SMA sheets and adhesive layers sandwiched between the sheets. The number of actuator layers increases the pulling force proportionally yet in a compact form. The adhesive layer ensures structural integrity and serves as an electrical insulator, so that the actuators can be connected in series by inserting a metal pin on one side. This increases resistance of the actuator ($R = \frac{\rho L}{A}$), hence requires less current to heat. In addition, our method enables sandwiching multiple actuators with thin cross-sectional area in parallel and connect electrically in series to address force and efficiency, respectively.

### 2.5.3 Application: Reconfigurable Suction Gripper

To demonstrate the applicability of the proposed Wave-SMA actuators, we integrated them into a mesoscale origami-inspired reconfigurable suction gripper for reconstructing multiple shapes.

#### Grippers Overview

Gripping is key to object manipulation and assembly. Besides delicacy and accuracy, adaptability of gripper geometry to the contact surface, and its mechanical compliance are important assets that bring high flexibility and dexterity for handling objects of different geometry and stiffness, respectively. Employing multi-DoF robotic fingers [99] requires meticulous control of configuration and contact forces [100, 101], soft jamming grippers [102, 103] have limitations in handling flat or soft objects, and adhesion-based soft gecko grippers [104] necessitate sophisticated clean-room microfiber fabrication using lithography. Conventional soft vacuum suction grippers [105] in the form of cups or bellows, on the other hand, overcome some of these challenges having simple, robust and low cost designs, but lack universality. There are a variety of fixed suction cup geometries from a few millimeters to a few decimeters circular-opening diameter, oval aperture for picking long objects, and with different compliance for lifting solid metal, fragile glass, or flexible textile fabric [106]. Hence, gripping objects of different shape and stiffness with a single cup is impossible without replacement, which is demanding and time consuming. Therefore, a self-reconfigurable suction gripper adaptable to any gripping task would increase flexibility and process efficiency.

#### Origami-Inspired Reconfigurable Suction Gripper Design

To address shape adaptability with grippers, we took inspiration from Origami. Origami-based geometries can produce shape transformations beyond classical 2D to 3D folding. They enable multiple active 3D to 3D shape reconfigurations for adapting to different tasks and environments. However, there is still a substantial gap between the origami shape reconfigurations, functionality and applications apart from proof-of-concept passive structures. We, for the first time, demonstrate a fully functional origami-inspired suction gripper [107] based on foldable mechanisms that reconfigure to multiple 3D shapes to pick objects with different shape and size as in Figure 2.18.

Made from soft and deformable rubber material, a typical industrial suction cup ensures conformity and sealing to the contact interface [108]. However, if we would like to pick objects of different surface areas and stiffness, both the suction gripper geometry, i.e. the cross-sectional area of the mouth, should conform to object contour, as well as the compliance of the gripper. For example, picking a rigid aluminum profile is different to picking a relatively softer hamburger bun in that the latter requires a more delicate grip. This is challenging given the highly deformable nature of elastomers, which creates issues for accurate shape

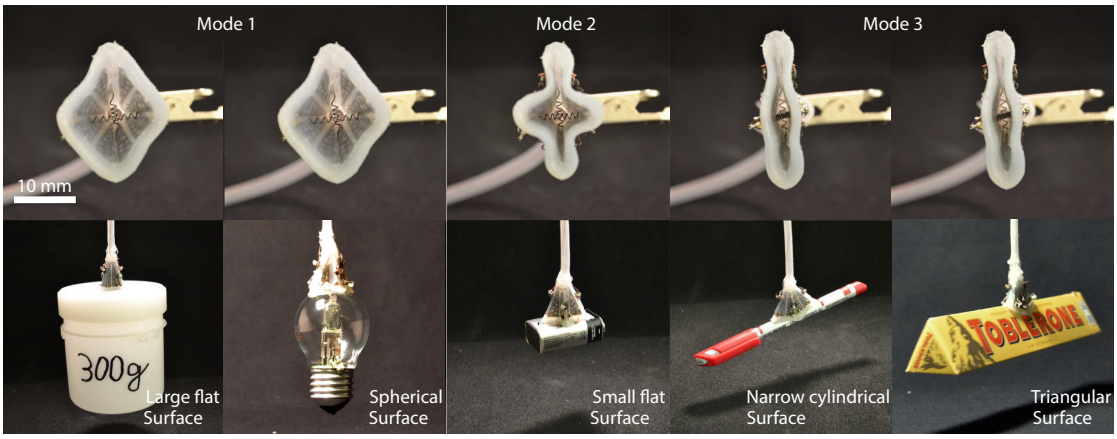


Figure 2.18 – **The reconfigurable universal suction gripper integrating Wave-SMA actuators to produce different shape modes.** The gripper adapts to the object geometry and size, be it a large, small, or narrow planar object, or a cylindrical, or spherical object. In Mode 1, the gripper has the maximum opening area and can pick a container with a relatively large planar surface and a light bulb with spherical surface. In Mode 2, the gripper has a small opening and can grip a 9 V battery, impossible with Mode 1. In Mode 3, the gripper can pick an office pen of 10 mm diameter, as well as a triangular object, like the Swiss chocolate Toblerone.

reconfiguration and control [109]. Our novel robogami suction gripper combines versatility of origami folding design with conformity of soft elastomer material to address shape adaptability for suction grippers, as depicted in Figure 2.18. Fabricated from multi-layer components and powered by SMA actuators and vacuum, our proposed system effectively switches between three operating modes, producing large, small, and narrow openings to pick-and-place objects with flat, narrow cylindrical, triangular, and spherical surfaces. We demonstrate the load bearing capacity of the single suction gripper of more than 5 N, which is 50 times the gripper's weight, and unique ability to pick long objects as narrow as an office pen. We also demonstrate a cable-driven under-actuated approach for the suction gripper to increase power efficiency.

### Gripper Materials Design

The folding mechanism of the suction gripper requires compression or extension of actuators when necessary. Employing linear DC motors at each hinge would make it bulky and rather expensive. Therefore, Wave-SMA actuators along with two helical spring SMA actuators enable easy integration and hinge folding . All actuators compress when their temperature exceeds the phase transition temperature ($M \rightarrow A$), upon Joule heating with direct current. Made of a thin Nitinol ($Ni_{50\%}Ti_{50\%}$) sheet, the low-profile wave SMA actuator facilitates mounting on the suction gripper wall with negligible friction. The activation sequence of the actuators and mode transitions are summarized in Table 1.1.

Besides having high elasticity to restore shape at high angular deflection ($\approx 180°$), the hinge material should possess sealing properties to avoid air leakage. Silicone rubber is well-suited

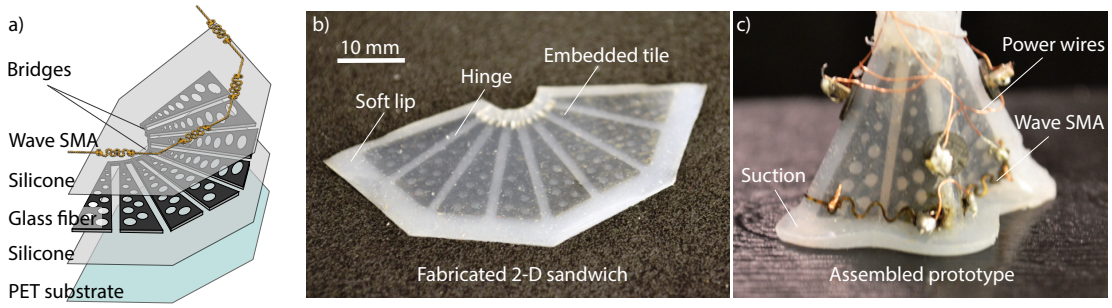


Figure 2.19 – **The rapid 2-D layer-by-layer fabrication process of the suction gripper and the fabricated prototypes in 2-D and 3-D. a** The rigid fiberglass tiles are embedded between two silicone rubber layers to enable flexure hinges, conformity and sealing at the gripper opening. The wave SMA actuators are mounted lastly onto the sandwich. **b** The fabricated 2-D prototype without wave SMA actuator layer, which was folded and assembled to 3-D **c**

for this purpose, which comes with fabrication simplicity by molding. Among the several types of commercially available silicone elastomers, we selected the most suitable DragonSkin ® 10 (Smooth-On Inc.) for high elasticity (475 psi), resistance to tearing (102 pli) and operational temperature (-53 °C to +232 °C). There is a myriad of possible materials for rigid tiles and we chose fiberglass due its high strength and low weight.

### Gripper Fabrication

We fabricated our prototype employing 2-D processing method of discrete material layers, piling to multi-layer sandwich and assembly to 3-D. The suction gripper construction necessitates both rigid backing and compliance for controlling shapes and conformity to the object. We embedded the triangular tiles into a silicone rubber (DragonSkin®, Smooth-On Inc.) in a multi-layer process, as depicted in Figure 2.19a, and the sandwich in Figure 2.19b is folded into a pyramid given in Figure 2.19c. The gripper is constructed from three layers; the outer two silicone layers embed the fiberglass tile layer. The silicone layers here not only serve as the flexure hinges, but also provide soft contact and sealing with the surface by means of lips. The lips protrude 5 mm from the rigid part, ensuring both foldability, compliance and sealing at the gripper opening.

To obtain the first layer, the liquid elastomer was poured onto a profiled PET sheet (positive mold) and spin-coated to 0.5 mm thickness and cured for 10 minutes in the oven at 90 °C. The tiles are cut from 0.4 mm thick fiberglass sheet employing a laser micromachining station (LAB 3550, Inno6 Inc.) with bridge spacers to ensure equal hinge spacing of 1.6 mm between the triangular tiles. The fiberglass layer is then placed onto the elastomer layer and another layer of liquid elastomer is poured onto the fiberglass. The sandwich is spin-coated and cured in the oven for one hour at 90 °C. The holes on the fiberglass layer enable bonding of top and bottom elastomer layers by holding the tiles in place and preventing delamination. Finally, the PET support is removed, the wave SMA actuators are mounted and the bridge spacers on

fiberglass cut out. The 1.5 mm thick sandwich is folded edge-to-edge to form a closed surface, and the two connecting ends are attached using silicone glue (Sil-Poxy ®, Smooth-On Inc.). A 3 mm diameter flexible pipe is attached to the small opening of the pyramid using silicone glue, which then connects to the vacuum source.

### Flat and Helical Spring SMA actuators Fabrication

SMA actuators require shaping and heat treatment process to induce the desired shape. In our design, all actuators were programmed to a compressed state. The set of four wave SMA actuators $SMA_1$ with compressible wave-like pattern were cut out of a single 0.1 mm thick Nitinol sheet (Memry Corporation), as shown in Figure 2.19a. The 1 mm diameter holes at each section allows mounting the actuator onto the gripper's four walls (see Figure 2.19) and the bridge connections are removed after mounting. To program the initial compressed shape, the series of actuators is annealed in a high temperature furnace (Nabertherm GmbH) at 400 °C for 30 minutes. After, the actuators are mounted on the suction gripper, fastened using wires and the connecting bridges are cut-out. Three wires connect the actuators in series and two power wires are finally attached to the actuator terminals to provide power.

### Hinge and Actuators Characterization

Force and deflection capabilities of SMA material and silicone hinges are highly influenced by their geometry, as well as the fabrication process. Therefore, predicting their behavior without characterization is difficult or even impossible. To verify the capability of the SMA actuators in overcoming the hinge stiffness in austenite state (hot), we designed a loading setup depicted in Figure 2.20a. The setup consists of a fixed-end part and a moving part, which comprise a linear stage with mounted load cell (Nano 17, ATI Industrial Automation). The setup is employed to characterize the wave and spring SMA actuators blocked forces by extending them in both austenite and martensite phases, whereas the valley and mountain hinge stiffnesses are characterized by bending them under compression.

In the first test, we attached the wave SMA actuator ($SMA_1$) with powering wires between the fixed and moving ends on the setup, as in Figure 2.20a. Initially, the actuator was in compressed state with length of 6 mm, then the stage is moved by 1 mm increments and the actuator force is measured by activating it at each position for 20 seconds to reach a steady-state force. The procedure is repeated three times per position and plotted with error bars in Figure 2.21. The same test is performed for martensite case, from 6 mm to 9 mm elongation, with 1 mm deflection increment at room temperature. The produced force (see Figure 2.21) was much lower than that of the austenite case as expected. The valley hinge (yellow) bending test is performed on the same setup by removing the tips on both ends and attaching a flat plate on the fixed-end as in Figure 2.20b. For this test, only a segment with two right triangle tiles connected with a rubber hinge is placed between the plate and the load cell surface. The hinge is pre-bent initially to overcome instability point and loaded by 1

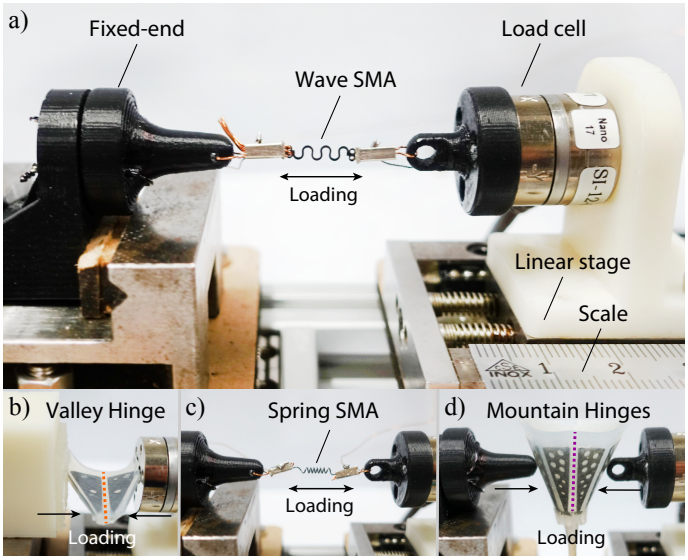


Figure 2.20 – **The blocked force measurement setup for SMA actuators and rubber hinges. a** The wave SMA actuator is clamped to the fixed part at one end and to the moving part with a load cell at the other end. The linear stage is moved to multiple positions and the actuator forces are measured for both austenite and martensite phases. **b** The valley hinge force characterization by bending. **c** The spring SMA mounted to the setup is tested similarly as the wave SMA. **d** The mountain hinge force measurement by compressing with two point tips from both sides.

mm increments and the forces at each position are recorded and plotted in Figure 2.21. The hinge stiffness is lower than that of the actuator's in both austenite and martensite phases at high deflections, however it is higher at around 6 to 6.5 mm deflection at room temperature, highlighted by the shaded triangular region. This enables partial shape recovery of the suction gripper passively by extending the wave SMA actuators.

In the second test, the spring SMA actuator ($SMA_2$) force is compared with the recovery forces of the mountain hinges (magenta). The loading procedure is the same as for the wave SMA for austenite and martensite phases (see Figure 2.20c). Due to higher stroke, the actuator was extended from 7 mm to 19 mm with 4 mm increments. Figure 2.22 displays the austenite forces were considerably higher than the martensite forces. To measure the stiffness of the diagonal mountain hinges, the suction gripper is placed between the fixed-end and moving parts with point tips pressed to two diagonal edges, as in Figure 2.20. The gripper is fixed at the bottom to ensure vertical alignment and loaded with increments of 2 mm from 16.5 mm opening distance to 9.5 mm. The hinge stiffness was lower than the spring SMA at room temperature at high deflections, however, it was higher below 13 mm and could partially recover its shape in the cooling process of the actuator.

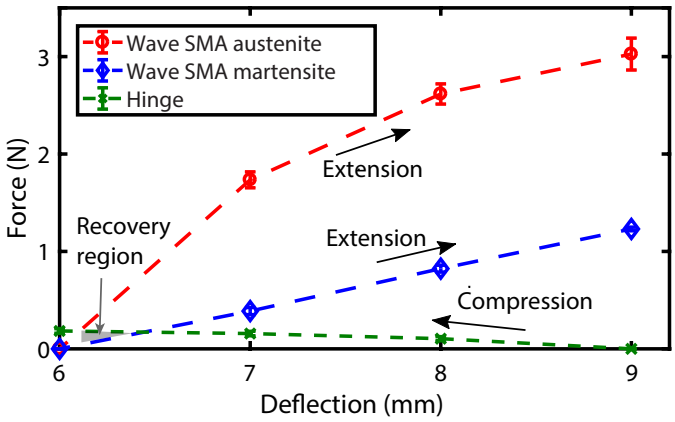


Figure 2.21 – **The wave SMA actuator force plots in austenite and martensite states, and the valley hinge force response at different linear deflection.** The triangular region reveals hinge folding when the actuator is in heating state (austenite) and the hinge partial recovery when the actuator is in cooling phase (martensite).

### Results

To validate the reconfigurability of the suction gripper and its gripping performance, we conducted two experiments to study its shape reconfiguration to pick different objects and the holding force in all three modes.

The experimental setup is as follows: the suction gripper is connected to a -80 kPa vacuum source and the actuators are connected to a controller board. The controller board comprises an Arduino microcontroller, three switches to regulate the power supply to three SMA actuators by PWM duty modulation and three push buttons to activate the actuators manually. PWM duty value of each actuator is calibrated to generate desired austenite finish temperatures of 70 °C for spring SMA and 65 °C for wave SMA, as specified in the vendors' datasheets for wire and sheet Nitinol alloys, respectively.

To test the effectiveness of the modes for gripping objects of different size, we selected five items to pick-and-place: a plastic container with large flat planar surface area, a 9 V DC battery with 25×44 $mm^2$ planar surface area, an office pen with a diameter of 9.5 mm, Swiss chocolate Toblerone with triangular profile, and a spherical light bulb, as depicted in Figure 2.18. The gripper is at rest in Mode 1 and could easily pick the large plastic container and the light bulb due to deep geometry. Then it was activated for 5 seconds to configure to Mode 2 to pick the battery that is too small to pick with Mode 1. Finally, the gripper was cooled for 20 seconds and activated for 5 seconds to configure to Mode 3 and pick the pen and chocolate, both successfully performed.

In this test, the gripper achieved the desired shapes accurately; however, the shape of the gripper was not maintained after contact with an object. The gripper shrunk to compensate for vacuum pressure, therefore the opening area decreased resulting in lower forces. This

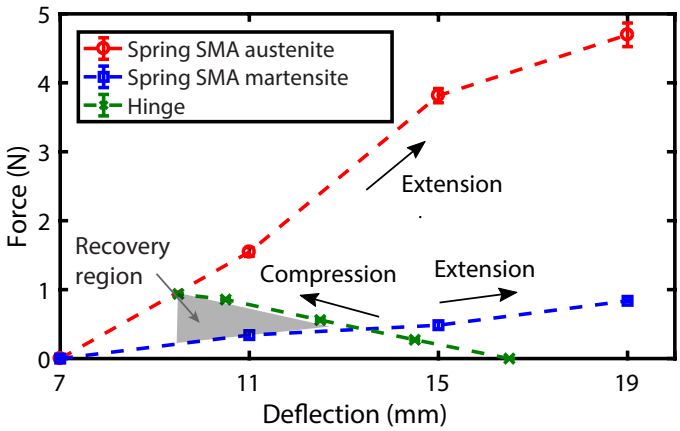


Figure 2.22 – **The helical spring SMA actuator force response in austenite and martensite states, and the mountain hinge force at different deflections.** The shaded triangular region shows the capability of the actuator to fold the hinge in heating phase (austenite) and the hinge's partial recovery when the actuator is in cooling process (martensite).

phenomena was observed in all three modes and is due to structural softness of the gripper. Also, in Mode 2, a slight push of the gripper perpendicularly to the battery surface was needed to ensure suction. This discrepancy is related to imperfection in the opening surface.

To evaluate the maximum holding force in each mode, we loaded the suction gripper, as in Figure 2.23a. Figure 2.23b displays the measured and calculated holding forces. As the suction gripper shrinks radially under vacuum, we measured the actual opening areas to calculate the expected forces. To study the gripper opening area, suction is applied onto a flat transparent plastic for modes 1 and 2, whereas for Mode 3, a 180° bent transparent plastic with curvature of 9.5 mm is used. The vacuum pressure generated by the gripper was identical in all three modes at -80 kPa and was measured using a digital pressure switch (ISE30A-01-P, SMC Corporation). The areas of the openings are then measured using image processing software (Image J) and used to calculate the holding forces by expression in (1).

The actual forces are measured by loading the suction gripper with weights in three modes, as in Figure 2.23a. Suction is first applied to a round flat plate of 43 mm radius for Mode 1, 29 mm radius for Mode 2 and a bent plate for Mode 3, with hooks for attaching weights. As expected, Mode 1 could hold the maximum load of 5.2 N (530 g), which is more than 50 times its weight, whereas Mode 2 could hold up to 4.2 N and Mode 3 up to 3.9 N. The loads are attached vertically and centered with minimal tangential effect and the weights are increased until the gripper eventually detaches from the plates. The maximum holding forces are plotted in Figure 2.23b, the error in predicting the expected forces was small for Mode 1 and 2 and comparably large in Mode 3 due to imperfect sealing between the curved surface and the suction gripper.

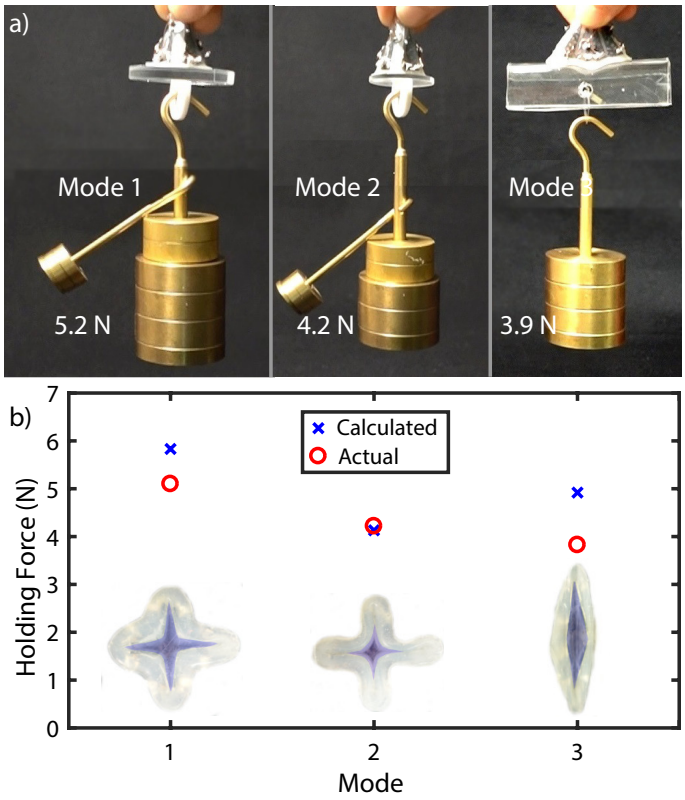


Figure 2.23 – **The origami suction gripper holding force measurement test and plots. a**, for Mode 1, the gripper is attached to a flat round plate (d = 43 mm) with a hole to hook weights. The gripper can lift up to 5.2 N weight. Similarly, a smaller plate (d = 29 mm) is used for lifting weights up to 4.2 N with Mode 2. Finally, a bend acrylic plate with 9.5 mm curvature is employed for hooking weights up to 3.9 N in Mode 3. **b**, the comparison between the actual and calculated holding forces in each mode. The expected forces are calculated by measuring the actual gripper opening area, shaded with blue, on a transparent surface at -80 kPa vacuum pressure. The actual value is slightly lower than the analytic one for Mode 1 and comparably lower for Mode 3 due to imperfect sealing.

## 2.6 Design Methodology for SMA Actuators

Based on the studies of three different actuators, such as the helical spring, bending sheet and wave spring actuators, we summarize by proposing a systematic design process for SMA actuators. Our goal is to set a clear and repeatable design methodology to facilitate their design process and encourage accessibility in the field.

Figure 2.24 depicts the generalized design process of SMA actuators. As mentioned earlier, SMA *geometry*, *mechanism* and *material* are critical in defining their behavior and are closely related. Therefore, they are placed concurrently in the beginning of the design process. The development process requires designing actuator geometry, including programmable shape and dimensions and its mechanism of motion in terms of force and deflection. It also

necessitates determining mechanical and thermal characteristics by characterizing a material specimen. These three features set first to construct a physical and behavioral preliminary model of an SMA actuator, then fabricating them and characterizing for both mechanical and material properties. As predicting the SMA behavior is difficult it necessitates multiple iteration steps to achieve desired results.

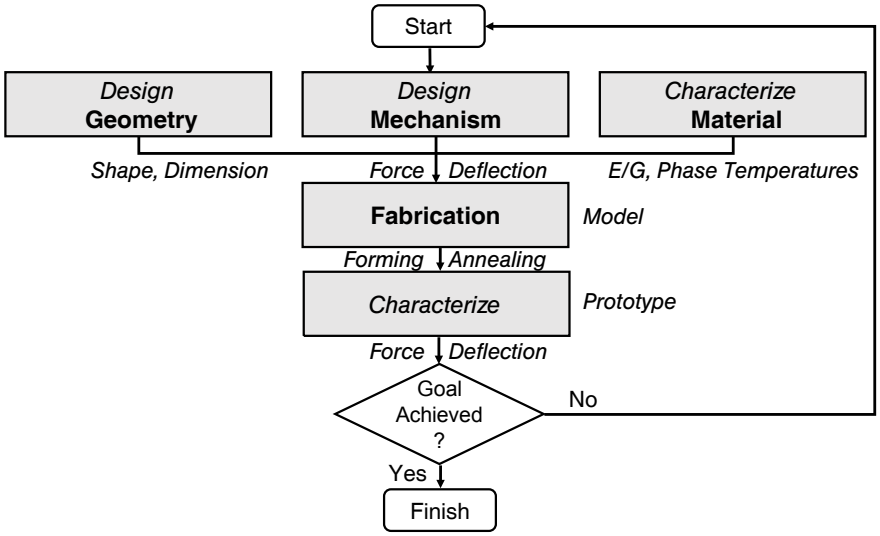


Figure 2.24 – **The systematic design methodology for SMA actuators.** The design process begins with designing initial geometry in terms of shape and dimensions, mechanisms, like force and deflection, and determining the material properties, such as modulus of elasticity or shear modulus in concurrent fashion. After defining the preliminary model, the design requires fabrication and characterization of the actuators. The process is interated until a desired performance is achieved.

## 2.7 Fluid-Driven Mesoscale Actuation Design

Thermally-activated functional material-based actuators overcome key challenges of conventional electro-mechanical actuators by being highly customizable and compact for embedment by multi-layer lamination processes, however, they are still substantially slow (<1 Hz), inefficient and irreversible without using an antagonistic pair, which further inhibits actuation. Some research have shown high speed and repeated folding of origami hinges by employing discrete inflatable pouch [65] and elastomeric [110, 111] actuators. However, the high volumetric expansion of the actuators (>200 %) limits their distribution density and motion range for more complex multi-hinged patterns, like the Miura-ori tesselation in Fig. 2.25, which has several mountain and valley hinges connected at a single vertex. Moreover, such air-pockets require a pre-fabrication process, such as heat sealing or molding, before integrating into a robotic origami. They were implemented in limited numbers for moving pre-folded shape changing origami structures [112] with individual fluidic piping. Similarly, a vacuum-driven actuator has been proposed [113] for collapsing readily-folded origami struc-

tures by encapsulating them in an airtight film, which lacks 2-D to 3-D self-folding capability and control over the folding sequence.

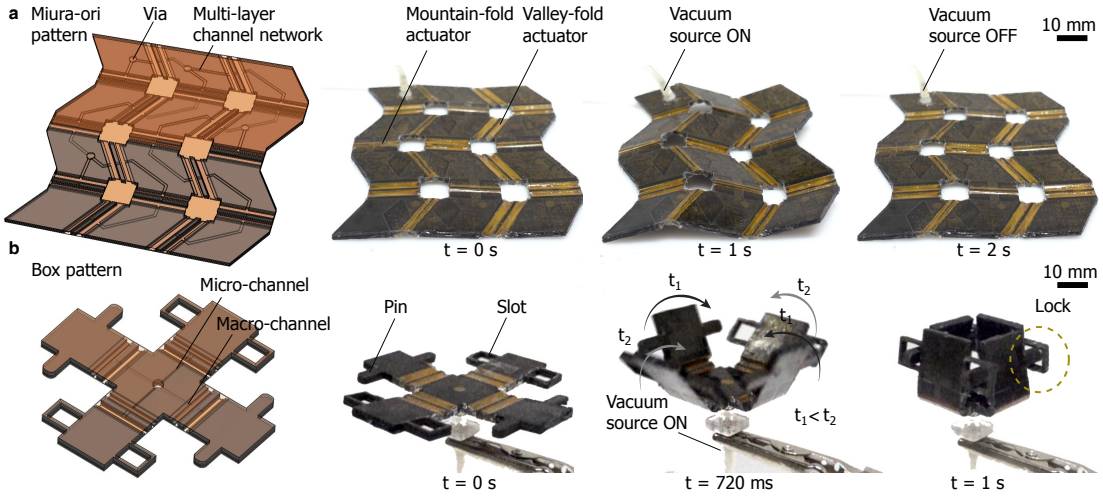


Figure 2.25 – **Two examples of reconfigurable self-folding origami structures driven by the proposed fluidic actuator-channel networks.** **a** The Miura-ori pattern embeds two rigid channel layers to distribute pressure among the mountain and valley folding actuators. The direction of folding is decided by the gap size on the top and bottom rigid cover layers. **b** The box pattern with four walls folding in a programmed sequence. Two walls embed a micro-channel with cross-sectional dimensions of 0.125 mm × 0.5 mm and the other pair has a macro-channel with dimensions 0.5 mm × 1 mm. The difference in the channel size results in a folding time delay occurring at high speeds (≤200 ms). We introduced pin and slot connectors on the walls to ensure locking only in the right folding sequence; first pin then slot, and to display the delay visually.

In this section, we present a method for designing single source, progammable, fluidic actuator and channel-embedded networks for origami sequential self-folding [114]. The proposed low-profile and at scale vacuum-powered multi-layer networks enable designs of complex multi-hinged origami patterns with fast (>1 Hz) folding and reversible shape reconfiguration. Owing to tunable design combined with layer-by-layer rapid manufacturing process, our approach allows for selective embedment of actuators and channels for folding complex origami patterns with mountain and valley folds in one step, like the Miura-ori tesselation in Figure 2.25a, or in a sequence, like the box pattern with tunable channels in Figure 2.25b. The main contributions of our work are

### 2.7.1 Fluidic Actuator Unit Design

#### Force and Motion Generation

The fluidic actuator and channel-embedded unit consists of a T-shaped void or chamber between two rigid tiles and airtight deformable membranes covering its four sides: top, bottom and two side walls, as in Figure 2.26a. A channel with rectangular cross-section residing close

to the bottom enables air flow between the pneumatic source and the actuator chamber. The hinge bending occurs upon applied vacuum pressure , due to the surface area difference between the top and bottom membranes, with latter possessing a smaller surface area. The force produced by the difference between the high atmospheric pressure outside and low pressure inside the chamber deforms the top membrane inward and pulls the side and bottom rigid walls, generating a bending moment at the middle of bottom membrane (yellow dot).

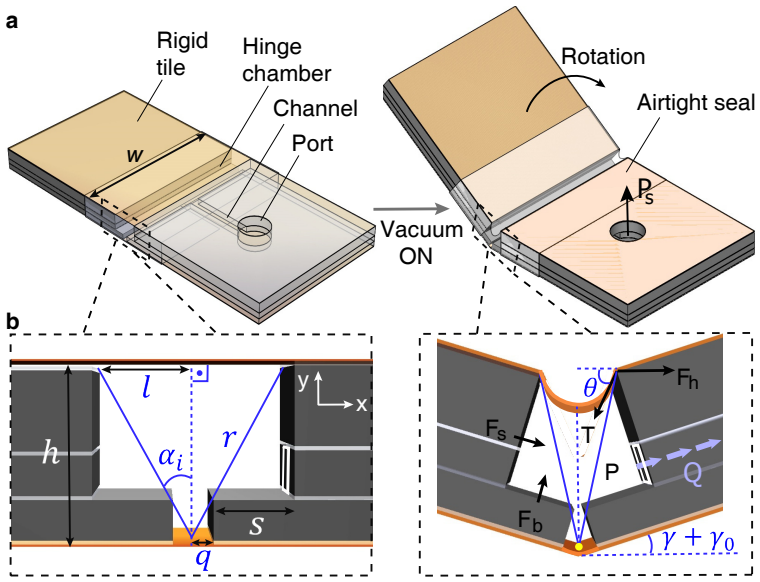


Figure 2.26 – **The fluid-driven actuator working principle. a**, the actuator comprise an air-sealed chamber, closed with flexible membranes. The difference in rigid support gaps at the top and bottom membranes define fold direction. The actuator folds upon vacuum pressure applied at the port connected to the chamber via a channel. **b**, the forces produced by the negative pressure acting on the membrane and rigid walls generate a bending moment at the yellow pivot. [114]

To establish a clear relation between the actuator geometry, membrane stiffness and fluid dynamics and it output moment and bending angle, we studied the physical model, given in Figure 2.26b. The deformation of the membrane is approximated by a planar cable deforming under distributed load [115], whereas the bottom membrane experiences pure bending. We neglected the effect of the side membranes due to complexity of predicting their deformation. The deflection of the top membrane under applied pressure can be expressed by

$$y = \frac{1}{F_h} \iint \Delta P w dx^2 = \frac{\Delta P w x^2}{2F_h} \tag{2.9}$$

here, the distributed load $\Delta P = P - P_{atm}$ acts on the top membrane surface spanning $x$-$z$ Cartesian plane with width $w$ and generates horizontal force $F_h$. Now, by taking the derivative

of the expression 2.9 in $x$, we can compute the slope of the curve as

$$\frac{dy}{dx} = \tan\theta = \frac{\Delta P w x}{F_h} \tag{2.10}$$

We also know that the length of the curved membrane is $l = \frac{1}{2}\int_{-l}^{+l}\sqrt{1+(\frac{dy}{dx})^2}dx$, so we can find the horizontal force $F_h$, which relates to the tension force by $T = \frac{F_h}{\cos\theta}$. The applied pressure similarly produces forces at the side and bottom rigid walls $F_s$ and $F_b$, respectively, that are the product of the pressure and their surface areas

$$F_s + F_b = \Delta P w(h+s) \tag{2.11}$$

where $h$ is the thickness of the actuator and $s$ is the width of the protruding rigid layer at the bottom. We can now calculate the moment produced by the applied pressure at the bottom pivot (yellow dot) as follows

$$M_p = rT\cos\big(\alpha_i - \gamma - \gamma_0 + \theta\big) + \frac{hF_s}{k} + \frac{F_b}{\frac{s}{2}+q} \tag{2.12}$$

here, $\alpha_i = \arctan\frac{l}{h}$ is the actuator initial angle before actuation, $\gamma$ and $\gamma_0$ are the half bending and recovery angles of the bottom membrane, $\theta$ is the top membrane bending angle, $q$ and $l$ are the half lengths of the bottom and top hinges, respectively. $F_s$ generated by the side wall is separated into two components that contribute to the bending of both membranes and their proportion is a function of the membrane stiffness $1/k$. Although, we neglect the membrane weight and assume the moment is generated solely by pressure, the membrane stiffness that counters the moment is crucial in defining the actuator output moment, which is described next.

#### Hinge Membrane Stiffness Model

The stiffness of the membrane is critical for force generation and hinge restoration. We assume that the proposed actuator hinge comprising two membranes deforms elastically and undergoes pure bending. For a bending sheet, the moment is given by $M = EI\phi = E\frac{Width\times(Thickness)^3}{12\times Length}\phi$, where $E$ is the elastic modulus of the material, $I$ is the second moment of inertia and $\phi$ is the bending angle.

In order to sum the effect of both membranes, the bending moments of the bottom and top

membranes are calculated about the bottom membrane's center. The total bending moment resisting to actuation can be calculated by

$$M_k = E\frac{w(t)^3}{12}\left[\frac{\gamma+\gamma_0}{q} + \frac{\theta}{l^2} r sin(\alpha_i - \gamma - \gamma_0 + \theta)\right] \tag{5}$$

The actuator total moment can now be calculated as $M_t = M_p - M_k$. Increasing the cross-sectional area of the actuator increases force and placing multiple chambers in series increases its angular range, as in Figure 2.25b.

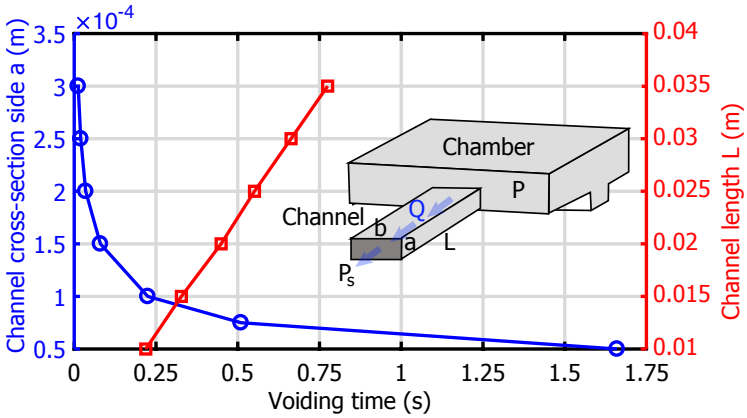


Figure 2.27 – **The relationship between the air voiding time and channel geometry for a chamber with fixed volume.** Air flow rate drops (blue) significantly for a smaller channel size, where it reduces linearly (red) with channel elongation. This highlights the ability of varying the fluidic resistance to design a variable time delay networks.

### Quasi-Static Fluid Model for Folding Sequence Programming

To achieve flexibility in realizing various self-folding origami structures, it requires not only a proper arrangement of crease patterns but also control over their folding sequence. We propose a single pressure source underactuation method for folding sequence control of distributed actuators by tuning the resistance of fluidic channels, therefore, programming the folding sequence logic circuitry into the active multi-creased origami structures.

For a rectangular fluidic channel carrying a laminar flow, the volumetric flow rate is given by

$$Q(t) = (P(t) - P_s)\frac{\rho(t)}{\mu}\underbrace{\frac{a^3 b}{12L}[1 - 0.630\frac{a}{b}]}_{R_{ch}^{-1}} \tag{2.13}$$

where $Q$ is the volumetric flow rate, $P(t)$ and $P_s$ are the hinge chamber and source pressures,

$\rho$ and $\mu$ are the air density and viscosity, respectively, and $R_{ch}$ is the channel resistance, which relies on the channel cross-sectional dimensions $a$ and $b$, and its length $L$. Clearly, a channel with larger cross-sectional area permits higher flow rates and the variation is more significant for channel cross-sectional dimensions than for channel length. Now, if we assume a locally steady flow that obeys the ideal gas law, the air density inside the chamber evolves as follows

$$\rho(t+\Delta t) = \rho(t)[1 - \frac{Q(t)}{V_T}\Delta t] \tag{2.14}$$

where $V_T$ is the total air volume inside the hinge chamber and channel combined before actuation, and $\Delta t$ is the time step. Then the pressure changes with density as $P(t) = RT\rho(t)$, where $R$ is the air specific gas constant and $T$ is the temperature. The complete voiding of the hinge chamber occurs with $Q(t_f) = 0$ at time $t_f$.

We simulated the relations in 2.13 and 2.14 in Matlab and compared the voiding time for different channel cross-sectional dimensions and length in Figure 2.27. We assumed a fixed volume chamber and run the simulation until the flow of air particles diminishes. The flow drops significantly with a slight decrease of the cross-sectional side $a$, whereas it is linearly proportional to the channel length.

### 2.7.2 Multi-Layer Fluidic Networks Design

The fluidic folding actuator unit enables integration into large networks to achieve complex origami shapes by multi-layer design process. To demonstrate the versatility of our design method, we pick a well-known, yet challenging pattern Miura-ori, illustrated in Figure 2.28, which possesses both mountain and valley folds connected in closed chains. We designed a pattern with 17 fluidic folding actuator units (9 valley and 8 mountain) connected in a large network via channels. This requires six functional layers to achieve self-folding: a pair of rigid cover, two rigid channel and two flexible membrane layers. The gap size on the cover layers decides mountain or valley folds: the actuator produces a valley fold if the top cover gap is larger than the bottom one and a mountain fold if vice versa. To employ a single source and distribute the pressure among the actuators it requires two channel layers; one for the mountain folds and another for the valley folds. Like with electrical circuits, the connection between the channel layers can be maintained by vias. The top and bottom flexible membranes make the hinges, ensuring sealing, structural integrity of the rigid parts and shape recovery. We employ channels with large cross-sectional areas (macro-channels), however, one can also design multi-layer channel networks with variable channel size to achieve sequential folding, like in the folding box example in Figure 2.25b.

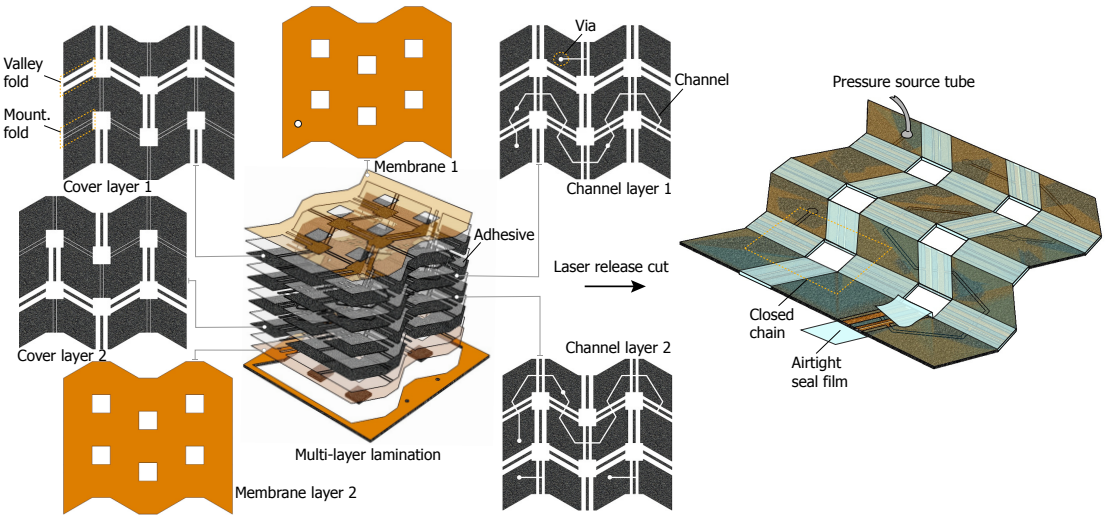


Figure 2.28 – **The layer-by-layer fabrication and assembly process of the fluidic actuator-channel networks for origami self-folding.** Here, we illustrate the fabrication process of a well-known Miura-ori crease pattern as an example. The 2-D structure consists of 11 layers of rigid, flexible and adhesive layers. As the structure requires folding in mountain and valley, we designed two channel layers interconnected by vias to maintain air flow between the layers. First, the discrete layers are laser cut separately in rectangular forms with grooves for actuator chambers and channels. Then the layers are stacked and aligned by cylindrical pins on a metallic plate and heat pressed. The sandwich is then laser cut again to a desired outline to release hinges from the supports. Finally, we air-seal the hinges with laser cut hot melt films by wrapping around the chambers and heat pressing.

### Fluidic Networks Fabrication

The proposed fluidic networks comprise channels with various cross-sectional dimensions varying from few hundred micrometers to few millimeters. Employing 3-D printers is not a viable option as their resolution is limited and it is difficult to achieve complex multi-layer fluidic networks without employing a support material. Therefore, we employed a layer-by-layer lamination process depicted in Figure 2.28 to readily embed actuators and channels into multi-tile origami structures with high flexibility.

Figure 2.28 shows the fabrication steps of the Miuri-ori pattern. The quasi-2-D structure comprises six functional and five adhesive layers. We employ 500 $\mu$m thick FR4 fiberglass sheet for rigid tiles due to lightweight and high stiffness characteristics, whereas the membranes are made of a 25 $\mu$m thick polyimide film (Kapton, DuPont Inc.) due to durability. Poli-melt 701 hotmelt adhesive (Poli-Tape Group) is employed for bonding the layers together, as well as for air-sealing the actuator chambers by wrapping around. The fabrication process is as follows: first, the individual layers are cut employing a laser micro-machining station (Speedy400, Trotec Laser GmbH) in rectangular forms with necessary grooves for actuation and channels then they are stacked on a metal plate by aligning with pins. The multi-layer stack is then heat pressed at 110 °C for eight minutes to ensure layer bonding. The sandwich then is laser cut

again to release hinges from the surrounding support material. As the final structure lacks side membranes, we wrapped the laser cut hotmelt adhesive strips around the hinges and heat pressed again at 110 °C for three minutes. This enables the hinge side walls sealing, however, we applied an additional thin layer of silicone glue (Sil-Poxy ™, Smooth On Inc.) on the seal conjunctions and fiberglass edges to ensure full air impermeability.

### 2.7.3 Results

To assess and validate the models presented in Section II across several samples with different geometry, we measured blocked forces for each when actuated at different angles using the setup depicted in Figure 2.29a. The setup comprises a force sensor (Nano 17, ATI Instruments), the actuator sample fixed at one end and in contact with the sensor at the other end, a camera mounted above the sample to extract the actuator angles using image processing software (Image J) and a vacuum pressure source with a pressure indicator sensor (SMC Corp.) connected to the actuator via a 3-mm diameter pipe. In our experiments, vacuum is achieved by converting a positive pressure using a vacuum ejector (ZH10BS-06-06, SMC Corp.). We fabricated three actuator-channel units with the sizes given in Table 2.3. While the channel length and cross-sectional area was identical for all samples, we varied the hinge chamber size ($l$, $w$ and $h$) to test different actuator sizes: sample 1 thin-wide, sample 2 thick-narrow and sample 3 thick-wide.

#### Blocked Force Test

To determine actuator sample forces at different applied pressures and compare them with the calculated ones using the model, we performed a blocked force test as in Figure 2.29a. Each sample is mounted onto the force setup and tested in blocked condition at different folding angles. Figure 2.29 displays the experimental results versus the model for -60 kPa and -80 kPa vacuum pressure. The model includes the top and bottom membrane stiffness given in (5) verified by loading the actuators with the force sensor in the direction of rotation. It is clear that the actual behavior is similar to the expected for all samples, with the model slightly greater than the measured data, which we suspect is due to the omitted stiffness of the side membranes. Moreover, there is a considerable discrepancy at lower angles for the largest sample 3 in Figure 2.29d, which is due to the side wall force $F_s$ at small folding angles that collapses the bottom membrane, resulting in large stiffness ratio between the top and bottom membranes ($k \gg 1$). In addition, some air leakage could still be persevering that could cause pressure drops inside the hinge chamber.

#### Robotic Shape Morphing

To verify the applicability of our method to more complex origami patterns, we fabricated and tested the Miura-ori tessellation depicted in Figure 2.25. The pattern comprises a matrix of 2

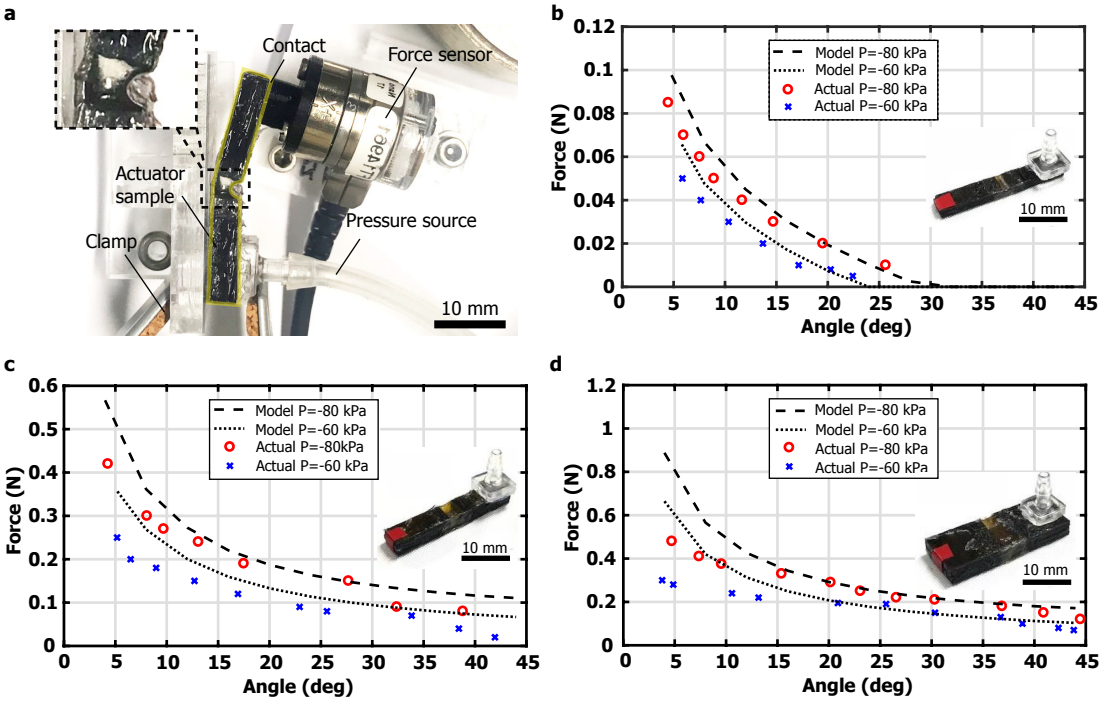


Figure 2.29 – **Blocked force characterization of fluidic actuator samples. a**, the force setup employed to measure blocked force at different angles. It comprises a force sensor, a camera for measuring angles and the actuator sample with fixed one end. The force is measured by stationing the sensor in contact with the actuator moving arm at different angles and pressurizing the actuator. **b**, the force plot for sample 1 with the chamber size of 2×2.2×7 $mm^3$. **c**, the force plot for sample 2 with the chamber size of 4×4.5×7 $mm^3$. **d**,the force plot for sample 3 with the chamber size of 4×4.5×15 $mm^3$.

× 2 base units with four hinges connected in closed chain: three for mountain and one for valley fold, or vice versa. The angular orientations of the hinges make up the wrinkles that fold out of plane.

We applied a negative pressure of -80 kPa to a single source port to achieve shape reconfiguration. When activated, the pressure distributes inside the actuator-channel network. Owing to reduced actuator volume, the sheet self-folding occurs in less than a second. It can also restore its flat shape at similar rates when the pressure is removed.

### Box Sequential Self-Folding

To demonstrate the self-folding capability with variable folding sequence, we fabricated and tested a self-folding box prototype given in Figure 2.25. The pattern consists of four square tiles branching out of a central tile that houses a pressure source port. We designed two hinge chambers per actuator to fold the walls to 90 °. Two opposite walls connect to the pressure source via a 10 mm long macro-channel with cross-sectional dimensions of a = 0.5 mm and

Table 2.3 – The actuator samples with different geometric parameters tested on the force measurement setup.

| **Samples** | l (mm) | h (mm) | w (mm) |
|---|---|---|---|
| Sample 1 | 2 | 2.2 | 7 |
| Sample 2 | 4 | 4.5 | 7 |
| Sample 3 | 4 | 4.5 | 15 |

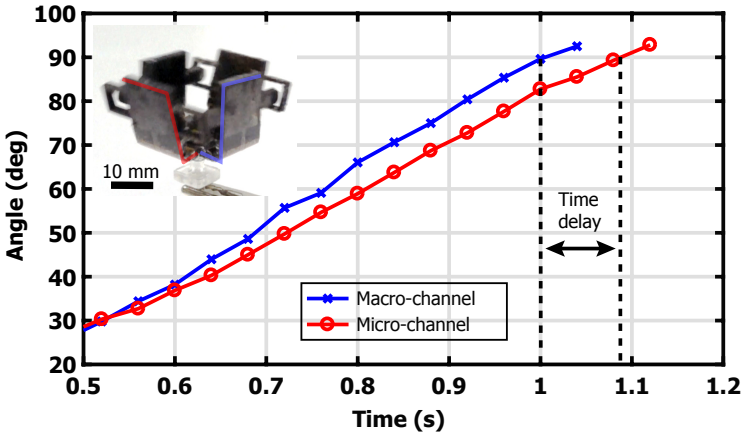


Figure 2.30 – **The sequential folding of a box with macro and micro channels**. The plots show the folding time difference between the walls with macro- and micro-channels. The difference in folding time is reflected on the slopes of the curves: the wall the with macro-channel has a steeper slope and folds first, whereas the wall with the micro-channel is slower by around 100 ms. As there was no apparent time difference for both channels before 500 ms, the plot was truncated to highlight the time delay.

b = 1 mm, whereas the other pair embeds a micro-channel with the same length and cross-sectional size a = 0.125 mm and b = 0.5 mm. To highlight the folding time difference between the channels visually, we introduced pin and slot connectors on the walls with macro- and micro-channels, respectively. The box locks only if the pin connector folds first and then the slot to ensure their engagement.

We measured the folding time for both walls with macro- and micro-channels using a high-speed camera (RX100 IV, Sony Corp.) at 1000 frames per second frame rate and plotted in Figure 2.30. It shows that the walls reach 90 ° at different rates with the pins folding first and the slots delayed for around 100 ms. The plot is truncated below 500 ms as there was no time delay between the walls in the beginning.

## 2.8 Conclusion

In this chapter, we present four novel actuation methods for mesoscale robots: three SMA-based actuation approaches for continuous rotational, linear and high speed discrete motions and a fluid-driven rotational motion. Each actuator design targets multifunctionality, miniaturization, easy assembly for mass-production and minimality. We design, model and experimentally validate them and demonstrate a variety of applications. We address the limitations of SMA actuators bandwidth by designing a helical spring SMA-based, compliant snapping mechanism that produces high power and high speed actuation. We demonstrate high torque bending with low power consumption employing sheet SMA-microheater composite design. We address the fabrication challenges of SMA actuators by designing a novel flat spring type actuator that allows for minimal processing and assembly steps. Finally, we demonstrate high speed, single source, distributed actuation employing fluids, addressing the bidirectional actuator embedment in multi-layer lamination process.

# 3 Design Methodology for Constructing Mesoscale Composite Robots

From the commercial kick-off of industrial robots in early 70s to today, their design has significantly improved thanks to advancements in design methodologies and manufacturing technologies. While robotics design knowledge was of interest solely in industry and research communities, today it is accessible to almost everyone thanks to off-the-shelf components and desktop 3D printers that transcended robot prototyping beyond factories. This is further backed by robotics lectures, workshops, handbooks [35], challenges and competitions, and rapidly growing makers communities. Structuring the knowledge of robotics design the years fueled the development of repeatable and comprehensive robotic design methodologies and standardization, reachable by interdisciplinary research community.

Accessibility and customizability of multifunctional, mass-producible mesoscale robots is the real potential for remote applications, education and human-robot interaction. However, to this end, the research in the field focused on the development of specific functional components, without exploring a general design methodology. The mechanical design of conventional robots are now well studied and governed by models of rigid bodies: mechanisms, kinematics and dynamics, 3-D geometric structures, off-the-shelf motors and sensors, predefined materials, and well-established manufacturing processes. The same methodologies are not directly applicable to mesoscale multimaterial robots as they are highly integrated and there is no apparent division between *mechanisms, geometry, functional components, materials* and *fabrication*. We demonstrated that functional materials, like SMA actuators, can produce a variety of active mechanisms by tailoring geometric and material properties in the previous chapter and we proposed a systematic method on how to design multifunctional SMA actuators. While this is applicable to a single isotropic material, then the next challenging question is *How to design multifunctional multimaterial composite robots? What, if any, is the generalized design methodology?*. Our research objective in this chapter is to investigate

The material presented in this chapter is adopted from the following publications:

**Zhakypov, Z.**, and Paik, J., Design methodology for constructing multimaterial origami robots and machines. IEEE Transactions on Robotics, 34(1), pp.151-165, 2018.

multimaterial components and their composition into functional structures and mechanisms along with consolidating design techniques by creating a systematic and repeatable design methodology. Establishing a clear process will improve mesoscale robot design practice, contributes to the robotics research community by bringing attention to the potential and challenges in the field and attracting researchers from diverse areas, such as material science, manufacturing and biologists.

In this chapter, we present a comprehensive formulation of a mechanical design process of origami-inspired multimaterial robots and machines, (that we also call *Robogamis*, in terms of *geometry*, *mechanisms*, *functional materials* and *fabrication*. We highlight their relation, potential and the challenges, and finally we present a systematic design methodology to facilitate their design process. We demonstrate applicability of our generalized methodology to the majority of robogamis presented in the literature; making it generic and extendable. We also demonstrate the validity and effectiveness of the method by designing a latest version of the jumping and crawling origami robot, Tribot. Tribot's design follows our proposed design process and for each step we evaluate design choices, qualify and characterize them. We close the loop by implementing a locomotion controller to accurately regulate Tribot's locomotion and compare it to the theoretical models. This work not only facilitates the design process of robogamis, but also leverages development by filling gaps in the research field and invites potential contributors from diverse areas of research.

The main contributions of this chapter are,

- Comprehensive study, including comparison of robotic origami mechanical design and conventional robot design;
- Development of a systematic methodology for designing origami-based multi-material machines and robots with multiple functionality;
- Validation of the design methodology with the crawling and jumping origami robot, Tribot.

## 3.1 Foldable Geometry

The ability to change shape is one of the key attractions of robogami platforms [116]. A quasi-2D robogami has an elevated DoF that can reconstruct several 3D geometries with structural softness. We categorize them into three main features: 2D to 3D passive folding assembly, 2D to 3D active self-folding and 3D to 3D shape transformation folding. Folding into different shapes requires prior definition of 3D shapes, their representation as a single 2D crease pattern and the kinematic relation between the crease pattern and 3D shapes in terms of fold sequence and fold angles. As in origami, a robogami structure consists of tiles (faces) connected by joints or hinges (creases) in a 2D lattice. As tiles are interconnected, then folding at any hinge changes the configuration of the surrounding tiles and consequently, the

overall shape. While the tile size dictates the resolution of a represented shape, their number defines the number of achievable DoF. An increased number of tiles complicates evaluation of kinematics and intensifies computation. Various geometric folding [117] and unfolding [118] algorithms were developed in the computational origami field to address origami shape reconstruction. However, these algorithms assume zero thickness geometry of the tiles, with no physical consideration. Many analytic solutions for kinematics of specific rigid origami patterns [119] and thick panels with zero thickness hinges [120] consider sharp revolute folds and there are few with curvature-like smooth folds [121] that reflect real scenarios [122], with trade-off of modeling compexity. There is also research on automated unfolding methods for some origami joint mechanisms [68] to a single material crease pattern, as well as folding algorithms for robogami self-folding sheets [25].

Currently, unfolding 3D shapes to decomposed and fabrication-ready multi-layer 2D geometries remains a challenging task. Also, for accurate shape reconstruction it is necessary to consider curvature angles and deformations as a function of material properties for physical implementation. For instance, folding a box pattern from thin tissue paper is different to folding thick corrugated paper; the latter necessitates extra lines along the folds to ensure curvature. As different geometries can generate different functionality and reverse, this two-way relation should be studied well to create task-oriented reconfigurable origami robots and machines.

## 3.2 Flexible Mechanisms

There is a diverse range of robogami movements. Some examples are translation [123], rotation [68], bending [59] and multiple deformations of sheets [62, 25] that are enabled by combinations of compliant fold mechanisms. Robogami links are planar tiles and arranged in open and closed chains, with tiles connected in series or parallel, respectively, as well as tree forms where a tile acts as a base for two or more tiles. Tiles are interconnected by flexure joints or hinges that do not require kinematic pairs and are made of a single, flexible material [124] with various possible patterns for folding, torsion, lateral bending, shear, compression, and tension [125, 126] with minimal friction, showing great versatility and customizability. Another important feature of robogami mechanisms is their ability to alter mechanical properties, for instance, a structure can evolve from soft to rigid state [127] by buckling, or by means of variable stiffness joints [64] to apply variable contact forces. Robogami mechanisms demonstrate high flexibility in producing various locomotion gaits like walking [29, 128] and crawling [31, 59] by alternating movements. Compliant mechanisms can store and release energy, having bi-stable properties [129], useful for jumping locomotion [60].

Modeling robogami mechanisms is not straightforward. Owing to the highly integrated nature of the layers, their behavior does not only rely on the mechanical properties, but also on the material characteristics. The classical models are still applicable to approximate the mechanisms of rigid origami with negligible joint thickness [120], however, in reality robogami

flexure joints have non-zero surface area [121] and non-linear elasticity [122] at high strains (>1 %), therefore, they should be characterized and included in the models to accurately predict motions and force translations. Flexure joints lack friction but introduce stiffness that counter acts to actuation forces that requires material characterization. Also, multi-tile robogamis have high dimensional fold space that needs to be addressed to achieve versatile mechanisms.

## 3.3 Functional Material Components

Mechanical components play critical roles in achieving robogami functionality in otherwise static and passive structures. Customizability of the material components is an important asset in robogami design. Actuators are essential in active robogamis. Besides being compact and lightweight to allow for distribution of several on a quasi-2-D lattice without overloads, the actuators should also be customizable and reversible in terms of force and motion to achieve flexibility in shape transformation and movement. They should produce high range of motion (0° - 180°) and sufficient torque to perform motions with multiple connected tiles, so electric drives are not effective at millimeter-scale. Therefore, alternative approaches using functional materials with shape memory effect are popular, due to their ability to transform from one shape to another upon thermal, electrical, light or chemical stimulation [77]. The typical shape memory materials are: shape memory alloys (SMA) [31, 78, 74, 70], shape memory polymers (SMP) [69, 73] and their composites such as polyvinyl chloride (PVC) [79], and pre-stretched polystyrene (PSPS) [27, 80]. Among these materials, SMA generates the highest force-to-weight ratio, being compact and customizable for embedding by multi-layer lamination processes with the trade-off of slow response rate (≈1 Hz), typical of shape memory materials, and low efficiency due to Joule heating. Their motion can be reversed by using an antagonistic pair.

The limitation of bandwidth and repeatable folding can be overcome by employing discrete inflatable pouch [65, 130] and elastomeric [110, 111] actuators. However, the high volumetric expansion of the actuators (>200 %) limits their distribution density and motion range for more complex multi-hinged patterns, like the Miura-ori pattern in Figure 2.25 presented in the previous chapter, which has several mountain and valley hinges connected at a single vertex. Moreover, such air-pockets require a pre-fabrication process, such as heat sealing or molding, before integrating into a robotic origami. They were implemented in limited numbers for moving pre-folded shape changing origami structures [112] with individual fluidic piping. Similarly, a vacuum-driven actuator has been proposed [113] for collapsing readily-folded origami structures by encapsulating them in an airtight film, which lacks 2D to 3D self-folding capability and control over the folding sequence.

For a comprehensive robotic system, embedded sensors play critical roles in feedback control. Compliant sensors utilizing changes in material properties upon mechanical input are also developed, such as resistive bending sensors based on carbon-ink [131, 132], liquid gallium-indium [133, 134], and solid metal alloy gauges like Inconel [71] and Cupronickel [78] backed by

a flexible material such as polyimide (Kapton) or silicone. However, the available solutions still lack accuracy and repeatability, suffer from noise and temperature variations, and therefore more accurate alternatives need to be studied for robust feedback.

Polyimide sheet [122, 135] is commonly employed for hinges being flexible and durable, also 3D printed [62] and molded [107] rubber hinges can function with high elasticity. Glass [21] and carbon [136] reinforced plastic, paper [123, 137], and ABS plastic sheets [61] are common for tiles and as structural backing being thin, light, and stiff.

## 3.4 2D Rapid Fabrication

For low cost and accurate mass production of robogamis, the possibility of fabricating them from a great variety of materials in a single process is a major challenge. Multi material-based additive manufacturing process using stereolithography is identified as an effective approach, however, the most current commercially available stereolithography systems face limitations in achieving very fine resolutions and the printable material is limited to a few polymers. At present, the large variety of functional materials like polymers and alloys still necessitate special fabrication techniques and equipment to handle them and there is no single fabrication process to manufacture robogamis. Some designs make use of additive process using 3D printers [26, 61, 138] and deposition [132], while the majority of them employ subtractive approaches, utilizing micro-machining technology [123, 21], and still a few use heat drawing or stamping [65] for shaping robots. The well-established subtractive methods like laser micromachining technology can process a wide range of materials rapidly with extremely fine features at meso-scale. The subtractive approach allows for rapid machining of several layers with high resolution and integrating into a monolithic process by lamination, known as smart composite microstructures (SCM) [59, 63, 20, 139]. This is beneficial for embedding extra functionality into the robot's body, empowered by flexure hinges and composite layers. To summarize, further developments are needed in integrated fabrication methods of multi-materials with minimized process steps and standardization of fabrication equipment and techniques for mass-manufacturing.

## 3.5 Material Characterization

Functionality and performance of robogamis is highly dependent on material choices, therefore, it requires insights into mechanics of materials. Conventional robots and machines have mechanical designs that are well defined and governed by rigid kinematic, motion and force models. Now, if we introduce multi-layer, multimaterial rigid and compliant components, these conventional design principles often do not apply due to the complex nature of their behavior. This is difficult to predict even for single isotropic material without characterization, whereas anticipating their combined behavior in multi-layer, multimaterial structure poses even greater challenges due to layer interactions. Moreover, the characteristics of functional

material vary greatly, not only with composition and geometry, but also with the fabrication process. For instance, a SMA material with the same composition and geometry displays different behavior if annealed at different temperatures or duration [78] or a resistive strain sensor, adapted for angle measurement, can display different resistance at different temperatures. This requires investigations into the materials characteristics of hinge, actuator and sensor under different loading and thermal conditions to enable cusomizability, as well as avoid discrepancies.

## 3.6 Design Methodology

Based on our earlier formulation of the design features and sub-features and analysis of their implementation in the literature, we unified the robogami mechanical design into a systematic design process given in Figure 3.1. Due to the interdependent nature of robogami geometry, mechanisms and functional materials, they are placed concurrently at the beginning of the design process. The design process is sequential within each block and top-down with connectedness (gray lines) for possible intervention with neighboring sub-blocks and a return loop for design modification and refinement.

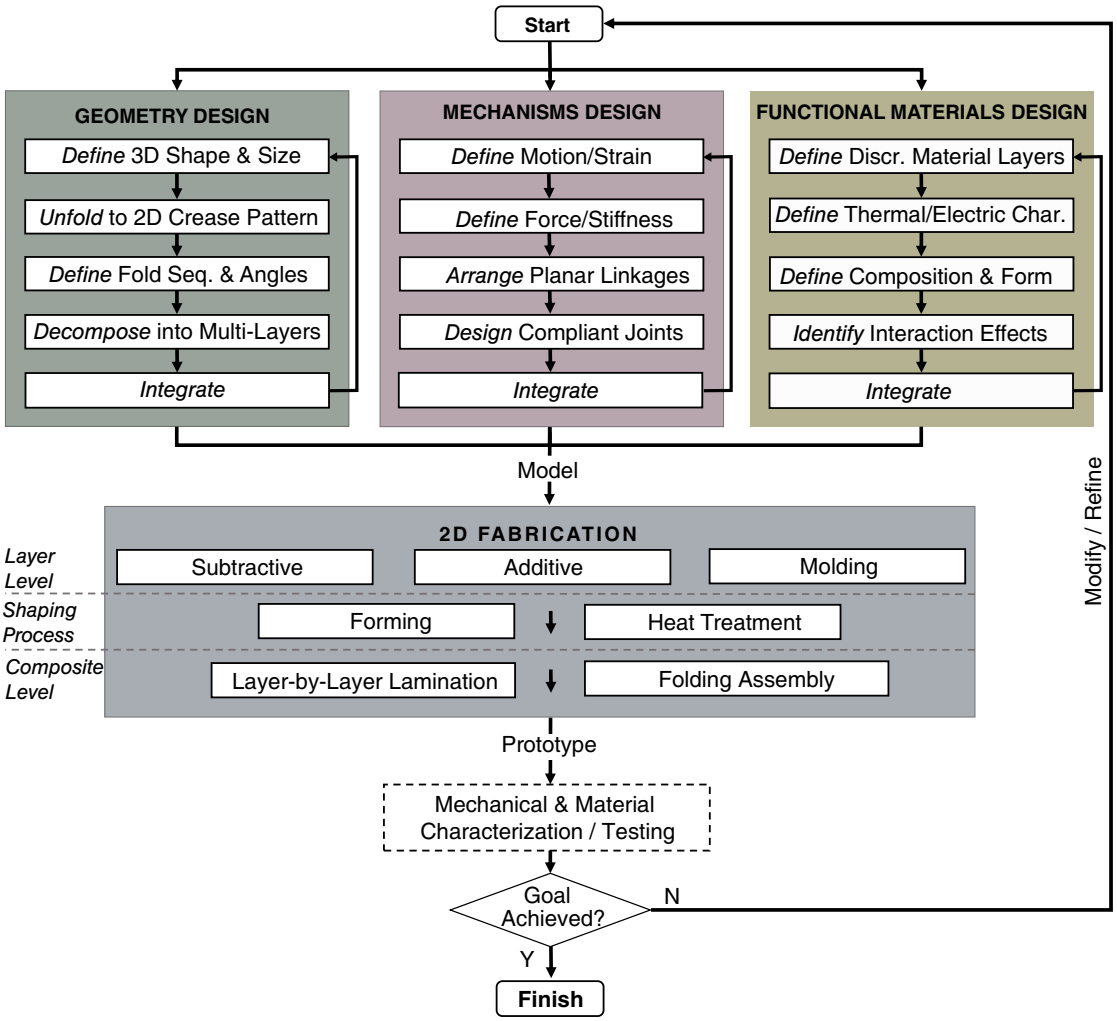


Figure 3.1 – **The proposed mechanical design scheme for prototyping functional origami robots and machines.** Depending on the design goals, the design process begins at any of the three features: geometry, mechanisms or functional materials and is then refined by iterative fabrication and characterization process. Apparent intervention at any of the top three features can be iterated among the neighboring features depending on their mutual relation. The proposed method is applicable not only for designing composite systems, but also for studying geometries, mechanisms or functional materials individually, backed by prototype 2D fabrication and characterization.

In the geometry design block, a robot's single or multiple 3D shape transformations are defined first, then they are deconstructed to a 2D crease pattern. Using a single creased sheet of material is impractical due to the different characteristics and functionality required for the tiles, hinges, actuators or sensors. Therefore, the crease pattern is decomposed into multimaterial layers for structural backing, compliant joints, actuators, sensors, heaters, etc. Fold sequence and angles, which relate the sandwiched layers (crease pattern) to the 3D shapes, are then determined. The crease pattern geometry is also closely linked to the shape

and placement of planar linkages and joints while designing the robogami mechanisms, therefore this two-way relation should be studied back and forth to optimize between shapes, forces and motions. While the mechanical properties of the discrete layers, including stresses and strains, and their combined behavior is modeled under the mechanisms design, their material properties and interactions, including thermal, electric or chemical, are studied under the functional materials design. For instance, a flexible strain sensor for measuring folding angles in close use with a thermally activated actuator, like SMA, besides having fitted geometry and compliance, should also have resilience to heat, which causes discrepancies in reading [78]. A less temperature sensitive sensor material should be used in this case or the sensor should be placed away from the heat-effected zones. In fact, the geometric (blue), mechanical (orange) and material (green) properties of robogamis, are essential in setting their desired models.

The 2D manufacturing process of robogamis is done in multiple steps at layer, intermediate and multi-layer levels. In the beginning, all discrete layers are prepared by machining, 3D printing or molding, then some layers, such as actuators, are shaped mechanically and heat treated for inducing the shape. Lastly, the layers are laminated layer-by-layer and assembled by folding. Some steps can be skipped, for instance using a multimaterial 3D printing of successive layers in one single go [61]. The prototype is finally characterized for mechanical and material response by loading and thermal or electrical input/output, respectively. Important knowledge of stiffness, strain, activation temperatures, hysteresis and other parameters are fed back to refine the model.

## 3.7 Applicability

The four essential robogami mechanical design features and sub-features are the nature of the most, if not all, robogami prototypes in the literature, including Berkley's Mini RoACH [140], Harvard's $\mu$-fly [141, 142] and self-folding origami [27], SNU's jumping Flea [60] and crawling Omegabot robots [59], EPFL's Crawler robogami [21] and origami gripper [64], Waseda's Paper robot [137], our first version of jumping and crawling robogami, Tribot [61] and the latest prototype presented in this work. The proposed design methodology is well-applicable to numerous prototypes, for instance, the design of an under-actuated origami gripper with adjustable contact forces [64], which focuses on SMP material for variable stiffness joints in a finger structure, by defining relation between its glass transition temperatures (material) to different stiffness levels (mechanism) and bending angles (geometry) of phalanges, embedded in a low-profile multi-layer structure along with heaters, sensors, tendon and backing. Each layer is machined using a laser micromachining station, some of which, like strain sensors and heaters are then wet-etched to have specific resistive properties, and laminated layer-by-layer by heat pressing. The joint prototype is further characrerized by tensile tests at different temperatures. Besides a complete system (multi-layer sandwich), the methodology is also applicable to sub-system and discrete layer levels. For instance, the torsional sheet $\Omega$-SMA actuator [78] design and fabrication process, starts at the functional materials block

by definition of SMA material and activation temperature, jumps to geometric shape (Ω) and folding mechanisms designs for desired motion and output torque, all then combined in a thermo-mechanical model. The modeling process is backed by machining of the geometric pattern on a SMA sheet, forming and annealing for shape programming, and its mechanical characterization for folding angle and torque response, as well as thermal parameters under different loading conditions. The characterized parameters, like stress, strain and phase temperatures are crucial in refining the actuator model for desired performance.

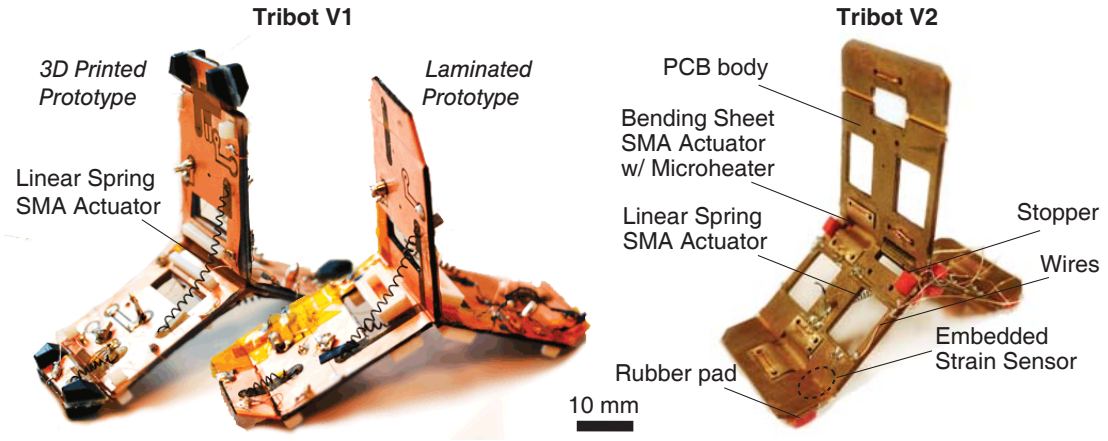


Figure 3.2 – **Two versions (V) of a crawling and jumping origami robot Tribot.** V1 presented in [61] is constructed of three layers of fiber glass body, copper-Kapton circuit and Kapton hinges, and powered by seven linear SMA spring actuators. The second version, presented in this paper, consists of two layers: PCB body and Kapton hinges driven by four torsional actuator and a linear SMA actuator. The second version consumes three times less power, jumps to set heights and performs side jumps.

To demonstrate the implementation of the proposed methodology in detail, we next design a second version of the origami robot Tribot from the ground-up, as a case study to follow the guidelines in Figure 3.1 step-by-step.

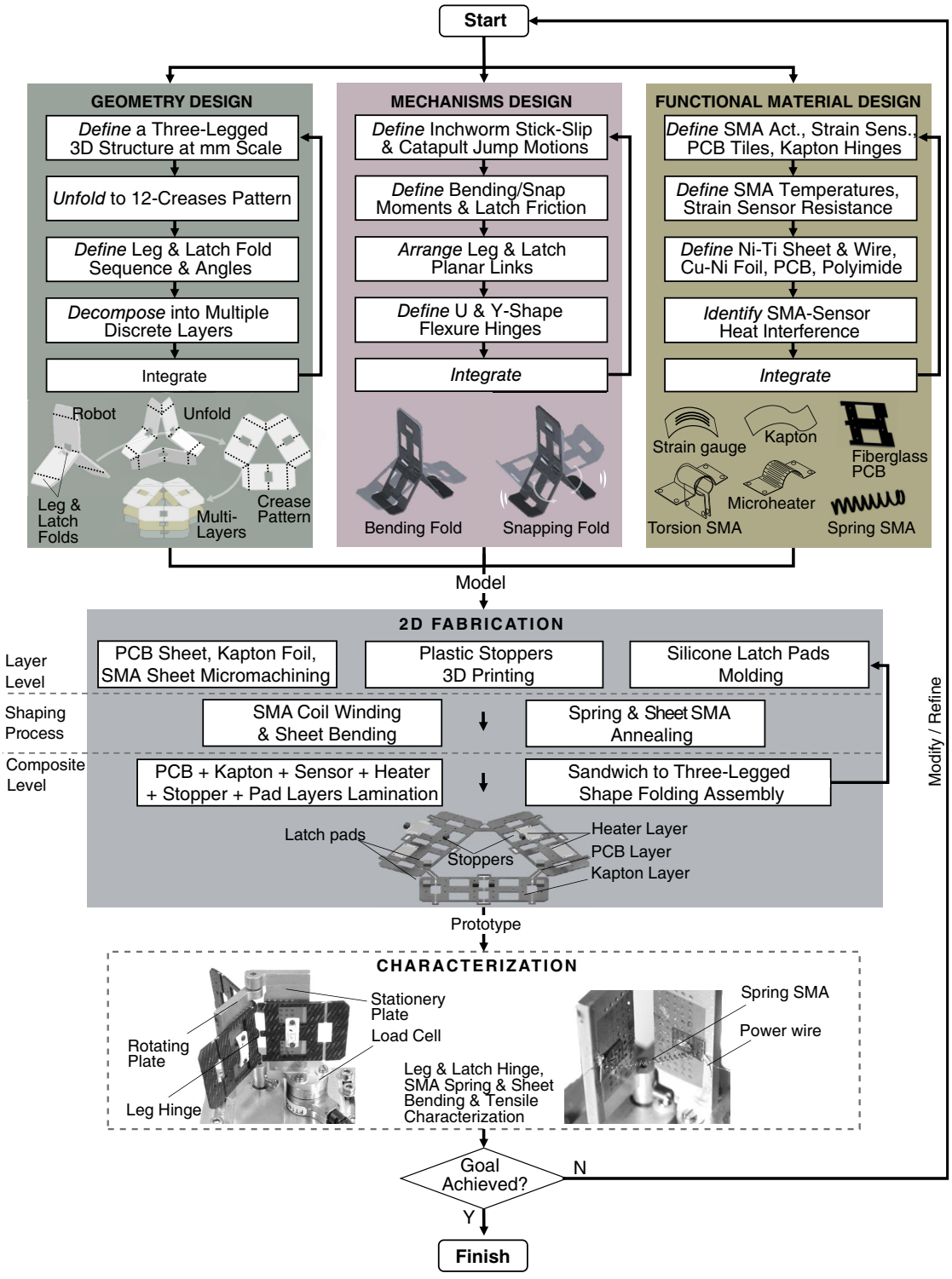


Figure 3.3 – **The mechanical design process of Tribot based on the proposed methodology.** The design begins with definition of the robot's crawling and jumping locomotion mechanisms and development of the geometry, mechanisms and material components that enable these functions. The prototype is finalized after multiple fabrication and characterization tests of the actuators and hinge joints by evaluating various design choices.

The new fabrication process of Tribot, enables embedding sensors for folding angle feedback, the more efficient low-profile Ω SMA actuators and PCB body in 2D lamination process. We first define Tribot's multi-locomotion mechanisms, then design its 3D shape, unfold it into a 2D crease pattern and then decompose into multi-layers. We then design the functional material components, and fabricate and characterize them. Finally, we develop a controller to regulate the robot crawling gait and adjust jumping height by power modulation.

## 3.8 Tribot, a Multi-Locomotion Mesoscale Robot

We demonstrate for the first time, a mesoscale multi-locomotion mechanism design capacity of robogami platform with Tribot [61], such as inchworm crawling and jumping by continuous (smooth) and discrete (snap) bending mechanisms, respectively, as shown in Figure 2.4a. Tribot crawls by stick-slip principle by folding and unfolding leg joint [61] (Figure 2.4b), flip to walk with average steps of 55 mm by snapping the side of the joint [96] (Figure 2.4c) and hop vertically as high as 215 mm by snapping the joint bottom (Figure 2.4d.) Besides active mechanisms, we demonstrate that robogami design principle also allows for embedding passive compliant mechanisms, such as the Tribot self-righting roll cage in Figure 3.4.

### 3.8.1 2D to 3D Folding Assembly

Unlike Origami paper art, which focuses on folding assembly of passive structures, robogami enables assembly of active, functional structures. This is essential to rapid manufacturing of complex shapes without assembling several separate 3D parts. We demonstrate this by folding assembly of a three-legged multi-locomotion origami robot, called Tribot, depicted in Figure 2.5. Owing to origami-inspired design, the robot addresses the key challenges of complex multi-locomotion mechanisms design. This complexity is originated from multiple mechanisms employed for performing different locomotion gaits and switching between them. However, since Tribot is made of a quasi-2D sheet of material, the design process is minimal and straightforward, while having several joints to perform different tasks and posses a scalable design. Initially, a 3D structure and mechanisms of the robot are defined and it is unfolded into multi-creased 2D pattern. Using a single material limits the functionality, therefore, the pattern is decomposed into multiple functional layers for actuation, flexible hinges, structural backing, stopper among others. After processing each layer and stacking, the multimaterial composite is folded and assembled to produce Tribot's 3D structure with embedded mechanical functionality.

The final structure of the robot carries three legs, where leg 2 and leg 3 are used for maintaining contact with the ground while the upper leg helps to spread the lower legs when pushed downwards. The legs connect in the center with a Y-shaped hinge, enabling independent movement of each leg about the central axis and stable locomotion on any two legs (edges). The central hinge folds and unfolds by compression and extension of linear spring SMA actuators. To achieve bidirectional crawling, rubber pads under the foldable latches exert

ground contact upon latch folding and unfolding. Hence, the crawling gait is generated by stick-slip movement of rubber latches in both direction. It uses the same compliant joints and SMA actuators connected in antagonistic fashion for leaping up vertically by adjusting its body and producing a snap-through motion. The robot design benefits from symmetry, which allows to have identical actuators on all joints. Tribot is a unique platform with minimal design and multi-functionality, assembled by folding.

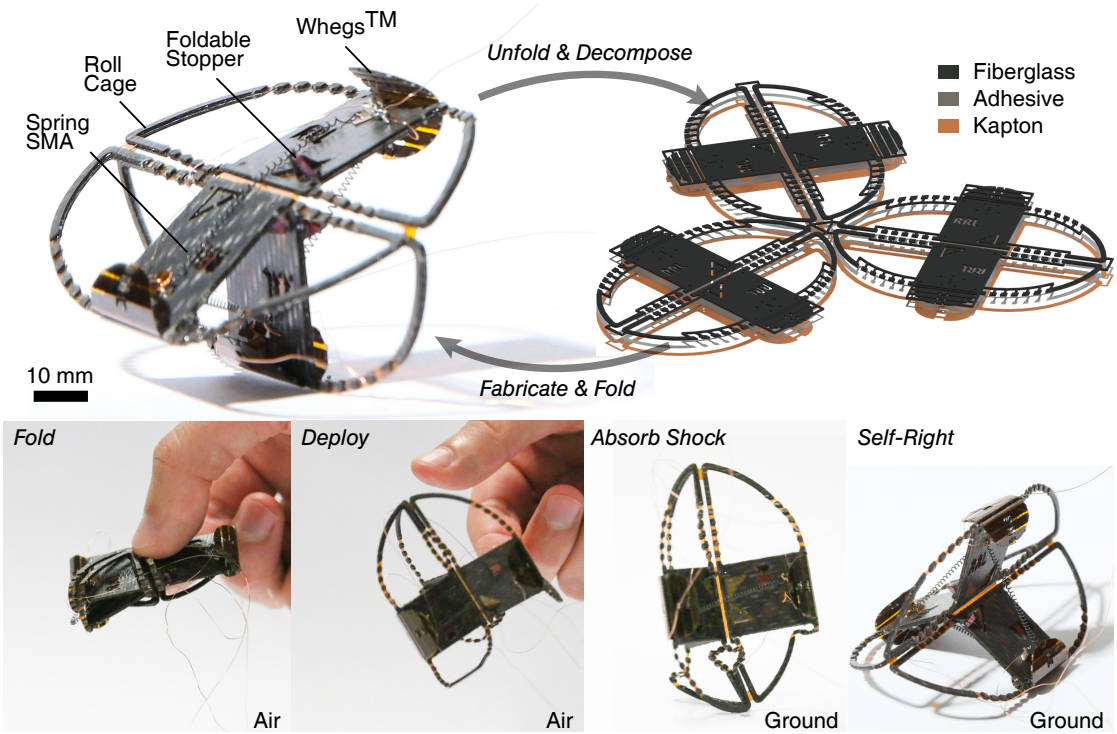


Figure 3.4 – **The design of a foldable, deployable and self-righting version of multi-locomotion origami robot Tribot. [96]** The compliant elliptic cage mechanism with hinges enables robot to fold to nine times smaller volume than the deployed state, absorb shock upon drop and impact with the ground, and ensures landing in upright position at all times. The Whegs™) on all three legs facilitate Tribot's body rotation for rolling locomotion upon snapping of the side hinge. The structure is unfolded, decomposed into functional layers, such as fibreglass for rigidity and Kapton for flexible hinges, both bonded by means of adhesive layer.

### 3.8.2 Versatility of Mechanism Design

Multi-layer folding assembly allows for embedding diverse functionality into robogami geometries. Figure 3.4 displays the foldable, deployable and self-righting version of Tribot with an elliptic compliant cage around the legs and wheel-legs (Whegs™) protrusions [96]. The elliptic shape of the compliant roll cage self-rights the robot and protects it from impact during landing, while the curved protrusions aid Tribot in performing smooth rolling locomotion. However, this requires enlarging the robot's structural frame, adding more than two times its

original tree-legged volume. To overcome this drawback altogether, we have designed the entire robot to be flat foldable. All functional features of the robot's design can be folded to nearly 180° relative to any adjacent part, allowing the robot to be folded to nine times smaller of its deployed volume, as shown in Figure 3.4. A number of hinges along each strut of the roll cage enable it to be folded over the central body once any two of the three legs are brought together. Due to the fact that these hinges are flexible, this comes with the additional benefit of making the roll cage compliant and damping impact forces during a fall. In addition, the previous version of Tribot utilized rigid stoppers for this purpose, which imply that the robot cannot be folded flat. In this version we have implemented hinged triangular elements that are pop-up to an upright position through rubber bands when the robot folded flat and deployed. All these features are still embedded through multi-layer decomposition, 2D processing, and assembly by folding, showing the versatility of the method.

## 3.9 Tribot's Flexure Joints and Locomotion Mechanisms

As for insects, multiple modes of locomotion is highly beneficial for millimeter-scale robots for both mobility on changing terrains and for traversing obstacles [143]. While some gaits, like crawling and walking, require smoothly movable limbs, jumping necessitates energy storage and a rapid release mechanism for lift-off. To combine two locomotion modes, jumping and crawling, in a single robogami structure, we designed a smoothly folding and unfolding flexure joint with links as legs to generate inchworm crawling as depicted in Figure 3.5, bottom left. Propagation is generated by a stick-slip mechanism that grips and releases the contact surface. There are two choices for this: using anisotropic friction pads [59] that apply one-way friction, or an active latch with an adjustable friction contact. We opted for the second method to enable two-way crawling locomotion. Adding jumping functionality on top of the crawling gait, without using a separate mechanism or modifying the existing one is a real challenge.

We found a solution that lies in the nature of the compliant joints that show a bi-stable property when compressed uni-axially. A flexible joint buckle, when compressed, stores energy and snaps to the side of the applied force. If adjusted properly, the snapping mechanism can generate high impact forces to lift the robot off the surface, resulting in a vertical jump (see Figure 3.5 top-right). For jumping to any of two sides in a ballistic projectile, the launching angle should be less than 90°. Therefore, we added a third upper leg to shift the robot's center of mass in the direction of the jump for horizontal propagation.

#### Crawling

For a single crawling step the mechanism is as follows: the rear sticky latch raises and disengages from the ground, then the bottom of the central joint closes allowing the rear leg to slip in the direction of the front leg. The rear latch then lowers and engages with the surface and the front latch raises to disengage. The bottom of the central joint opens, resulting in slipping of the front leg forward. This stick-slip step-cycle can be repeated in both directions enabling

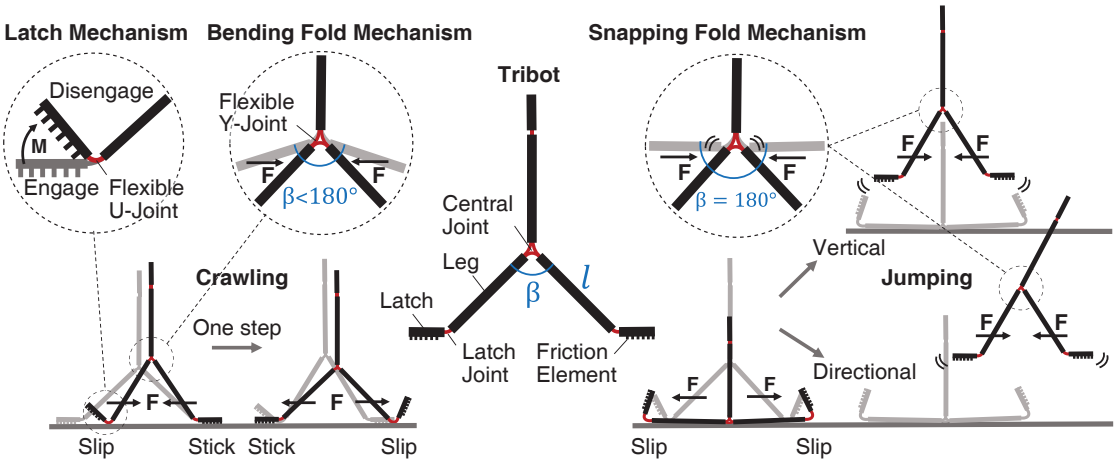


Figure 3.5 – **Design of two locomotion mechanisms of Tribot.** Compliant origami hinges generate smooth and snap folds that can be employed for crawling (left) and jumping gaits (right), respectively. The robot has five links, three of which are for legs and two for latches. The legs are connected at the center with a Y-shape flexure joint, and two latch links contain high friction material for stiction. When activated properly, smooth fold and latch mechanisms generate an inchworm crawling while the snap mechanism generates vertical or side jumps depending on the upper leg position.

the robot to propagate to the desired position in multiple step cycles as shown in Figure 3.5, left. The kinematic model for crawling is similar to a single DoF two-link robotic arm clamped at one end and moving with the other end, constrained to the axis of motion as apparent in Figure 3.5. Then the distance between two legs at the contact point on the sliding surface can be calculated as follows

$$s = 2l \sin \frac{\beta}{2} \tag{3.1}$$

where $l$ is the leg length and $\beta$ is the angle between the two lower legs. Then the step size of crawling in each step cycle can be calculated as the difference between the initial and final distance between two legs as

$$\Delta s = s_f - s_i \tag{3.2}$$

where $\Delta s$ is the step size, $s_i$ and $s_f$ are the initial and final distances between two legs, before and after each step cycle, respectively. The total displacement of the robot is the increment of

the steps in each step cycle

$$d = \Delta s_j + \Delta s_{j-1} \tag{3.3}$$

here, $d$ is the displacement, $\Delta s_j$ and $\Delta s_{j-1}$ are the current and previous steps of the robot in the direction of locomotion.

**Jumping**

If the bottom hinge is opened to an angle greater than or equal to 180° and compressed, the bottom legs close instantly against the contact surface creating a ground reaction force (GRF) which lifts the robot off the surface. The velocity and height of jump can be computed based on three methods: the impulse-momentum using GRF data, the work-energy and the flight time methods [144]. We adopted the latter approach to estimate the height of the robot jumping, due to simplicity of measuring the flight-time. For the robot in flight

$$v_f - v_i = -g(t_f - t_i) \tag{3.4}$$

where $g$ is the gravity, $v_i$ and $v_f$ are the initial and final velocities at the instant of take-off and landing $t_i$ and $t_f$, respectively. If the height of the robot at the instant of take-off is the same as that at the instant of landing, then $v_i = -v_f$, then the robot's take-off velocity is given by

$$v_i = \frac{g t_{flight}}{2} \tag{3.5}$$

where $t_{flight}$ is the flight time given by $t_f - t_i$. If we consider the changes in kinetic energy and gravitational potential energy between the instant of take-off $v_i$ and the instant the robot reaches the peak of the jump then

$$\frac{1}{2} m v_i^2 + mgh_i = \frac{1}{2} m v_{peak}^2 + mgh_{peak} \tag{3.6}$$

here, $h_i$ and $h_{peak}$ are the take-off and the height at the peak, and $v_{peak}$ is the velocity of the robot at the peak. The velocity at the peak of the jump is zero, and so the jumping height is

given by

$$h = h_{peak} - h_i = \frac{v_i^2}{2g} \tag{3.7}$$

## 3.10 Tribot's Geometry and Multi-Layer Decomposition

Tribot's locomotion mechanisms require two legs to be in contact with the ground at all times. The legs should be planar and sufficiently wide to maintain stability without falling to one side. An origami structure with three planar tiles connected by a Y-shaped flexure joint can be easily constructed with three additional latch tiles extending from each leg as shown in Figure 3.3. This structure is unfolded to a delta-shaped 2D crease pattern with six leg and six latch tiles separated by 12 creases for 2D fabrication purposes. The assembly to the three-legged structure requires one back-to-back (180°) folding along the three hinges at the delta vertices and 120° along the central hinges. The crease pattern is decomposed into a flexible and rigid layer as illustrated in Figure 3.6. Backed by the rigid layer, the flexible layer folds only along the segments without the rigid backing, the gaps, making flexure hinges. The gap size affects the stiffness of the hinge as well as the fold angle of the tiles; the larger the gap, the less stiff is the hinge and it has more freedom to fold flat. Therefore, there should be a balance between stiffness and foldability of the flexure hinges when designing the gap size.

## 3.11 Functional Material Components

Tribot's locomotion mechanisms and geometry require four essential components: actuators for driving the folds, angular sensors for controlling the fold angles, flexible hinges and rigid tiles. Material selection and component design is crucial for the robot's operational performance, durability, fabrication effort and cost and for our design we picked the materials accordingly. Crawling gait requires bending motion of the central and latch hinges, while jumping necessitates exertion of linear force on the central hinge to generate a snap. Among the actuator options towards a lightweight origami robot, SMA, SMP or IPMC may be considered for actuation. A linear spring SMA actuator provides an amiable and unique solution to both smooth and snap fold mechanisms if placed across two legs as in Figure 3.6, having a high power-to-weight ratio and a compact design. The actuator can also be easily customized by changing the wire and coil diameters, coil number and input power. In the previous version of the robot, we employed seven spring actuators; three for legs and four for latches. To reduce power consumption, we replaced six linear spring SMAs with the four torsional Ω-SMA sheet actuators we presented in [78]. Each low-profile Ω-SMA with the micro-heater layer consumes only 0.5 W power, considerably lower than with Joule heating and allows mounting across the leg and latch flexure hinges as was shown in Figure 2.3b. This reduces the robot's energy consumption by three fold for the same activation time and sequence. In our design, we rely

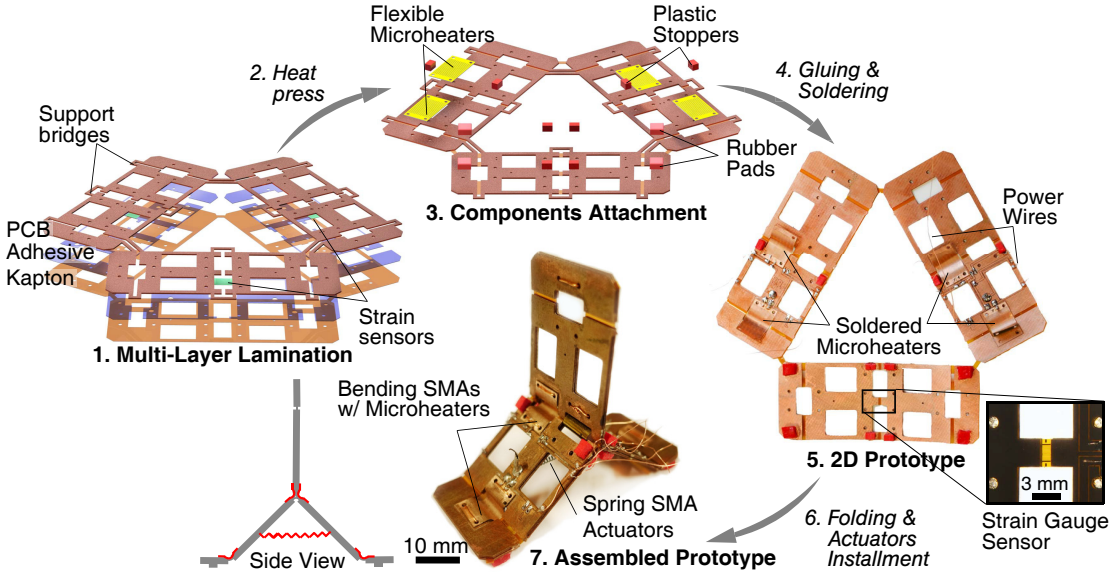


Figure 3.6 – **Fabrication process of the three-legged multi-gait origami robot, Tribot.** PCB and Kapton layers are processed in 2D and bonded together by an adhesive layer. After, three flexible strain sensors and four Ω-SMA micro-heaters are attached across the leg and latch joints, eight stoppers and four rubber pads are glued and the power wires are soldered onto the PCB. Finally, the 2D structure is folded to obtain the 3D robot, then four torsional SMA actuators are inserted under the micro-heaters and the spring SMA actuator is attached across the bottom legs. The actuator placement is shown on the robot's side view.

on the elasticity of the flexible hinges to reset the actuator passively to an open configuration while cooling. A single spring SMA actuator remains to drive the bottom leg joint by applying a moment and compression force while crawling and jumping, respectively.

Attaining certain folding angles necessitates angular sensors for feedback. The sensor needs to be low profile and flexible, and able to withstand multiple folding cycles and high impacts during the jump process. We adapted the off-the-shelf thin Cupronickel (Cu-Ni alloy) strain sensor (120 Ω, RS Components Ltd) for this purpose, being linear and repeatable. A thin, flexible and durable 50 $\mu$m thick Kapton-polyimide film (DuPont) is well-suited for compliant hinges that can withstand quick snap motions without tearing apart (UTS=33.5 GPa), can be laser cut rapidly and resist high temperatures (up to +400 °C), suitable for multi-layer heat pressing. A printed circuit board (PCB) sheet, glass-reinforced epoxy laminate (FR-4) with double-sided copper coating, fits well for constructing the robot's light and stiff body, as well as for onboard power and signal circuitry. For stick-slip crawling, Tribot requires high friction pads for latching onto the surface, that we designed from silicone rubber. ABS plastic stopper elements were introduced to constrain the kinematics of the legs during locomotion as well as robot proper alignment and balance before jump. The hardware components along with their characteristics are summarized in Table 3.1.

Table 3.1 – Tribot Components and Specifications

| Components | Dimensions ($mm^3$) | Material |
|---|---|---|
| 4 Torsional SMAs | 12×8×2.5 | Ni-Ti sheet t=0.1 mm |
| 1 Linear SMA | 25×1.5×1.5 | SMA wire d=0.25 mm |
| 4 Micro-heaters | 12×8×2.5 | Cu-Polyimide t=0.04 mm |
| 3 Strain sensors | 6×2.5×0.06 | Cu-Ni t=0.1 mm |
| 1 Hinge layer | 106×93×0.05 | Polyimide t=0.05 mm |
| 1 PCB tile layer | 106×93×0.4 | Cu-Fiberglass t=0.4 mm |
| 4 Rubber pads | 3×3×1.5 | Silicone |
| 8 Stoppers | 2.5×2×1.5 | ABS plastic |

## 3.12 2D Fabrication and Characterization

The components described above are combined in a multi-layer lamination process as illustrated in Figure 3.6. The robot's rigid layer is machined from 0.4 mm-thick PCB using a PCB plotter (ProtoMat S63, LPKF Laser and Electronics AG) with circuit traces for powering the actuators and sensor reading, whereas the hinge layer is cut from a 50 $\mu$m-thick Kapton sheet on the laser-micromachining station (LAB 3550, Inno6 Inc.). Three strain gauge sensors are placed between the PCB and Kapton layers on the leg joints and the layers are bonded together by an adhesive film (Poli-Melt 701, Poli-Tape Group) under heat press (Carver 3853CE, Carver, Inc.) for two minutes at 160°C and 90 N. The bridge supports on the PCB layer make a hinge gap and ease alignment with the Kapton layer and cut-off after bonding. Six plastic stoppers are 3D printed and four rubber latch pads are molded and glued onto the PCB layer as in Figure 3.6. Four microheaters and signal wires are then soldered onto the PCB pins. Finally, the structure is folded and the spring and torsional SMA actuators are installed. The robot's side view in Figure 3.6, bottom, shows the actuator placement scheme and it is similar to the linear and torsional approaches, illustrated in Figure 2.3 in the previous chapter.

The robot design is finalized after three iterations based on the back and forth design of the geometry, mechanisms and the functional materials, prefabrication and characterization tests. The first iteration was with a glass fiber body with different actuator placement, the second was with an additional Kapton-copper circuit layer, whereas the last prototype combined both in a PCB body as illustrated in Figure 3.6. The flexure hinge thickness and gap were decided based on the SMA actuator torques that are given below.

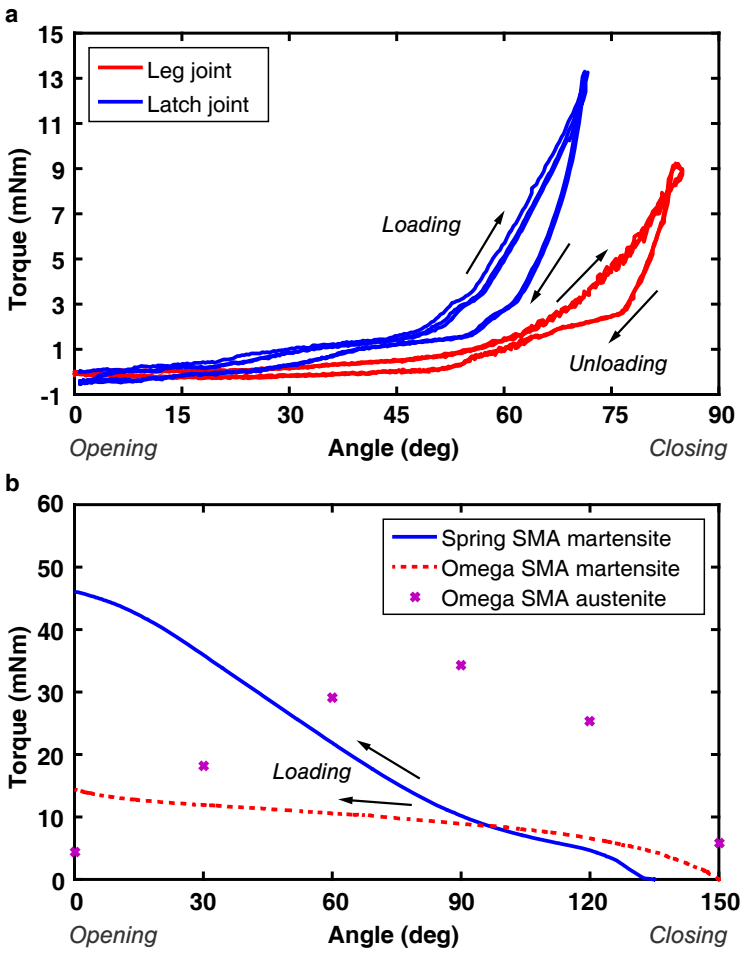


Figure 3.7 – **Three consecutive loading and unloading test plots of the leg and latch hinges made of Kapton.** Here, the latch hinge is closed to 70° while the leg hinge is closed to 80°. Torque is measured continuously for angular deflection while loading and unloading. Loading test plots for the Ω-SMA and spring SMA actuators in martensite state at room temperature as well as blocked torque response of the torsional actuator in austenite state. For martensite, the torsional actuator is first placed in a closed configuration and then loaded to open, while the spring SMA is pulled from compressed state to extended state. The blocked torque measurement of the Ω-SMA is done at different angles.

### 3.12.1 Characterization of Leg and Latch Hinges

In Tribot, the leg joints are driven by either the spring or sheet SMA actuators, whereas the latch joints are folded only by means of sheet actuators. It is important to characterize the actuator torques and hinge joint stiffness to maintain a two-way motion. Stiffness of the compliant hinges changes with the properties of the flexible material used, its thickness and the surface area of the gap between two rigid tiles. We set hinge gaps at 1.5 mm for foldability of 180° considering the thickness of the Kapton and PCB layers. After back-to-back folding

assembly, the robot has latch hinges with double layer Kapton with thickness of 100 $\mu$m and a surface area of 17×1.5 $mm^2$, and the leg hinges formed by a double layer of Kapton forming a Y-shape. Figure 3.7a displays three loading and unloading cycles of the leg and latch hinges using the torque measurement apparatus depicted in Figure 3.3, below. The maximum torque measured for folding a single leg hinge to 80° was approximately 9 mNm, while the latch joint had higher stiffness with a torque of approximately 13.5 mNm at 70° of deflection.

### 3.12.2 Torsional and Spring SMA Actuator Characterization

The performance of SMA actuators is primarily related to their metal composition and geometry. Both the spring SMA and torsional Ω-SMA actuators are characterized on the torque apparatus in two states; austenite when heated and martensite at room temperature. In austenite, the Ω-SMA actuator is in a closed shape and spring SMA is compressed. The loading or opening of the torsional SMA and extension of the spring SMA is done in martensite phase. Figure 3.7b depicts the blocked torque generated by the Ω-SMA actuator at different angles with a maximum at 34.1 mNm. The loading tests for both actuators in martensite state display the maximum torque of 15 mNm for the torsional actuator and 46 mNm for the spring actuator. This test reveals that two torsional actuators placed at the leg side hinges generate total torque of 68.2 mNm in austenite, and are able to extend the spring SMA in martensite, unfolding the bottom hinge. Also, the reverse is true for the spring SMA that has higher torque in austenite than that of torsional actuators in martensite, and able to fold the bottom hinge. Ω-SMA actuators produce sufficient torque to fold the latch joints and the motion can be partially reversed at cooling process of the actuators due to a non-considerable difference between the hinge and actuator holding torques.

## 3.13 Gait Controller Design

Tribot's gait patterns require specific sequences of activation of the folds by attaining set folding angles. The majority of robogami prototypes considered a predefined activation sequence in an open-loop [31, 59] and only a few have integrated sensory feedback for closed-loop angular control of the folds, using an On-Off controller for torsional SMA actuators [21, 132]. However, the On-Off method has high angular oscillation errors due to discontinuity of control input to achieve angles, therefore, we implemented a PID controller with PWM duty modulation to improve this discrepancy. We can control the angular positions of the torsional Ω-SMA and spring SMA actuators by PWM control of the input power, and the angular feedback from the strain gauges embedded into leg and latch joints. We design a PI controller where the bending angle $\theta$ is controlled as

$$D = K_p(\theta_{set} - \theta) + K_i \int (\theta_{set} - \theta) \tag{3.8}$$

Here $D$ is the PWM duty value of the power supplied to the actuator, $K_p$, $K_i$ are the proportional and integral gain constants to minimize the error in the bending angle, which is the difference between the set angle, $\theta_{set}$, and the measured angle, $\theta$, coming from the strain sensor. To avoid over-heating of the actuator, we limited the controller duty value output to $D_{lim}$, which is $0 \leq D_{lim} \leq 1$.

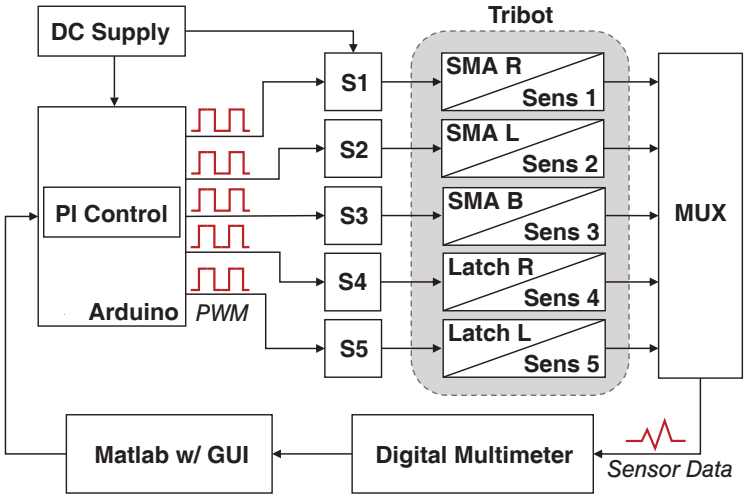


Figure 3.8 – **Schematic of Tribot test setup.** Robot parameters are set in Matlab/GUI, whereas the PI controller runs in the Arduino board and produces PWM signals with error-dependent duty, to the five switches (S) that decide each actuator's power. The sensor data is measured by DMM and fed back to Matlab.

For jumping, we regulate the robot's jumping height to avoid obstacles of different sizes. Jumping height changes upon variation in the power level of the spring SMA actuator that defines its stiffness. Input power to jumping height relation is experimentally tested and compared to the heights calculated from the model in (3.7).

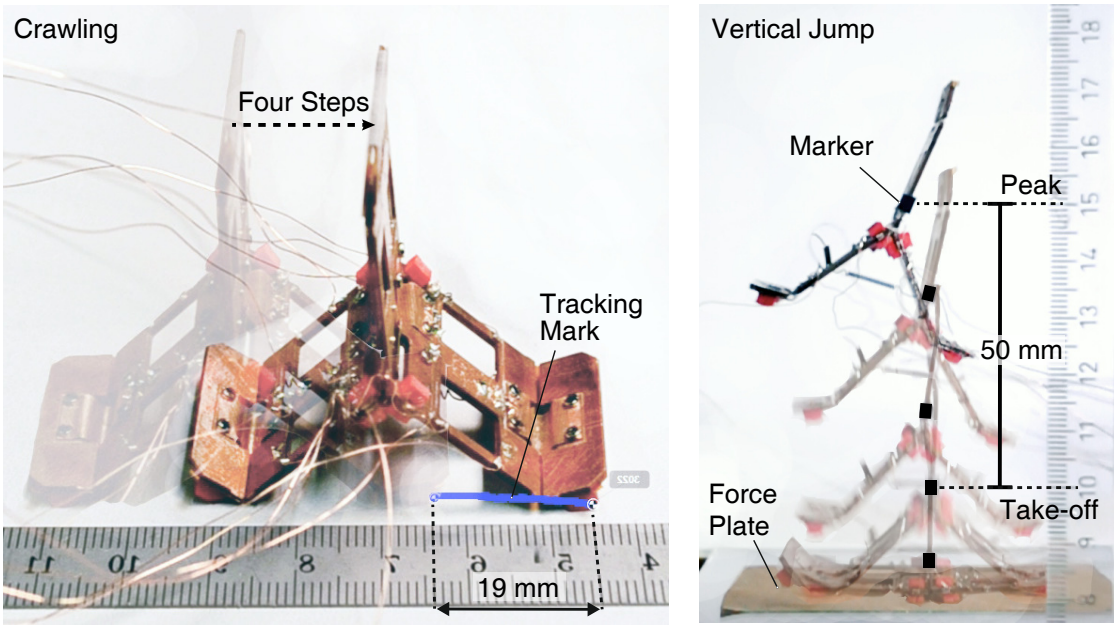


Figure 3.9 – **Tribot in crawling and vertical jumping phases.** For a reference step of 5 mm per step cycle the displacement of the robot after four consecutive step cycles measures approximately 19 mm. The maximum jumping height of the robot is 45 mm when the spring SMA is powered to 3.7 W.

## 3.14 Experimental results

We tested the crawling gait by implementing the PWM duty controller described above and compared the robot's jumping height with that calculated from the model by varying input power to the spring SMA actuator. We also demonstrated the directed jumping capability of the robot with an obstacle. For the experiments, the setup is as illustrated in Figure 3.8, where an Arduino Mega-2560 microcontroller is employed to run the PI controller loop and drive five switches (S) connected to the actuators on the robot with PWM signals. The controller decides which actuator to activate and the level of power depending on the error between the actual and reference angles. We read the resistance change data from the sensors by a digital multimeter (DMM) (USB-4065, NI) that has a single channel and we overcame this using a multiplexer (MUX) circuit. DMM and Arduino are interfaced with Matlab and graphical user interface (GUI) where we calibrated each sensor and defined resistance to angle relation as linear, set controller parameters and recorded data.

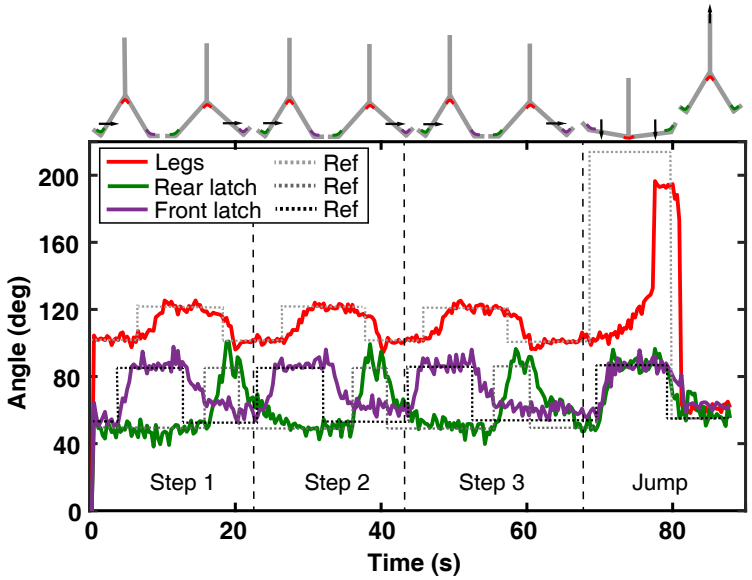


Figure 3.10 – **Closed-loop control response of Tribot hinge folding**. The plot shows the angular response of the leg and latch joints for realizing a 5 mm step size for three consecutive step cycles and then jumping. The actual angle response at each joint follows the set angles calculated by the inverse kinematic model.

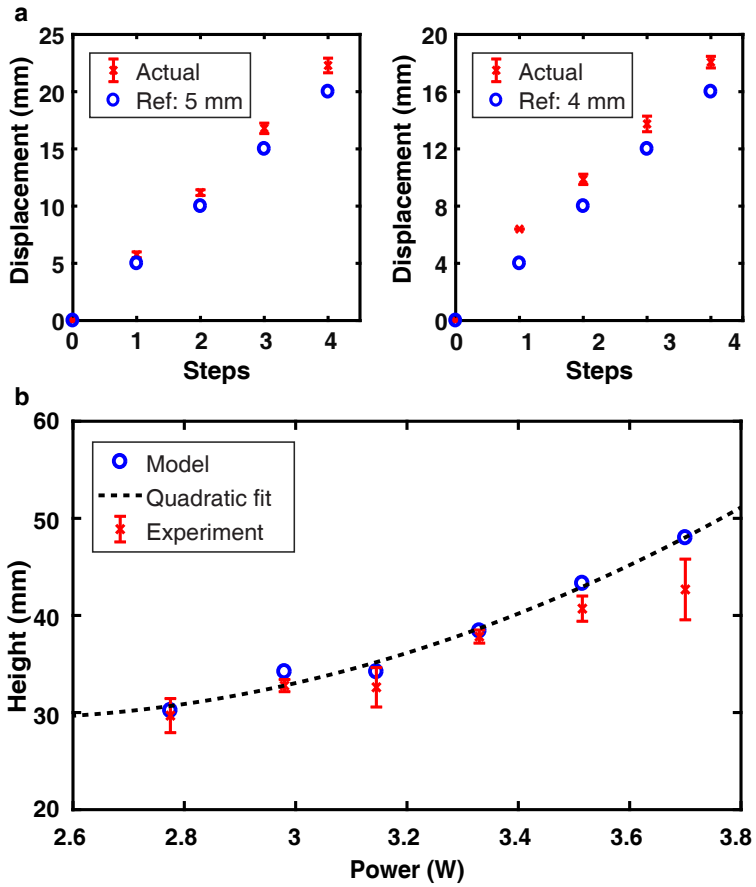


Figure 3.11 – **Closed-loop experimental vs theoretical crawling step size.** **a**, step size plots for four consecutive crawling step cycles of the robot. Each experiment is performed twice and their average is plotted along with error bars. The robot can accurately repeat a 5 mm step size reference (left) computed by forward kinematics while for 4 mm reference (right) there is a large error in the first step, which shifts the actual displacement plot above the computed one, however the rest of the steps are realized with approximately 4 mm step size. **b**, the measured and calculated vertical jumping heights plot for different spring SMA power values. Each experiment is performed twice and their average is plotted along with error bars. The maximum error of 5.3 mm occurs at the maximum power of 3.7 W.

### 3.14.1 Crawling Gait

Closed-loop control of the joint angles allows repeatable regulation of the crawling step size, hence the total travel distance of the robot can be defined prior to crawling. The angular measurement from the strain sensors at the joints for three crawling steps with step size of 5 mm followed by a vertical jump is depicted in Figure 3.10, which shows accurate angular positioning of the bottom and latch hinges for the reference angles calculated from the inverse kinematics given in (2.2). Due to the single-sided effect of the control input, the actuator returns (cools) by natural convection which results in oscillation below 5° for the left latch and

leg folds. Overshoots in the angular transition are due to the initial temperature overshoot of the SMAs. In jumping phase, the actual angle did not reach the reference as the torsional actuator torques were limited to further extend the bottom spring. The experimental results for 5 mm and 4 mm step size crawling in each of four step cycles along with the expected step size is depicted in Figure 3.11a, left and right, respectively. The results were analyzed from the video images using the open source program Tracker. For 4 mm step reference, a large error in the first step shifts the displacement curve above the reference and the rest of the steps were close to 4 mm, respectively. There are multiple factors of mismatch between the actual and the theoretical step size, like SMA non-linearity, sliding caused by imperfect sticking of the latches, among others.

### 3.14.2 Jumping Gait

To validate the model for vertical jumping, we studied the robot's jumping on a plate with force sensor (Nano 17, ATI Instruments) as in Figure 3.9. The height of jumping is varied by changing the PWM duty value to adjust power to the bottom spring SMA. We employed a high speed camera (Sony RX100 IV) with video recording speed of 480 fps and placed a ruler scale. The force sensor provides GRF information at take-off and landing, hence the flight time. The flight time for each power input is used to calculate the take-off velocity of the robot using the relation in (3.5) then the jumping height using (2.5) and is compared to the actual height of jump measured by the Tracker program as in Figure 3.11b. The initial reference height of the robot is taken as position of the black marker at the instant of take-off, when the robot stands at full height; and the jumping height is the difference between the initial and peak marker positions. The maximum jumping height measures around 45 mm and the error in prediction of the height was 5.3 mm.

Finally, we tested the directed jumping capability of the robot in an obstacle avoidance scenario with an inclined plate two centimeters high at one end, as depicted in Figure 3.12. Here, since one of the torsional actuators is kept active while compressing the spring actuator, the robot's center of mass shifts in the direction of the active torsional actuator (see Figure 3.5) and the robot jumps in that direction, here to the right. The robot is preprogrammed to jump onto the plate, slide down and stand again, which is accurately performed.

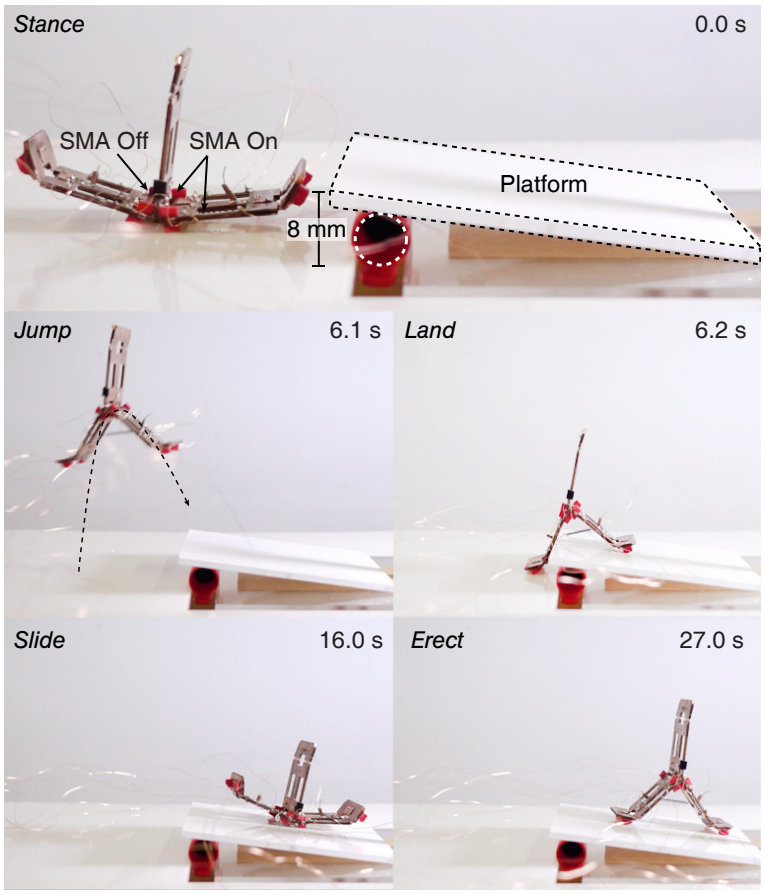


Figure 3.12 – Obstacle avoidance scenario with directed jumping of the multi-gait robot. The robot crawls until it faces the obstacle of two centimeters high (0.0 s), triggers itself for jumping (6.0 s), jumps in the direction of the obstacle by steering the upper leg (6.1 s), lands (6.2 s), triggers itself again to slide down the platform (16.0 s) and finally stands up (27.0 s).

Table 3.2 summarizes two Tribot versions; one presented in [61] and the one considered here. The earlier prototype was lighter and utilizes seven linear spring SMA actuators of 300 $\mu$m wire diameter that each, when activated, consume up to 4.4 W. This shortfall was improved in the new prototype by introducing the torsional SMAs that consume a maximum of 0.5 W each and the bottom spring for jumping is replaced by a linear spring SMA with a thinner 250 $\mu$m wire diameter that consumes up to 2.96 W. The total power consumption for jumping is improved more than three fold over the earlier version. Using the proposed design methodology, we improved the overall design of the new prototype in terms of power consumption, functional layers and controllability. The jump height is four times less than that of the previous version's, 160 mm. This is due to the torsional actuators at the central hinge that oppose the compression and snap motion, also the robot mass is increased by 30 % and a smaller wire diameter is used for the linear actuator that generates less force. These factors reduce the lift-off speed hence height of jump, however the cost of transport for both was comparable. Moreover, we modeled the jumping gait and experimentally studied height of jumping as a function of input power in

the new prototype and further, directed jumping was successfully implemented for obstacle avoidance. Reducing the power consumption allows for untethered autonomous operation in the future by equipping the robot with a battery, controller and sensors.

Table 3.2 – Comparison of Tribot Version 1 and Version 2

| | Version 1 | Version 2 |
|---|---|---|
| LxWxH ($mm^3$) | 63×34×20 | 55×25×50 |
| Weight (g) | 3.9 | 5.7 |
| Material | GRP, Cu-Kapton, Kapton | PCB, Kapton |
| Actuators (SMA) | 7 linear | 4 torsional, 1 linear |
| Jump power (W) | 16.28 | 4.96 |
| Directed jump | No | Yes |

## 3.15 Conclusion and Discussion

We present a comprehensive and systematic mechanical design methodology for multimaterial integrated robots and machines, called robogamis. The design process is categorized into four important design features: geometry, mechanisms, functional materials and fabrication, and we show their differences and similarities with respect to conventional robots, as well as highlight challenges for both. Based on this, the analysis of the literature on construction of such machines and the developed state of the art robotic systems, we establish a systematic design methodology from the ground-up and demonstrate its generality and applicability for designing and fabricating multimaterial integrated robots and machines.

We demonstrated the design process of the novel, crawling and jumping origami robot Tribot from the ground up by following the proposed design methodology step-by-step to showcase the applicability of our method. We designed Tribot's three-legged geometry decomposed to multimaterial layers, crawling, vertical and side jumping minimal multi-locomotion mechanisms, functional materials, including flexible Kapton hinges, PCB tiles, strain gauge sensors and low-profile SMA actuators, all combined in 2D to 3D fabrication process by lamination and folding assembly. The palm-sized, 6 g tethered robot crawls with closed-loop controlled steps and adjusts jumping height in open-loop by SMA actuator power modulation. Experimental results reveal the effectiveness, validity and versatility of the scheme for designing and prototyping origami robots with multiple functionality. The minimal, compact bending and snapping "gear-free" mechanism based on the Y-shaped compliant joint folded by the lightweight, customizable SMA actuators and sensors, demonstrates a great potential for building multi-functional millirobots with minimal assembly steps.

This work is a crucial step toward a generalized robogami design tool by *computational making*, encouraging creativity in the field and pushing its boundaries. While we demonstrated some

generalized models for the folding actuators, the proposed formulation still lacks quantitative analysis of the design features to establish standard models for geometries, mechanisms and functional material components and their synergistic integration into a design tool as in Figure 3.13, one of our future directions. In this sense, a clear relation of the geometry, mechanisms and materials to generate versatile and up-to-task functionality is required, optimizing the design. Another objective is to develop multimaterial integrated fabrication methods for machining/printing of meso-scale robogamis and to standardize them for mass-manufacturing. The proposed design paradigm not only contributes to the robotic origami research community by bringing attention to the potential and challenges in the field, but also attracts researchers from diverse areas.

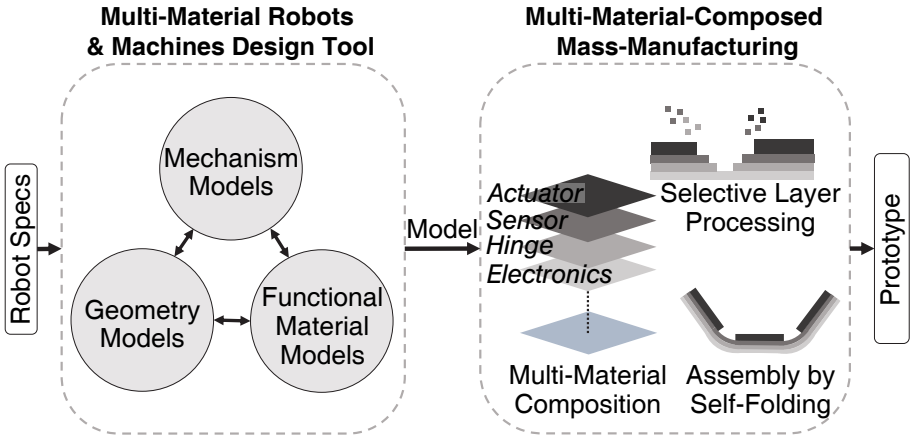


Figure 3.13 – Illustration of the grand goal for multimaterial-integrated rapid design and mass manufacturing of a new generation of intelligent robots and machines. This is possible by developments in both design and manufacturing technologies. The design requires quantitative formulation and generalization of the mathematical models for geometry, mechanisms, and functional materials in the first place, and their synergy to give an integrated system model, whereas mass manufacturing requires the development of new multimaterial integrated fabrication methods by selective layer processing of multi-layer stacks at meso-scale with minimized assembly effort.

# 4 Design of a Multi-Locomotion Mesoscale Robotic Collective

In this chapter, we demonstrate the capability of our design methodology for constructing *push button* mass-manufacturable origami robots with mechanisms, material and electronic layers readily-composed to produce untethered, self-contained, multifunctional *mechamatronic* robots. Here, we design the latest version of an autonomous, multi-locomotion millirobot Tribot, inspired by trap-jaw ants, that addresses the locomotion mechanism design and scalability challenges of small-scale terrestrial robots. We present a unique example of minimal, compact and tunable mechanism that generates five distinct locomotion gaits: height (vertical), distance (horizontal) and somersault jumping to clear obstacles, flic-flac walking on textured terrains and inchworm crawling on flat surfaces. The untethered, battery-powered millirobot can selectively switch gaits to transit diverse terrains and operate collectively to manipulate objects and overcome obstacles in tandem. We constructed the 10 g palm-sized prototype (see Figure 4.1), the smallest and lightest self-contained, multi-locomotion robot to date, by folding a quasi-2-D mechamatronic composite with locomotion mechanisms, smart actuation and sensing layers, enabling robot scalability by assembly-free mass-manufacturing.

The material presented in this chapter is adopted from the following publication:

**Zhakypov, Z.**, Mori, K., Hosoda, K. and Paik, J., 2019. Designing minimal and scalable insect-inspired multi-locomotion millirobots. Nature, 571(7765), pp.381-386.

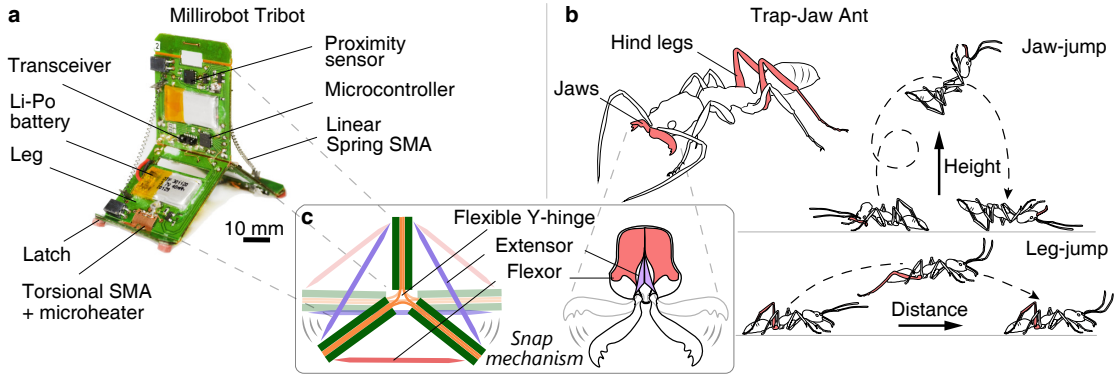


Figure 4.1 – **Tribot millirobot trap-jaw ant-inspired multi-locomotion mechanism design.** **a**, the untethered millirobot Tribot with Y flexure hinge powered by linear spring SMA actuators. **b**, the trap-jaw ant, which uses both mandible snap and hind legs for jumping. **c**, The Y-hinge that connects the three legs snaps-through when compressed uni-axially with high force and bends at low forces and angles less than 180°.

## 4.1 Challenges of Scalable Design

In ant colonies, collectivity enables division of labor and resources[145, 146, 147] with great scalability. Beyond intricate social behaviors, individuals of the genus *Odontomachus*[2], also known as trap-jaw ants, developed remarkable multi-locomotion mechanisms to “escape-jump” upward when threatened using instant snapping of mandibles[148] and leap forward employing their legs[1] to negotiate obstacles (Figure 4.1). Creating this ability in small-scale robotic systems with design simplicity and scalability remains a significant challenge that will allow emulating diverse insect biomechanics, studying collective behaviors in uneven environments and their deployment toward emergency relief, exploration and monitoring[5] with high task efficiency and flexibility. Existing robotic collectives[149, 6, 150, 151, 152], however, are confined to 2-D surfaces, whereas the individual battery-powered multi-locomotion robots[50, 51, 52, 53, 54] are difficult to scale up due to increased complexity, size and cost of hardware designs that hinder mass production.

The unique, integrated jaw bite-jump and leg walk-jump multi-locomotion mechanisms evolved in trap-jaw ants are vital for traversing obstacles orders of magnitude larger than their miniature bodies, covering large areas in search for food, predation while escaping predators[3] (Figure 4.2). However, such highly complex design nature of trap-jaw individuals is not an issue for scaling up their colony as they can continuously reproduce by "queen factories". Engineering the ability of negotiating diverse terrains at meso-scale yet with design scalability remains a significant challenge for locomotion mechanisms hardware design[14]. The locomotion strategies, like jumping, necessitate high mechanical power[15] to achieve high take-off velocity, whereas walking requires relatively low power and combining them into a compact robotic body with minimal, yet tunable power mechanism suitable for mass manufacturing is difficult. Existing small-scale multi-locomotion robots[50, 51, 52, 53, 54]

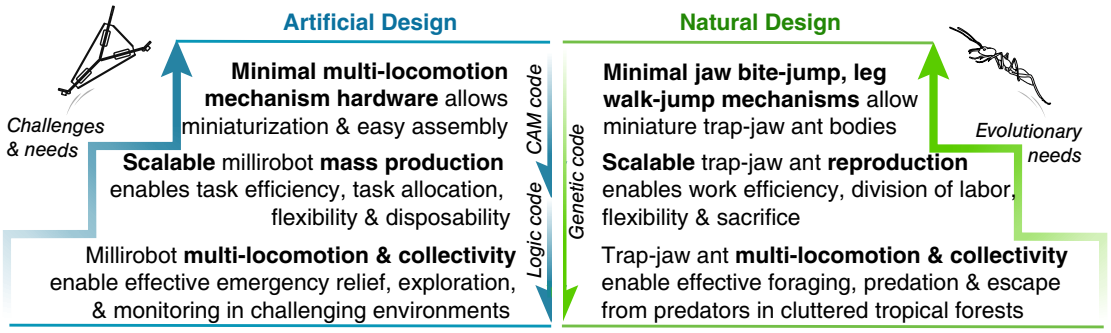


Figure 4.2 – **Design challenges and needs of natural vs artificial multi-locomotion collectives.** Trap-jaw ant collectivity backed by scalable reproduction and minimal multi-locomotion mechanisms integrated into their jaws and legs are the key to their survival in cluttered environments, designed by evolutionary process. Creating these abilities in engineered systems will enable applications, such as emergency mitigation, environmental monitoring and exploration with high task flexibility and efficiency. However, constructing minimal, integrated multi-locomotion mechanisms remains as a significant challenge for robotic hardware design that, when addressed, enables robot miniaturization and assembly-free mass production for collective implementations.

possess individual mechanisms per locomotion gait with increased gear trains, joints and links, which makes manufacturing difficult, or require external electromagnetic actuation[8, 153]. Neither of the approaches offers a compact, scalable, and autonomous multi-locomotion robot platform with capabilities for collective application.

Hardware complexity due to multifunctionality and mass-production is contradictory in terms of design, cost and time. Mass manufacturing is only possible by standardizing and automating the design and fabrication processes with minimum intervention. This necessitates robot minimal design without deteriorating multifunctionality, hence, manufacturing is a critical part of design process that supports our design paradigm presented in Figure 4 and methodology in Figure 3.1. Such design for manufacturing approach will allow rapid "reproduction" of robots by robots with high consistency and often using raw materials efficiently, which remains as an open scientific question.

## 4.2 Tribot Multi-Locomotion Mechanisms Design

To address the challenges desribed earlier, we design the next generation of a multi-locomotion origami millirobot Tribot in Figure 4.1a that addresses the multi-terrain mobility and scalability challenges of millirobots using a single yet versatile locomotion mechanism. To leap and clear obstacles, we designed a snap-through mechanism similar to the trap-jaw ant's mandibles (Figure 4.1b) by constructing a three-legged robot with Y-shaped flexure hinge at the center and opening and instant closing the legs by selective activation of three linear spring shape memory alloy (SMA) muscle-actuators. When the Y-flexure hinge is opened by a pair of extensor SMA actuators to an angle slightly above 180° on any three sides and compressed

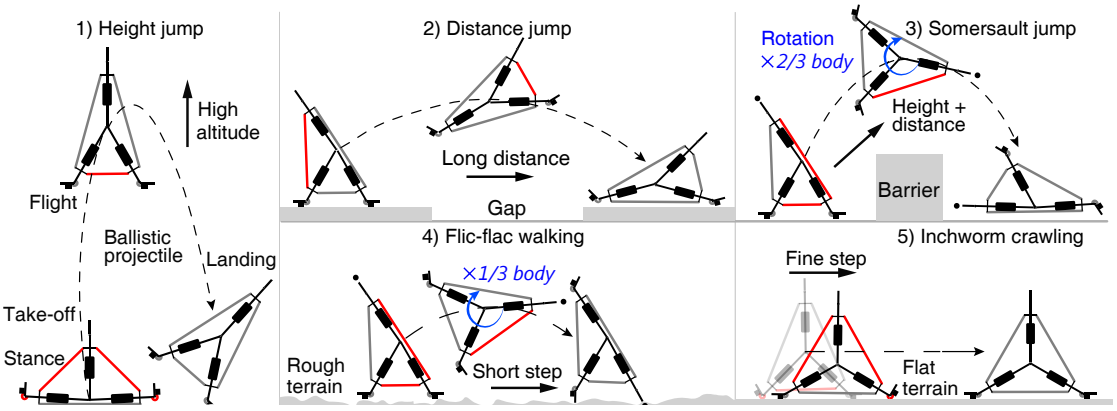


Figure 4.3 – **Tribot millirobot multi-locomotion mechanism design.** Selective snapping and bending of the Y-hinge by activating (red) spring and torsional SMA actuators generates five locomotion gaits: height jump (jaw-jump), distance jump (leg-jump), somersault jump by flipping in the air, flic-flac walking and inchworm crawling.

uni-axially by a flexor SMA, it experiences instability and snaps-through to the side of the applied compressive force with variable speed proportional to the applied force (Figure 4.1c). If the snap occurs at the hinge bottom, Tribot leaps vertically upward in a height jump, similar to jaw-jump, if it is at any of the two hinge sides, the robot leaps horizontally in a distance jump, like a leg-jump, beneficial for striding across gaps, or combines both in a somersault jump for clearing barrier obstacles as depicted in Figure 4.3. In the latter, the bottom SMA activates shortly before triggering the side SMA that snaps the mechanism, so the robot leaps both vertically and horizontally in the air while flipping before landing.

To enable the robot walking with periodic short steps over textured terrains employing the same mechanism, we developed a “flic-flac” locomotion strategy similar to Moroccan spiders[4]. Here, the actuator activation sequence is the same as for somersault jump; however, the compression of trigger SMA occurs at low power so the robot slightly hops and flips onto its two consecutive legs as in Figure 4.3. This maneuver is producible multiple times at any robot edge. Then to achieve propagation with fine steps on flat terrain, we incorporated “inchworm-like” crawling strategy. We utilized the continuous bending ability of the Y-hinge at three sides combined with stick-slip rubber latches that grip and release the ground contact. We embedded two torsional-sheet SMA actuators[78] with micro-heater layers into the latch folds to produce controllable crawling in both directions.

### 4.2.1 Multi-Locomotion Analysis

The snap-through and bending properties of the central compliant Y-hinge (Fig. 1d), along with the appropriate arrangement of the robot legs and latches by selective activation of the SMA actuators, generate height, distance, somersault jumping, walking, or crawling gaits shown in Figure 4.3. For a robot with autonomy, this can be programmed on the onboard

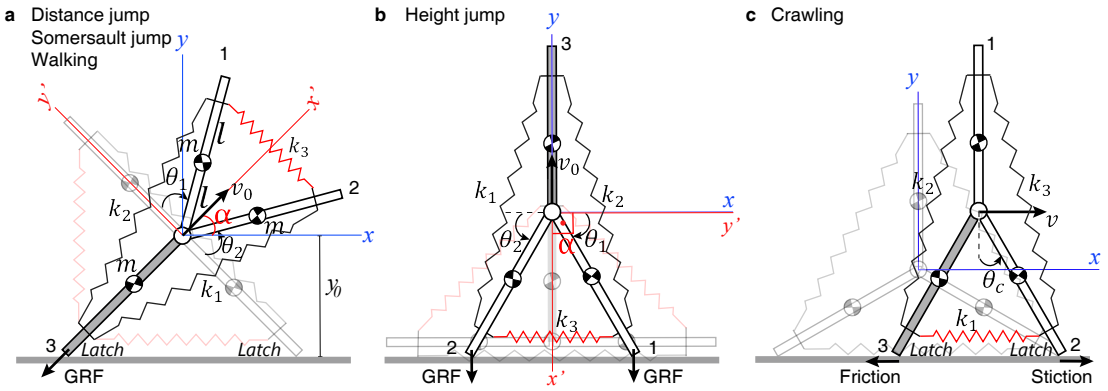


Figure 4.4 – **Tribot locomotion mechanisms free-body diagram. a**, Tribot transitioning from a stance to take-off phases applicable for distance, somersault jumping and walking gaits as a result of snap-through at the Y-hinge side. Y-hinge is modeled as a revolute pin-joint connecting three links. The snap-through motion generated by compression of the side SMA spring actuator ($k_3$) rotates side legs (1 and 2) instantly and pushes the rear leg (3) against the ground. This produces a ground reaction force (GRF) that lifts the robot in ballistic projectile with the take-off velocity $v_0$. For somersault jumping, the bottom spring actuator ($k_1$) activates shortly before the side spring ($k_3$) to achieve free body rotation in flight phase. The robot can perform height jumps on any three edges; however, for reaching high altitudes, it is the most effective on the edge without friction latches (1 and 2). Here, the snap-through occurs at the Y-hinge bottom, so the rapid closing of bottom legs produce GRF that lifts the robot up vertically as in **b**. The crawling locomotion is done on the edge with latches and the robot moves by opening and closing the bottom legs (2 and 3) and stick-slip arrangement of the latches as in **c**.

microcontroller, or controlled remotely via a keyboard on a portable computer by setting the actuator activation sequence, duration and power through a custom graphical user interface. For height, distance, somersault jumping and walking, the activation pattern of the actuators (on-red, off-gray) transits the robot from an initial rest state to stance and then to take-off phases, while there is no activation presents at flight and landing phases. The robot follows a ballistic projectile for all four maneuvers after take-off with different launch angle, velocity and body rotation during flight.

We modeled the Y-hinge as a pin-joint, which connects three independently rotating legs as in the robot free-body diagram illustrated in Figure 4.4. For distance jumping, somersault and walking, the snap-through motion at Y-hinge side shuts two side legs instantly that push the third rear leg against the ground at angle $\alpha$, so the ground reaction force (GRF) lifts the robot in the air (Figure 4.4a). For height jumping, the snap-through of the Y-hinge bottom rapidly closes two bottom legs against the ground that in turn produce GRF to launch the robot up vertically (Figure 4.4b). The kinematics of the robot flight in x-y Cartesian coordinates between

take-off and landing (first touchdown) is governed by a ballistic projectile motion given by

$$y = y_0 + x\tan\alpha - \frac{g x^2}{2v_0^2\cos^2\alpha} \tag{4.1}$$

where $y_0$ is the initial height of the robot considered between the center of Y-hinge and the ground at instant of take-off, $\alpha$ and $v_0$ are the launch angle and velocity, respectively, and g is the gravitational acceleration. We omit the air-drag due to high uncertainty in predicting the surface area of the robot for each gait, especially for somersault jumping and walking due to free body rotation. The maximum travel distance in horizontal d and vertical h axis are then calculated by

$$h = \frac{v_0^2\sin^2\alpha}{2g}, \quad d = \frac{v_0^2\sin 2\alpha}{g} \tag{4.2}$$

The robot jumping displacement is maximized by increasing $v_0$ and adjusting $\alpha = pi/2$ for height jumps and $\alpha = pi/4$ for distance, somersault jumping and walking. While Tribot does not considerably rotate when performing height and distance jumps, at least during ascend, it rotates 2/3 times its body on average for somersault jumping and 1/3 for walking.

For crawling locomotion, the robot contacts the ground with latches and the activation sequence of the linear and torsional actuators produce a periodic stick-slip motion (Figure 4.4c). Here, the torsional SMA actuators raise rubber pads to slip and drop to stick, discretely varying the contact friction. The crawling step is then calculated by

$$c = 4l(\sin\theta_0 - \sin\theta_c) \tag{4.3}$$

where $c$ is the crawling step size for a single stick-slip maneuver, $l$ is the leg half length, $\theta_o$ and $\theta_c$ are the opening and closing angles between the bottom two legs, respectively.

To set a generalized robot multi-locomotion dynamic model and to identify the effect of the robot parameters on its velocity for each gait, we adopted Euler-Lagrange method. Employing Newtonian ($F = ma$) approach is difficult for modeling not only multi-locomotion, multi-DoF mechanisms, but also single locomotion mechanisms. The energy-based nature of the Euler-Lagrange method provides close insight into the locomotion mechanism performance in terms of stored energy and produced motion, and, therefore, enables design optimization of system components responsible for motion. The total kinetic and potential energy of the

robot are given by

$$T = \frac{1}{2}\sum_{i=1}^{3} m_i v_i^2 + \frac{1}{2}\sum_{i=1}^{3} J_i w_i^2, \quad V = \sum_{i=1}^{3} m_i g h_i + \frac{1}{2}\sum_{i=1}^{3} k_i s_i^2 \tag{4.4}$$

Here, $m_i$, $J_i$, $v_i$, $w_i$ and $h_i$ are the mass, moment of inertia, Cartesian and angular velocities, and height of $i$-th link, respectively. $k_i$ and $s_i$ are the stiffness coefficient and deflection of $i$-th spring SMA actuator (Figure 4.4). The Lagrangian function is then calculated by $L = T - V$, and since the high speed (snap-through), or low speed (bending) rotation of two links produce all five gaits, then the equations of motion $\begin{bmatrix} \ddot{\theta}_1 \\ \ddot{\theta}_2 \end{bmatrix}$ can be computed by solving

$$\frac{\mathrm{d}}{\mathrm{d}t}\left(\frac{\partial L}{\partial \dot{\theta}}\right) - \frac{\partial L}{\partial \theta} = 0 \tag{4.5}$$

While the masses and moments of inertia of all three links in Equation 4.4 are assumed to be equal and constant, it is the spring SMA stiffness coefficients $k_i$ that define stored energy and, therefore, decide the link moving speeds when released at snap-through. For our robot, the stiffness balance is set as $k_1 + k_2 > k_3$ then $k_3 > k_1 + k_2$ to generate snap-through for jumping and walking gaits, and $k_1 > k_2 + k_3$ then $k_2 + k_3 > k_1$ for crawling. These actuator parameters are not only tailored at design, but also controllable between the martensitic and austenitic temperatures during operation by changing the input electric power that varies the SMA material temperature, hence stiffness[32] (see Appendix).

As Tribot structure necessitates different configuration and orientation for each locomotion, we defined a local coordinate frame ($x' - y'$) and global coordinate frame ($x - y$), which relate by a $2 \times 2$ rotation matrix and angle $\alpha$ (Figure 4.4). As the position of the robot's center of mass significantly varies between the stance and take-off states, we fixed the origins for both coordinate systems at the center of Y-hinge. Then the positions, translational velocity and acceleration of the link 1 and link 2 are calculated by

$$p_i = \begin{bmatrix} x_i \\ y_i \end{bmatrix} = \begin{bmatrix} l(\sin(\theta_i + \alpha) - \sin\alpha) \\ -l(\cos(\theta_i + \alpha) - \cos\alpha) \end{bmatrix}, \quad i = 1,2 \tag{4.6}$$

$$v_i = \sqrt{\dot{x_i}^2 + \dot{y_i}^2} = l\dot{\theta}_i, \quad i = 1,2 \tag{4.7}$$

$$a_i = l\ddot{\theta}_i, \quad i = 1,2 \tag{4.8}$$

For height and distance jumping $\theta_1 \approx \theta_2$ and for somersault jumping and walking $\theta_1 > \theta_2$ due to short activation of bottom spring SMA actuator before the snap-through that limits the angular rotation of link 2. The overall robot velocity is then a sum of individual link velocities

$$m_r v = m \sum_{i=1}^{2} v_i \tag{4.9}$$

Here, $m_r$ and $v = v_0$ are the robot mass and velocity. The total actuation power P required to accelerate Tribot to distance $\Delta p$ between the stance and take-off positions can be calculated using

$$P = \frac{KE}{\Delta p} v = \frac{m_r v^3}{2\Delta p} \tag{4.10}$$

where $KE$ is the robot's kinetic energy. We can also calculate the cost of transport (COT) for each locomotion by

$$COT = \frac{KE}{m_r r} = \frac{v^2}{2r} \tag{4.11}$$

Here, COT is in $J.kg^{-1}m^{-1}$ and $r$ is the total travel distance, corresponding to $h$ for the height jump, $d$ for distance, somersault jumping and walking, and $c$ for crawling locomotion. COT is an important metric for identifying energy efficiency, especially of terrestrial locomotion, and benchmarking across different mobile robots and organisms.

### 4.2.2 Actuation Design

The latest version of Tribot has similar geometry as previous designs, however, we combined the energy storing capability of spring coil SMA actuators at the legs and low power consumption of torsional sheet actuators on the latch joints to produce locomotion on any three sides. The aforementioned locomotion mechanisms are produced by compressing and storing energy in the three spring SMA actuators that are Joule heated by passing direct current, whereas the two torsional sheet SMA actuators are activated by thermal conduction of heat generated

by the micro-heaters. To enable a fully automatic, as well as a remotely controlled activation of the actuators, yet with tunable power, we employed a pulse-width-modulation (PWM) method. We adjust the average electrical power $P_{avg}$ flow to each actuator by controlling the switching duration $0 \leq duty \leq 1$ of five MOSFETs in the software as $P_{avg} = duty \times P_s$. The supply power is governed by Kirchhoff's rule $P_s = V_s^2 / R_{SMA}$ , where $V_s$ is the battery supply voltage and $R_{SMA}$ is the electrical resistance of spring SMA, or torsional SMA micro-heater. In reality, electrical resistance of Nitinol material slightly increases with temperature, however, we fix it to 2.2 Ω, which is measured at room temperature (martensite) and 7 Ω for torsional SMA micro-heater.

The SMA actuators also stiffen proportionally to the applied heat between the martensite (cold) and austenite (hot) temperatures as described in Chapter 2 Equation 2.1. The compression force also increases significantly with increasing the wire diameter, however, it requires higher currents to heat the wire due to reduced resistance. This is an important trade-off in designing the actuators to generate sufficient force at low power for untethered applications. For our spring SMA actuators, we designed $d$=0.25 mm, $D$=0.9 mm, $N$=32-33, $G_A \approx$18 GPa and $G_M \approx$7 GPa to operate without an external power supply. The torsional sheet SMA actuators[78] bending moment is governed by Equation 2.4. The dimensions of SMA sheet are designed as $t$=0.1 mm, $w$=8 mm, $L$=14 mm, $E_A \approx$34 GPa and $E_M \approx$19 GPa. The external heater layer composes of Kapton-backed copper laminate thin as 0.05 mm.

## 4.3 2D Fabrication

To achieve millirobot scalability for collective applications, we combined the automated manufacturability of printed circuit assembly (PCA) process and the flexibility of SCM design [20] to facilitate integrated robot construction with mechanical, material and electronic layers by processing them in 2-D, laminating layer-by-layer and assembling into 3-D by folding [32, 28], as depicted in Figure 4.5. While the PCB layer serves as structural backing and for embedding autonomy with off-the-shelf electronics, including a microcontroller, distance and communication sensors and rechargeable batteries, the polyimide (Kapton) layer forms the flexure hinges. The integrated design of actuators, mechanisms and surface mount electronics enables robot miniaturization; however, for the current version, the off-the-shelf battery capacity was the major factor defining its size, occupying almost 50 % of body surface and 40 % of the body mass (see Table 4.1).

In our design, we use off-the-shelf components and the total cost of the robot is under 60 $ (USD). It takes approximately three hours for a skillful person to fabricate and manually assemble the robot. However, we could substantially improve this by automated PCA mass-production process. Our method allows processing of a wide range of materials with extremely fine features and greatly reduces assembly effort, leveraging low-cost and on-demand push button manufacturing of millirobots.

Tribot's body consists of two structural layers: a 300 µm-thick double-sided FR-4 PCB for

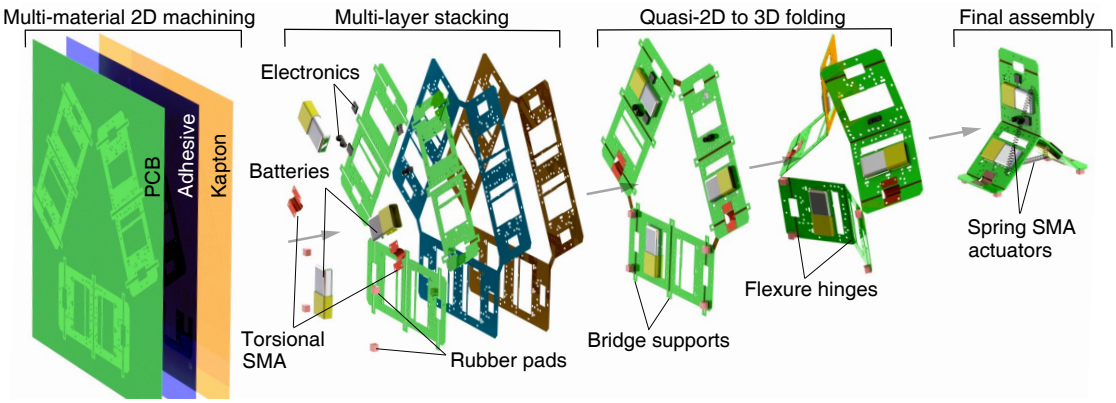


Figure 4.5 – **Tribot millirobot mechamatronic, multi-layer 2-D rapid fabrication and folding assembly process.** The PCB and Kapton layers serve as the structural support and compliant hinges, respectively and are stacked by an adhesive layer and heat press. Then, a stencil mask is placed on the PCB face and footprints are filled with solder paste. The stencil is removed, the electronic components then placed onto the footprints and the circuit placed on a heat plate for reflow. After, batteries, latch rubber pads and torsional SMA actuators are attached and the bridge supports are removed for fold ability of hinges. Finally, the multi-layer sandwich is folded along the hinges to obtain Tribot's 3-D structure, spring actuators, wires are installed and the robot is programmed and tested.

structural backing and electronics and a 50 µm-thick Kapton polyimide film (DuPont) for hinges, being flexible and durable. The EPFL PCB workshop mass-produced the PCB layer and the Kapton is cut on a laser micro-machining station (LAB 3550, Inno6, Inc.). The two layers are bonded together by an adhesive film (Poli-Melt 701, Poli-Tape Group) and heat pressed (Carver 3853CE, Carver, Inc.) for two minutes at 160 ºC with 90 N pressure. Then, to attach the electronic components, we applied a solder paste (SMD291AX, Chip Quick, Inc.) onto the 100 µm-thick Kapton stencil, placed on top of the PCB using a spatula, filling the component footprints. The stencil is gently removed and then surface-mount device (SMD) components, including two infrared (IR) proximity sensors (VCNL4010, Vishay), two IR transceivers (TFBS4711-TT1, Vishay) for communication, a microcontroller (ATTINY4313-MU, Atmel), connectors and switches among 50 other electronic components, are manually pick-placed onto the footprints. We then place the PCB sheet for three minutes on a hot plate at 200 ºC for solder reflow. Then, three 3.7 V, 40 mAh rechargeable Li-Po batteries (DTP301120, Datapower) are soldered onto the terminals, two torsional SMA actuators with attached micro heaters and four rectangular pads of 3 mm size, molded from silicone rubber (Elastocil M4601, Wacker Chemie AG) are glued onto the two latches. After cutting off the support bridges across the PCB hinge gaps (Figure 4.5), the multi-layer sheet is folded to pop-up to the robot's three-legged 3-D structure. Finally, we solder a few wires electrically connecting one leg to the other, install the spring SMA actuators and test the assembled robot.

Table 4.1 – Tribot Funcitonal Layers and Mass Budget

| Component/Layer | Material | Quantity | Mass (g) |
|---|---|---|---|
| Rigid Legs | Fiberglass-Copper | 1 | 3.1 |
| Compliant Hinge | Polyimide | 1 | 0.49 |
| SMA Actuators | Nitinol | 5 | 0.35 |
| Latch Friction Pads | Elastocil | 4 | 0.5 |
| Electronics and Wires | Silicon, Copper | >50 | 1.56 |
| Batteries | Lithium-Polymer | 3 | 3.7 |
| **Robot Total** | | | **9.7** |

## 4.4 Locomotion Performance

To validate the efficacy and repeatability of Tribot's locomotion gaits, we conducted twelve original locomotion experiments: eleven independent gait tasks (height, distance and somersault jumping, walking and crawling) each repeated six times at various terrain, power and loading conditions and a continuous parkour scenario with smooth, rough terrain and obstacle. We studied robot's motion by recording each experiment on camera at high frame rate (250 fps) for jumping and in real-time (25 fps) for walking and crawling gaits, and tracking the central Y-hinge employing a video analysis software. The further details of the experimental design and error analysis can be found in Appendix.

### 4.4.1 Jumping

We studied the robot's vertical leaping capacity by height jumps on two edges on a flat surface, with and without rubber latches as shown in Figure 4.6a. Tribot jumps as high as 140.6 mm on average, 2.5 times the size of body, on the edge without latches compared to 72.5 mm on the edge with latches for an equal trigger SMA electrical power of 3.7 W, due to the minimal friction during take-off (Figure 4.7). We studied the distance jumping with the trigger power of 3.7 W as in Figure 4.6b, 2.7 W and with added payload of 5 g, 50 % the robot's body mass, at 3.7 W. The average jumping distance was 230 mm, almost four times of the body size, 140 mm and 110 mm, respectively. The somersault jump gait was tested with the trigger power of 3.7 W and the average jumping height and distance were 88 mm and 100 mm, respectively, with average of 2/3 of body rotation around its central axis in the air.

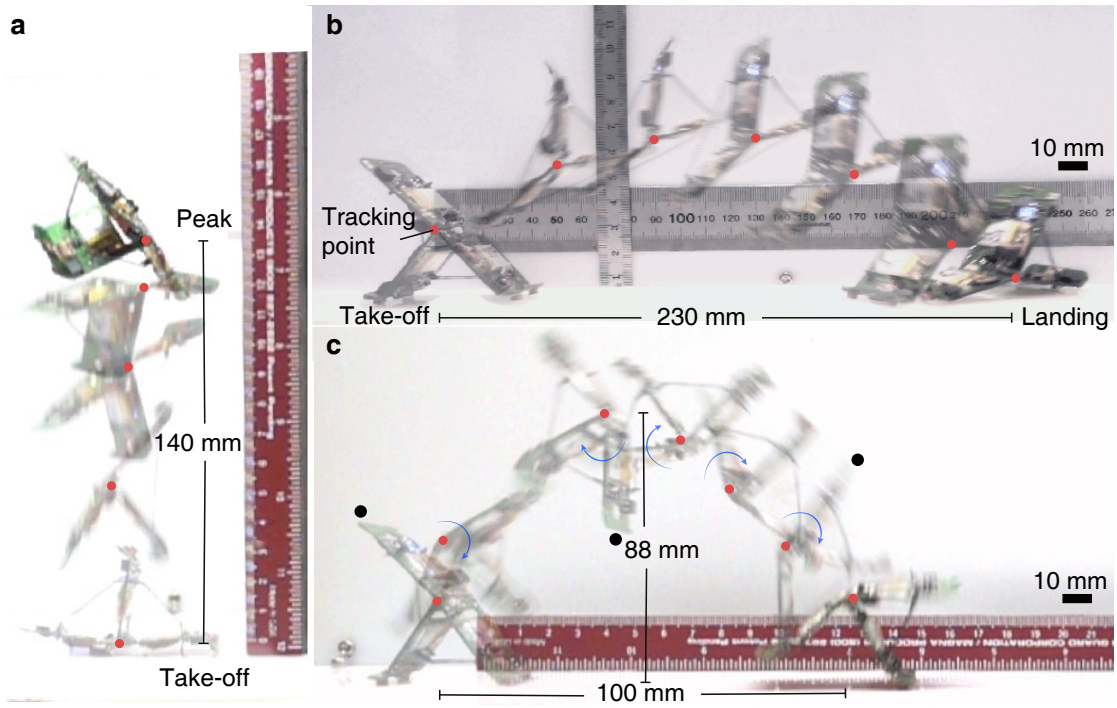


Figure 4.6 – **The snapshots of Tribot height, ditance and sommersault jumping.** **a**, Tribot is in height jump phase on no latch side from take-off to peak height. **b**, The robot in distance jump phase; from stance to landing positions. **c**, Tribot performing a somersault jump maneuver by rotating in the air before landing.

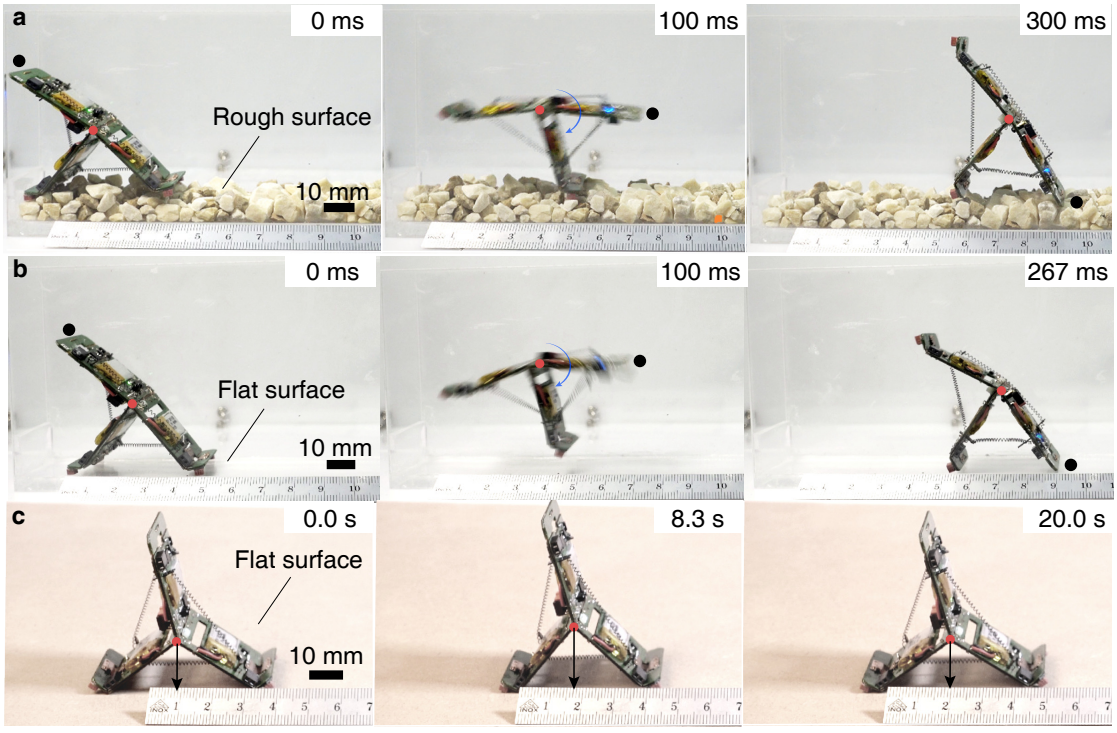


Figure 4.8 – **The snapshots of Tribot walking and crawling locomotion.** The robot performing a single flic-flac walking maneuver on rough with raisin-sized stones **a** and smooth flat surface without the stones **b**. **c**, the robot performing a single stick-slip inchworm crawling step on flat surface.

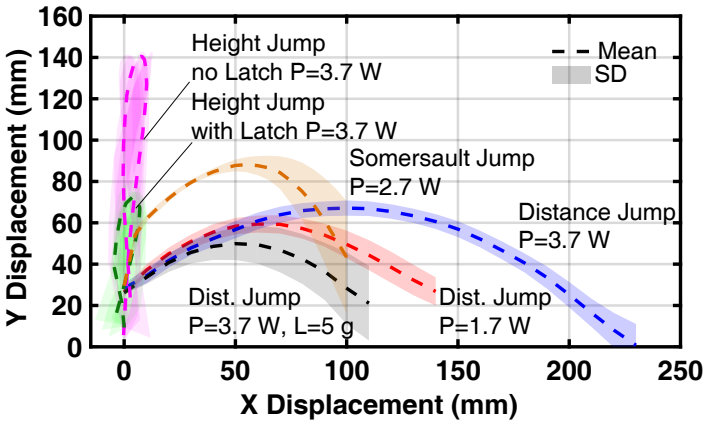


Figure 4.7 – **Tribot's travel projectiles for height, distance and somersault jumping.** The data is extracted from videos recorded at 250 fps. Each experiment is repeated six times to determine the mean (dashed lines) and standard deviation (shaded regions).

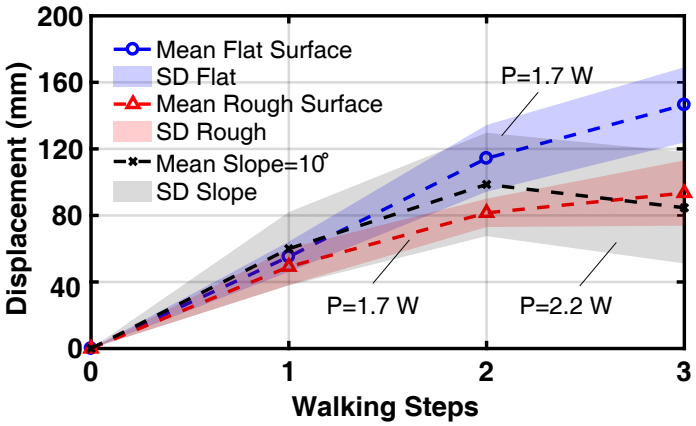


Figure 4.9 – The robot walking displacement per walking step on flat, rough and 10° flat slope for six runs. Tribot flips three times to return to the initial state.

### 4.4.2 Walking

To test the effectiveness of the walking gait on rough and flat surfaces and climbing up a flat slope of 10°, we remotely controlled Tribot to perform three flic-flac maneuvers on each terrain, arriving back on its initial edge. To confine the robot's deviation sideways, we placed it inside a transparent acrylic glass channel, slightly wider than its body, with (Figure 4.8a) and without (Figure 4.8b) raisin-sized stones on the floor. Tribot generates an average repeatable step of 48.8 mm on the flat surface with minimal 1.7 W trigger power (see Figure 4.9), while the steps on the textured surface were 31.1 mm, considerably smaller and not repeatable (Figure 4.9). This is likely due to minimal leg-ground contact with the textured surface, especially on the edges without latches, causing leg slippage with each rotation. The average step on the

slope was 28.8 mm and required about 30 % more power to flip.

### 4.4.3 Crawling

We validated the robot's crawling locomotion with fine steps on a flat surface as in Figure 4.8c and a 10º slope. The robot was programmed to execute six consecutive crawling steps and the average step size was 4.85 mm on flat surface and low as 2.61 mm for climbing the slope due to slippage (see Figure 4.10).

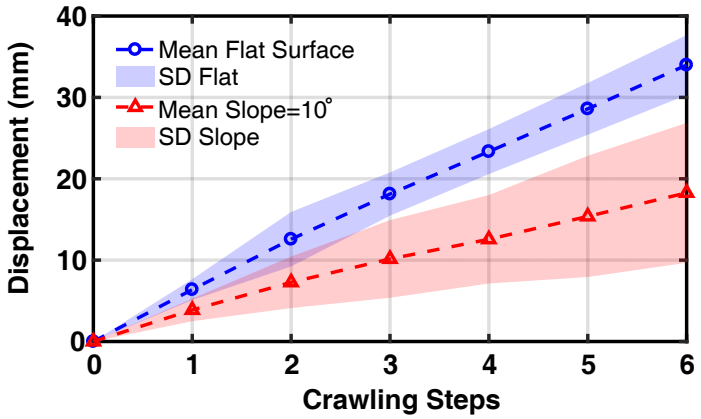


Figure 4.10 – **Tribot crawling displacement on flat surface and 10º slope.** The data is extracted from six consecutive crawling step cycles.

### 4.4.4 Cost of Transport

We assessed the generated power and cost of transport (COT) for all five gaits and compared Tribot's distance jumping COT to the existing small-scale multi-locomotion robots and insects as in Figure 4.11. Tribot is the smallest and lightest among the engineered systems and has significantly lower COT for distance jumps, comparable to the ones of trap-jaw ants [2], desert locust [11] and jumping spiders [12]. Tribot can distance jump as far as 230 mm on average with take-off velocity of 1.44 m/s. A more extensive comparison of multi-locomotion robots and insects in terms of mass, size, mechanisms among others is summarized in Appendix Table 4.2.

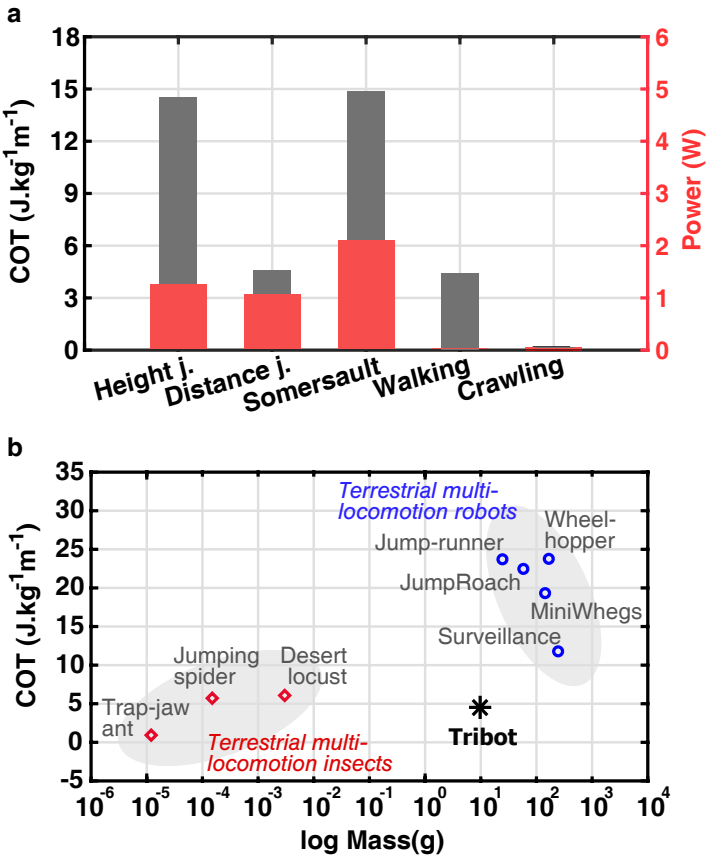


Figure 4.11 – **Tribot cost of transport compared to small scale multi-locomotion robots and insects.** **a**, the mechanical power output and cost of transport for five independent gaits. **b**, Tribot is smaller and lighter and has lower COT than the existing small-scale robots, comparable to those of insects.

### 4.4.5 Multi-Locomotion

To demonstrate the ability of multi-locomotion on diverse terrains, as well as against an obstacle, we set up a parkour experiment as depicted in Figure 4.12. Due to difficulty in predicting the locomotion maneuver outcomes on rough terrain, we controlled the walking and jumping phases remotely, while the crawling gait was pre-programmed. Tribot crawls through the smooth section until it reaches rough terrain, where it switches to walking gait and after four flips, arrives at the obstacle and jumps over. In this test, we observed discrepancy in the walking phase due to poor leg-ground contact that caused slippage and the robot landed once on the wrong edge. However, as walking is possible on any edge, the robot resumed the maneuver, demonstrating versatility.

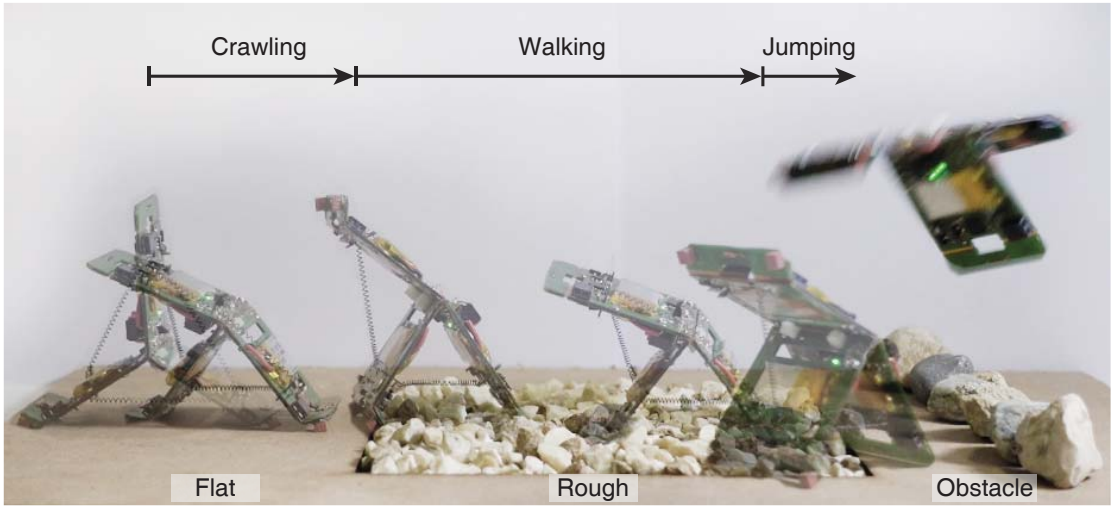


Figure 4.12 – **The demonstration of Tribot's gait adaptability on parkour setup with flat, rough terrain, and obstacle.** It crawls through the flat section, walks on the rough terrain and then jumps over the obstacle.

## 4.5 Collectivity

To display task efficacy in a scalable collective of multi-locomotion millirobots, we set up two experiments with division of labor and tandem running scenarios as in Figure 4.13, executed autonomously. The first task was to move a prismatic object to a set position that is light enough for two robots to push but not for one alone (Figure 4.13a). Such a simple task, however, requires assignation of five millirobots: two workers to push the object toward a monitor, who measures the relative closeness of the object by proximity sensor and informs the leader, who in turn coordinates the workers to push or stop. As the prism interrupts the local communication between the leader and monitor, it necessitates a messenger, who exchanges messages between the leader and monitor through an alternative route. The monitor robot's proximity measurement data shows that the object traveled from the 80 mm start proximity to the 50 mm set proximity (Figure 4.14a). This experiment demonstrates the significance of millirobot scalability for effectively allocating tasks, manipulating objects and resolving communication issues with limited resources.

To highlight the significance of robot multi-locomotion in collective tasks, we set up a unique tandem-running experiment with two robots, a leader and follower as in Figure 4.13b, performed autonomously. Both robots crawl in a line with fixed steps. The leader crawls and scans continuously for obstacles using its proximity sensor, while the follower only checks messages from the leader without energy expense for scanning. Both robots crawl until the leader detects an obstacle and conveys this to the follower (Figure 4.14b). We chose a relatively wide (40 mm) and deep (20 mm) gap as obstacle, which is crossable only by jumping over. We demonstrate that the leader, stuck at the gap edge and tilted forward, notifies the follower of the obstacle. Upon receiving the obstacle message, the follower measures its distance

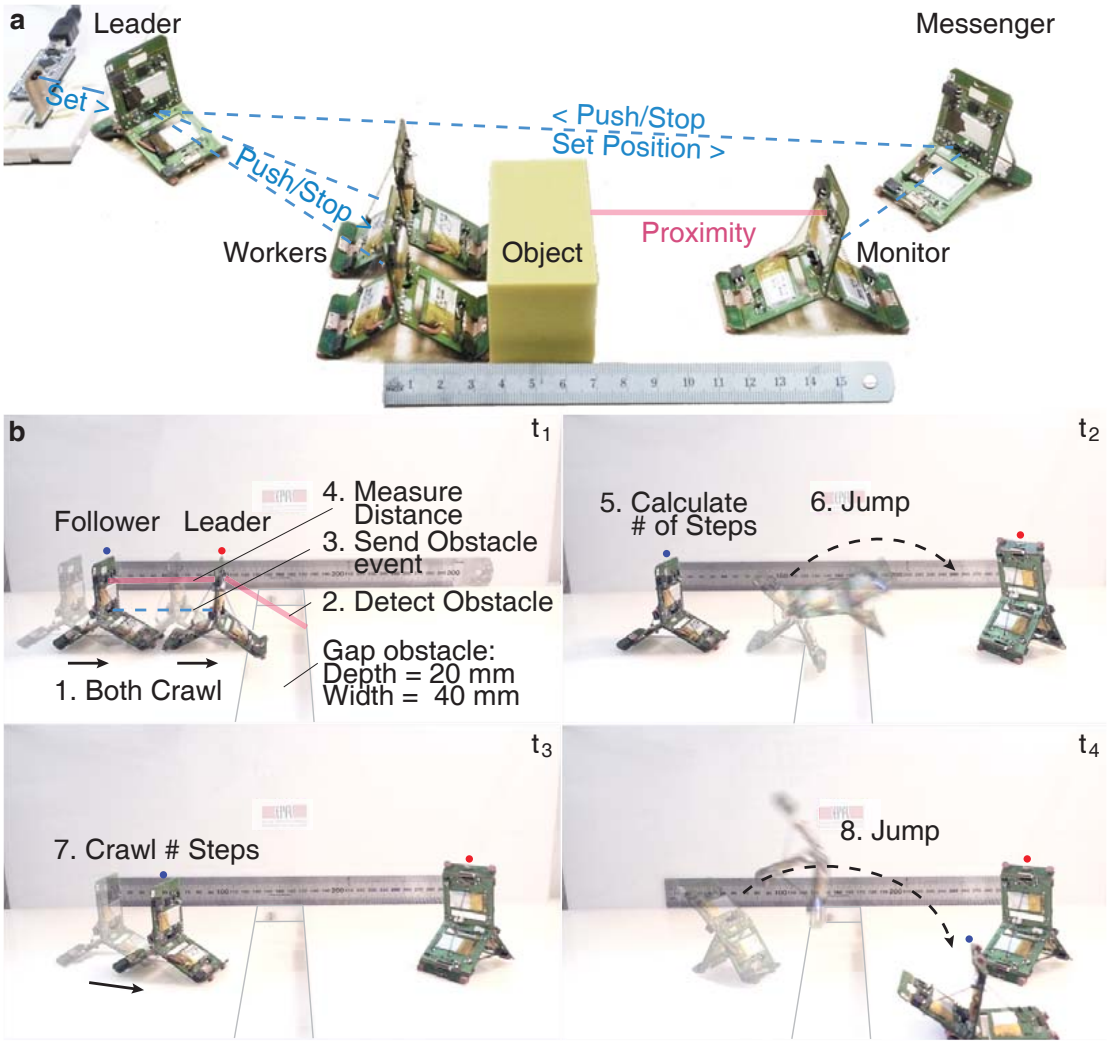


Figure 4.13 – **Two collective experiments with division of labor and tandem running. a**, the first task was to push an object to a desired position by coordination between the leader, workers, monitor and messenger robots. The leader orders two workers to push the object and the monitor measures the relative position of the object. As the object interrupts the two-way link between the leader and the monitor, the messenger maintains the communication. **b**, both robots crawl in a line until the leader detects the gap obstacle and informs the follower by sending a message. Unlike the leader, the follower does not search for obstacles, therefore saves energy. The leader jumps over the obstacle, while the follower measures the distance relative to the leader once and calculates the total number of steps to crawl to the obstacle before jumping. Both robots safely overcome the obstacle.

relative to the leader only once and then calculates the total number of steps to crawl by dividing the distance by the step size. Once transmitted, the leader jumps over the gap and then the follower crawls and jumps following its calculations without falling in. This signifies not only the expanded capabilities of multi-locomotion millirobot collectives, but also the

benefits of collectivity in negotiating obstacles, like allocating demanding tasks to a leader. Such "millirobot tandem running" can further promote collective teaching and learning about various terrains and obstacles to effectively plan locomotion.

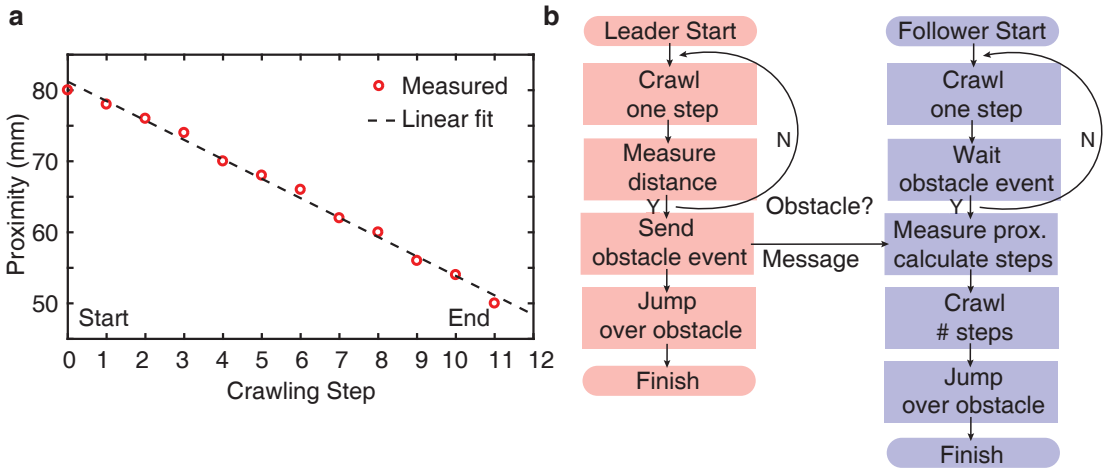


Figure 4.14 – **The proximity measurement data for division of labor experiment and event chart for the tandem running experiment. a**, the proximity data measured by the monitor robot that shows linear propagation of the workers with each pushing step and the object is moved a set distance of 30 mm. **b**, The event-chart for leader-follower tandem running experiment with obstacle avoidance by communication.

## 4.6 Experimental Design

To measure the robot's height, distance and somersault jumping trajectories, walking and crawling steps, we setup eleven different experimental scenarios. Each locomotion experiment is video recorded and analyzed using an open source scientific video tracking software, called Tracker (https://physlets.org/tracker/). As the robot leg snap-through motion occurs within a hundred millisecond, we employed a high frame rate camera (Sony Cyber-shot DSC-RX100 IV) with video recording speed of 250 fps, placed in front of the locomotion scene to capture robot displacement in x-y plane. The camera was configured to real-time (25 fps) video recording speed for walking, crawling and multi-locomotion parkour experiments. We located a ruler scale with SI units on the horizontal x and vertical y-axis to calibrate the captured videos that are then analyzed in Tracker. For all locomotion maneuvers, we tracked the robot's central Y-hinge in x-y Cartesian coordinates from the instant of take-off to flight and instant of landing (first touchdown). We performed eleven independent experiments for all five gaits, each ran six times and at each run, Tribot was brought to an initial stance position. As each experiment comprise twelve measured data sets of $x$ and $y$ positions with data points not aligned in neither of the axes, we interpolated each data set using Matlab pchip shape-preserving piecewise cubic interpolator function to align them in x coordinate to computed mean for each experiment. We also calculated the average standard deviations in y-axis by

taking the square root of the mean of variances (Extended Data Table 2). They are plotted as shaded regions in the locomotion plots employing Matlab fill function.

For height jumping experiments, the robot is tested on two different edges: side with latches contacting the ground and the side with no latch. The robot is controlled remotely for both experiments by keyboard with pre-set actuator activation power on GUI. For loaded distance jumping experiment, we mounted a 5 g M8 stainless steel hex nut at the robot rear leg. To evaluate the robot's walking step size, we placed it into a 22 mm wide channel made of transparent acrylic material to confine its lateral deviation while flipping. For testing on rough surface, we filled the channel floor with raisin-sized grains (FEPA F grain = F4 standard), while they were removed for the smooth surface test. To evaluate robot walking onto a slope, we placed the channel on an inclined flat medium-density fiberboard (MDF) with the slope of $10^o$.

To test the efficacy of robot crawling gait on different surfaces and onto a slope, we programmed the robot to crawl automatically with multiple steps on the edge with latches. We tested three terrain conditions: a sand paper with roughness P100 (FEPA standard), MDF with smooth finish positioned horizontally (slope=$0^o$) and inclined to $10^o$. As Tribot crawls by periodically applying friction on the surface with rubber pads and sliding with the torsional sheet SMA contact, their surface interaction was essential in defining the crawling performance. While we did not observe any horizontal propagation on sandpaper due to increased friction between SMA and sandpaper, the robot could crawl on the fiberboard with repeatable steps and even climb up a slope, however, with smaller steps due to sliding.

We computed COT for Tribot locomotion gaits and compared distance jumping COT to the multi-locomotion robots and insects employing take-off velocity, travel distance and mass data available in the associated literature, or extrapolated. This allows for effective benchmarking engineered and natural systems in terms of locomotion efficiency and performance.

## 4.7 Communication Range

Communication sensors enable Tribot to exchange information, interact and cooperate to execute collective tasks. Determining the sensor range helps to define the orientation and position of the next agent for a sustainable two-way (transmit-receive) communication link. The communication range of two IR transceivers placed on both sides of the robot's upper leg appear as two symmetric sectors with $60^o$ angular opening and the maximum range of 1 m. For two robots to establish two-way communication link, the maximum separation should not exceed 1 m and be within the sector with orientations that meet the conditions

$$\beta_1 - \frac{\pi}{6} + n\pi \leq \gamma \leq \beta_1 + \frac{\pi}{6} + n\pi, (n = ... - 1, 0, 1...) \tag{4.12}$$

$$\gamma - \frac{\pi}{6} + m\pi \leq \beta_2 \leq \gamma + \frac{\pi}{6} + m\pi, (m = ... - 1, 0, 1...) \tag{4.13}$$

where, $\beta_1$ and $\beta_2$ are the orientations of the first and the second robots on $x-z$ Cartesian coordinate plane, respectively, and $\gamma$ is the relative angle between two robots.

## 4.8 Conclusion and Discussion

We presented a new insect-scale origami robot that produces multi-locomotion with minimal and scalable design. This work motivates new investigations into a variety of insect bio-inspired and neuro-mechanics by employing a customizable, yet mass-producible hardware platform. The presented implementations leverage new research studies into the effect of multi-locomotion ability on collective behaviors of social insects, their colony size and task distribution that in turn will stimulate development of algorithms for large-scale physical systems with expanded capabilities. While the current version of the hardware has limited maneuverability, sensing and computational capacity, it still demonstrates applicability to real-world problems, such as emergency mitigation, environmental monitoring and exploration. Therefore, we aim to investigate comprehensive design methods and automated fabrication processes further to enable on-demand, push-button-manufactured robots and mechanisms accessible to diverse research community.

Table 4.2 – Comparison of Tribot with Small-Scale Terrestrial Multi-Locomotion Robots and Insects. h: height, d: distance, s: somersault, w: walking, c: crawling, esc.: escape and def.:defense

| **Robot / Insect Name** | **Mass (g)** | **Size (mm)** | **Number of Locomotion** | **Mechanisms & Actuation** | **Jump h./ Size** | **Jump d./ Size** | **COT** $\frac{J}{kg.m}$ |
|---|---|---|---|---|---|---|---|
| JumpRoach [50] | 59.4 | 100 | 2, running, jumping | 6 rubber bands, 1 four-bar linkages, 3 gears, 3 DC motors | 11 | 7 | h:9.7 d:22.4 |
| MSU Jump-Runner [51] | 25 | 90 | 2, running, jumping | 2 elastic strips, 1 slider-crank-cable, 8 gears, 2 DC motors | 16 | 6.6 | h:9.8 d:23.6 |
| MiniWhegs [53] | 146 | 90 | 2, running, jumping | 1 steel spring, 2 four-bar linkage legs, 2 chains, 2 motors, 4 whegs | 2.4 | 1.2 | h:10.5 d:19.3 |
| Surveillance Robot [54] | 250 | 140 | 2, rolling, jumping | 1 steel spring, 1 six-bar linkage, 4 gears, 3 DC motors, 2 wheels | 2.9 | 2.9 | h:11.7 d:11.7 |
| Wheel-Hopper [52] | 170 | 168 | 2, rolling, jumping | 1 steel spring, 2 four-bar linkages, 4 gears, 3 DC motors, 2 wheels | 0.7 | 0.3 | h:10.7 d:23.7 |
| *Desert Locust* [11] | *3* | *60* | *3, leg-jump, walking, flying* | *Leg flexor-extensor muscles* | *9.8* | *10* | *h:6.2 d:6.1* |
| *Jumping Spider* [12] | *0.15* | *15* | *2, leg-jump, walking* | *Leg flexor-extensor muscles* | *0.3* | *4.0* | *h:69.8 d:5.7* |
| *Trap-Jaw Ant* [2] | *0.01* | *13* | *3, jaw-jump, leg-jump, walking* | *Jaw snap leg catapult muscles* | *5.6 esc. 2.4 def.* | *2.4 esc. 17.2 def.* | *h:0.4 d:0.9 esc.* |
| **Tribot** | **9.7** | **58** | **5, height jump, distance jump, somersault jump, walking, crawling** | **3 SMA springs & 2 SMA sheet, 3 tree linkage legs, 1 snap/bend Y compliant hinge, 2 rubber latches** | **2.4** | **4.0** | **h:14.4 d:4.5 s:14.8 w:4.4 c:<1** |

# 5 Conclusion and Contribution

In this thesis we studied, developed and demonstrated multifunctional multi-robot systems in mesoscale. To achieve this, our first research objective was to develop, evaluate and demonstrate minimal, compact, variable power and efficient actuators and mechanisms employing functional materials, such as SMA and fluid, and their composites. Our second research objective was to develop a comprehensive and systematic design methodology for multi-layer multimaterial composite robots targeting robot multifunctionality, mass-producibility and miniaturization all together. These two state of the art studies on actuation and composite robot design methodologies are then consolidated and demonstrated by a multi-locomotion, mesoscale robotic platform called Tribot, to study both locomotion and collective behaviours similar to natural systems.

During my PhD studies, I developed and studied the following unique, state of the art prototypes:

- Five generations of multi-locomotion origami mesoscale robot Tribot;
- Origami-inspired reconfigurable suction gripper for picking objects with variable shape and size;
- Three compact SMA-based linear and bending actuators and a fluid-driven actuator.

## 5.1 Contribution Statement

My PhD dissertation explored and contributed by seeking answers to the following key research questions:

***How to achieve variable power, efficient and compact actuation in mesoscale?*** I explored and developed unconventional, synthetic, active material-based actuation methods using SMA and composite material to achieve four novel actuation methods: *high power and high speed actuation with helical spring SMA actuators, high torque and power efficient actuation*

*with bending sheet SMA actuators, easy inlaying and minimally assembled actuation with linear flat spring SMA actuators, and high speed distributed actuation with bending vacuum-powered actuation.* I investigated compromises between force, speed, efficiency and size of SMA material. I studied and demonstrated new, compact multimaterial actuators and mechanisms that possess power density superior to conventional motors, produce high speed and high force actuation and achieve multifunctionality when distributed and actuated selectively, all with minimal and compact forms and easy integration. I studied and developed a generalized design methodology for SMA actuators. The key findings of my research led to several research publications and contributed to the field by presenting a variety of actuation methods for mesoscale robots:

- **Zhakypov, Z.**, Falahi, M., Shah, M., and Paik, J. The design and control of the multi-modal locomotion origami robot, Tribot, IEEE IROS, pp. 4349-4355, 2015.
- **Zhakypov, Z.**, Belke, C.H., and Paik, J. Tribot: A deployable, self-righting and multi-locomotive origami robot. IEEE IROS, pp. 5580-5586, 2017.
- **Zhakypov, Z.**, Huang, J.L. and Paik, J. A novel torsional shape memory alloy actuator: Modeling, characterization, and control. IEEE Robotics and Automation Magazine, 23(3), pp.65-74, 2016.
- **Zhakypov, Z.**, Heremans, F., Billard, A. and Paik, J., An origami-inspired reconfigurable suction gripper for picking objects with variable shape and size. IEEE Robotics and Automation Letters, 3(4), pp.2894-2901, 2018.
- **Zhakypov, Z.**, Mete, M., Fiorentino, J. and Paik, J., Programmable Fluidic Networks Design for Robotic Origami Sequential Self-Folding. IEEE RoboSoft, pp. 814-820, 2019

***What, if any, is the general design methodology for constructing composite robots?*** Like with actuators, I studied and proposed a systemic design methodology for composite robot design. To achieve this I formulated and analyzed the robogami design in terms of *mechanisms, geometry, functional components, materials* and *fabrication* to highlight their relation, potential and the challenges, as well as to structure the knowledge in the field. I proposed a systematic design approach for composite robots that consolidates these critical design features and facilitates robot design process. I demonstrated the applicability of the methodology to the majority of reported mesoscale robotic systems and designed a jumping and crawling multi-locomotion mesoscale robot, called Tribot, that embeds minimal mechanisms and components for multifunctionality. This research work not only facilitates the design process of composite robots, but also promotes accessibility and development by filling gaps in the research field and invites potential contributors from diverse areas of research. The key findings of this work are published in the following manuscript:

- **Zhakypov, Z.**, and Paik, J., Design methodology for constructing multimaterial origami robots and machines. IEEE Transactions on Robotics, 34(1), pp.151-165, 2018.

This research can be thought of as an attempt to define qualitative, quantitative and experimental design schemes and aimed at establishing a backbone for future developments of composite robots. It requires further studies into the generalization of the method to enable computational methods to create a universal robogami design tool, encouraging creativity in the field and pushing its boundaries by including new methods and materials. In this sense, further extensive investigations into design generalization, quantitative analysis of the design features is necessary to establish standard models for geometries, mechanisms and functional material components and their synergistic integration. Another crucial direction is to improve multimaterial integrated fabrication techniques and methods for machining/printing of mesoscale robogamis and to standardize them for mass-manufacturing. Currently, discrete layer components are processed separately before composing, therefore, alternative approaches by selective laser processing of readily composed sheets should be closely studied to ensure minimal process intervention.

***How to achieve multifunctional multi-robot behaviors in mesoscale?*** I demonstrated the capability of the proposed actuation, mechanisms and robot composite design methods for constructing multifunctional multi-robot systems that display intricate physical and collective behaviors unexplored previously. In this sense, my final goal was to achieve the ability of multi-locomotion and mass-manufacturability of composite robots. I demonstrated this by constructing a unique, untethered, multi-locomotion robotic collective of Tribots to study multi-locomotion and cooperative behaviors. I investigated and developed a minimal, compact and tunable mechanism that generates high power jumping and low power crawling locomotion. I addressed the key trade-off between the actuation power and weight and constructed a 10 g palm-sized prototype, the smallest and lightest self-contained, multi-locomotion robot to date, by folding a quasi-2-D *mechamatronic* composite with locomotion mechanisms, smart actuation and sensing layers, enabling robot scalability by assembly-free mass-manufacturing. I demonstrated and experimentally validated a unique Tribot robotic platforms that operate in collective to manipulate objects and overcome obstacles together, addressing the locomotion limitations of existing robotic swarms with great scalability. My research and unique designs reach beyond the robotics research community to industrial production, computer science and biology. The presented implementations leverage new research studies into the effect of multi-locomotion ability on collective behaviors of social insects, their colony size and task distribution that in turn will stimulate development of algorithms for large-scale physical systems with expanded capabilities. The current version of the robot demonstrates applicability to real-world problems, such as emergency mitigation, environmental monitoring and exploration. The key findings of this research work led to the following publication:

- **Zhakypov, Z.**, Mori, K., Hosoda, K. and Paik, J., 2019. Designing minimal and scalable insect-inspired multi-locomotion millirobots. Nature, 571(7765), pp.381-386.

## 5.2 Future Implications

The future of manufacturing is digital and this can greatly expedite robogami design. Developments in machine learning, multimaterial printing and virtual reality will surely pave the way to efficient designs through simulation, physical creation and interaction, respectively. This would allow, a ten-years old school student to build and customize robots in class to learn engineering, biology and creativity all together through augmented reality by projecting different concepts onto the robotic platforms. Robogami designs, like Tribot, show full potential for scientists and engineers to recreate complex social and physical behaviours of natural systems realistically through tailored, scalable robotic platforms. These studies will motivate new hypothesis, experimentation and observation to uncover the unknown about natural designs and in turn inspire new ones. Like personalized software applications, physical machines can be personalized to interact and assist us in day-to-day tasks, as well as in emergency and exploration. With the emergence of machine learning and artificial intelligence, the millirobot collectives show promising prospects for large real-world data collection, for forecasting and also training new algorithms and designs by deploying them into diverse environments. Further developments in design methodologies and tools may finally merge the gap between software and robotic hardware to pave the way toward *consumer robotics*.

# Bibliography


[1] Sorger, D.M., 2015. Snap! Trap-jaw ants in Borneo also jump using their legs. Frontiers in Ecology and the Environment, 13(10), pp.574-575.

[2] Patek, S.N., Baio, J.E., Fisher, B.L. and Suarez, A.V. Multifunctionality and mechanical origins: ballistic jaw propulsion in trap-jaw ants. Proc. Nat. Acad. Sci., 103(34), pp.12787-12792 (2006).

[3] Larabee, F.J and Suarez, A.V. Mandible-powered escape jumps in trap-jaw ants increase survival rates during predator-prey encounters. PloS one 10 (5), e0124871 (2015).

[4] Jaeger, P. Cebrennus Simon, 1880 (Araneae: Sparassidae): a revisionary up-date with the description of four new species and an updated identification key for all species. Zootaxa, 3790(2), 319-356 (2014).

[5] Fearing, R. S. (2006, November). Challenges for Efffective Millirobots. In Micro-NanoMechatronics and Human Science, 2006 International Symposium on (pp. 1-5). IEEE.

[6] Kernbach, S., Häbe, D., Kernbach, O., Thenius, R., Radspieler, G., Kimura, T., & Schmickl, T. (2013). Adaptive collective decision-making in limited robot swarms without communication. The International Journal of Robotics Research, 32(1), 35-55.

[7] Werfel, J., Petersen, K. and Nagpal, R., 2014. Designing collective behavior in a termite-inspired robot construction team. Science, 343(6172), pp.754-758.

[8] Hu, W., Lum, G.Z., Mastrangeli, M. and Sitti, M., 2018. Small-scale soft-bodied robot with multimodal locomotion. Nature, 554(7690), p.81.

[9] Huang, H-W., Fazil Emre Uslu, Panayiota Katsamba, Eric Lauga, M. S. Sakar, and B. J. Nelson. "Adaptive locomotion of artificial microswimmers." Science advances 5, no. 1 (2019): eaau1532.

[10] Lock, R. J., Burgess, S. C., & Vaidyanathan, R. (2013). Multi-modal locomotion: from animal to application. Bioinspiration & biomimetics, 9(1), 011001.

[11] Bennet-Clark, H.C. The energetics of the jump of the locust Schistocerca gregaria. J. of Exp. Bio. 63(1), 53-83 (1975).

[12] Nabawy, M.R., Sivalingam, G., Garwood, R.J., Crowther, W.J., Sellers, W.I. Energy and time optimal trajectories in exploratory jumps of the spider Phidippus regius. Sci. Rep. 8(1), 7142 (2018).

[13] Kovac, M., Fuchs, M., Guignard, A., Zufferey, J.C. and Floreano, D., 2008, May. A miniature 7g jumping robot. In 2008 IEEE International Conference on Robotics and Automation (pp. 373-378). IEEE.

[14] Bergbreiter, S. (2008, September). Effective and efficient locomotion for millimeter-sized microrobots. In Intelligent Robots and Systems, 2008. IROS 2008. IEEE/RSJ International Conference on (pp. 4030-4035). IEEE.

[15] Haldane, D. W., Plecnik, M. M., Yim, J. K., Fearing, R. S. Robotic vertical jumping agility via series-elastic power modulation. Sci. Rob. 1 (1), eaag2048 (2016).

[16] Verbeek, Peter-Paul & Vermaas, Pieter E. (2012). Technological Artifacts. A Companion to the Philosophy of Technology. Wiley-Blackwell.

[17] Via, S., 1990. Ecological genetics and host adaptation in herbivorous insects: the experimental study of evolution in natural and agricultural systems. Annual review of entomology, 35(1), pp.421-446.

[18] Altenberg, L., 1995. Genome growth and the evolution of the genotype-phenotype map. In Evolution and biocomputation (pp. 205-259). Springer, Berlin, Heidelberg.

[19] Miki, N., Zhang, X., Khanna, R., Ayon, A.A., Ward, D. and Spearing, S.M., 2003. Multi-stack silicon-direct wafer bonding for 3D MEMS manufacturing. Sensors and Actuators A: Physical, 103(1-2), pp.194-201.

[20] Wood, R.J., Avadhanula, S., Sahai, R., Steltz, E. and Fearing, R.S., 2008. Microrobot design using fiber reinforced composites. Journal of Mechanical Design, 130(5), p.052304.

[21] Firouzeh, A., & Paik, J. (2015). Robogami: a fully integrated low-profile robotic origami. Journal of Mechanisms and Robotics, 7(2), 021009.

[22] Hawkes, E., B. An, N. M. Benbernou, H. Tanaka, S. Kim, E. D. Demaine, D. Rus, & R. J. Wood. "Programmable matter by folding." Proceedings of the National Academy of Sciences of the United States of America 107, no. 28 (2010): 12441-12445.

[23] Onal, C. D., Wood, R. J., & Rus, D. (2011, May). Towards printable robotics: Origami-inspired planar fabrication of three-dimensional mechanisms. InRobotics and Automation (ICRA), 2011 IEEE International Conference on (pp. 4608-4613). IEEE.

[24] Felton, S. M., Tolley, M. T., Onal, C. D., Rus, D., & Wood, R. J. (2013, May). Robot self-assembly by folding: A printed inchworm robot. In Robotics and Automation (ICRA), 2013 IEEE International Conference on (pp. 277-282). IEEE.

[25] An, B., & Rus, D. (2014). Designing and programming self-folding sheets.Robotics and Autonomous Systems, 62(7), 976-1001.

[26] Mao, Y., Yu, K., Isakov, M.S., Wu, J., Dunn, M.L. and Qi, H.J., 2015. Sequential self-folding structures by 3D printed digital shape memory polymers. Scientific reports, 5, p.13616.

[27] Tolley, M. T., Felton, S. M., Miyashita, S., Aukes, D., Rus, D., & Wood, R. J. (2014). Self-folding origami: shape memory composites activated by uniform heating. Smart Materials and Structures, 23(9), 094006.

[28] Felton, S., Tolley, M., Demaine, E., Rus, D., & Wood, R. (2014). A method for building self-folding machines. Science, 345(6197), 644-646.

[29] Soltero, D.E., Julian, B.J., Onal, C.D. and Rus, D., 2013, November. A lightweight modular 12-dof print-and-fold hexapod. In 2013 IEEE/RSJ International Conference on Intelligent Robots and Systems (pp. 1465-1471). IEEE.

[30] Bezzo, N., Mehta, A., Onal, C. D., & Tolley, M. T. (2015). Robot Makers: The Future of Digital Rapid Design and Fabrication of Robots. Robotics & Automation Magazine, IEEE, 22(4), 27-36.

[31] Onal, C. D., Wood, R. J., & Rus, D. (2013). An origami-inspired approach to worm robots. Mechatronics, IEEE/ASME Transactions on, 18(2), 430-438.

[32] Zhakypov, Z. and Paik, J., 2018. Design methodology for constructing multimaterial origami robots and machines. IEEE Transactions on Robotics, 34(1), pp.151-165.

[33] Paik, J., 2018. Soft robot design methodology for 'push-button'manufacturing. Nature Reviews Materials, 3(6), p.81.

[34] Marghitu, D.B., 2001. Mechanical engineer's handbook. Elsevier.

[35] Siciliano, B. and Khatib, O. eds., 2016. Springer handbook of robotics. Springer.

[36] Ha, S., Coros, S., Alspach, A., Kim, J. and Yamane, K., 2018. Computational co-optimization of design parameters and motion trajectories for robotic systems. The International Journal of Robotics Research, 37(13-14), pp.1521-1536.

[37] Huang, J.L., Zhakypov, Z., Sonar, H. and Paik, J., 2018. A reconfigurable interactive interface for controlling robotic origami in virtual environments. The International Journal of Robotics Research, 37(6), pp.629-647.

[38] Geilinger, M., Poranne, R., Desai, R., Thomaszewski, B. and Coros, S., 2018. Skaterbots: Optimization-based design and motion synthesis for robotic creatures with legs and wheels. ACM Transactions on Graphics (TOG), 37(4), p.160.

[39] Kriegman, S., Cheney, N. and Bongard, J., 2018. How morphological development can guide evolution. Scientific reports, 8(1), p.13934.

[40] Corucci, F., Cheney, N., Giorgio-Serchi, F., Bongard, J. and Laschi, C., 2018. Evolving soft locomotion in aquatic and terrestrial environments: effects of material properties and environmental transitions. Soft robotics, 5(4), pp.475-495.

[41] Cheney, N., Bongard, J., SunSpiral, V. and Lipson, H., 2018. Scalable co-optimization of morphology and control in embodied machines. Journal of The Royal Society Interface, 15(143), p.20170937.

[42] Fanuc (2019), M-2000iA/1200, URL: https://www.fanuc.eu/ch/en/robots/robot-filter-page/m-2000-series/m-2000ia-1200

[43] ABB (2019), ABB to build the world's most advanced robotics factory in Shanghai. URL: https://new.abb.com/news/detail/9412/abb-to-build-the-worlds-most-advanced-robotics-factory-in-shanghai.

[44] McGinn, C., Cullinan, M.F., Otubela, M. and Kelly, K., 2019. Design of a terrain adaptive wheeled robot for human-orientated environments. Autonomous Robots, 43(1), pp.63-78.

[45] Fankhauser, P. and Hutter, M., 2018. ANYmal: A Unique Quadruped Robot Conquering Harsh Environments. Research Features, (126), pp.54-57.

[46] Boussema, C., Powell, M.J., Bledt, G., Ijspeert, A.J., Wensing, P.M. and Kim, S., 2019. Online gait transitions and disturbance recovery for legged robots via the feasible impulse set. IEEE Robotics and Automation Letters, 4(2), pp.1611-1618.

[47] Chung, S.J., Paranjape, A.A., Dames, P., Shen, S. and Kumar, V., 2018. A survey on aerial swarm robotics. IEEE Transactions on Robotics, 34(4), pp.837-855.

[48] Tesla (2019), Semi truck, URL: https://www.tesla.com/semi

[49] El Wakil, S.D., 2019. Processes and design for manufacturing. CRC Press.

[50] Jung, G. P., Casarez, C. S., Jung, S. P., Fearing, R. S., & Cho, K. J. (2016, May). An integrated jumping-crawling robot using height-adjustable jumping module. In Robotics and Automation (ICRA), 2016 IEEE International Conference on (pp. 4680-4685). IEEE.

[51] Zhao, J., Yan, W., Xi, N., Mutka, M. W., & Xiao, L. (2014, May). A miniature 25 grams running and jumping robot. In Robotics and Automation (ICRA), 2014 IEEE International Conference on (pp. 5115-5120). IEEE.

[52] Zhang, Y., Zhang, L., Wang, W., Li, Y. and Zhang, Q., 2018. Design and Implementation of a Two-Wheel and Hopping Robot With a Linkage Mechanism. IEEE Access, 6, pp.42422-42430.

[53] Morrey, J. M., Lambrecht, B., Horchler, A. D., Ritzmann, R. E., & Quinn, R. D. (2003, October). Highly mobile and robust small quadruped robots. In Intelligent Robots and Systems, 2003.(IROS 2003). Proceedings. 2003 IEEE/RSJ International Conference on (Vol. 1, pp. 82-87). IEEE.

[54] Song, G., Yin, K., Zhou, Y. and Cheng, X., 2009. A surveillance robot with hopping capabilities for home security. IEEE Transactions on Consumer Electronics, 55(4), pp.2034-2039.

[55] Stoeter, S.A. and Papanikolopoulos, N., 2006. Kinematic motion model for jumping scout robots. IEEE transactions on robotics, 22(2), pp.397-402.

[56] Vaezi, M., Chianrabutra, S., Mellor, B., & Yang, S. (2013). Multiple material additive manufacturing–Part 1: a review: This review paper covers a decade of research on multiple material additive manufacturing technologies which can produce complex geometry parts with different materials. Virtual and Physical Prototyping, 8(1), 19-50.

[57] Shim, T. S., Kim, S. H., Heo, C. J., Jeon, H. C., & Yang, S. M. (2012). Controlled origami folding of hydrogel bilayers with sustained reversibility for robust microcarriers. Angewandte Chemie International Edition, 51(6), 1420-1423.

[58] Yun, D. and Fearing, R.S., 2019. Cockroach Milli-Robot With Improved Load Capacity. Journal of Mechanisms and Robotics, pp.1-12.

[59] Koh, J. S., & Cho, K. J. (2013). Omega-shaped inchworm-inspired crawling robot with large-index-and-pitch (LIP) SMA spring actuators. Mechatronics, IEEE/ASME Transactions on, 18(2), 419-429.

[60] Noh, M., Kim, S. W., An, S., Koh, J. S., & Cho, K. J. (2012). Flea-inspired catapult mechanism for miniature jumping robots. Robotics, IEEE Transactions on, 28(5), 1007-1018. Chicago

[61] Zhakypov, Z., Falahi, M., Shah, M., & Paik, J. (2015, September). The design and control of the multi-modal locomotion origami robot, Tribot. In Intelligent Robots and Systems (IROS), 2015 IEEE/RSJ International Conference on (pp. 4349-4355). IEEE.

[62] Paik, J. K., Byoungkwon, A., Rus, D., & Wood, R. J. (2012). Robotic Origamis: Self-morphing Modular Robot. In ICMC (No. EPFL-CONF-206919)

[63] Onal, C. D., Tolley, M. T., Wood, R. J., & Rus, D. (2015). Origami-inspired printed robots. IEEE/ASME Transactions on Mechatronics, 20(5), 2214-2221.

[64] Firouzeh, A., Salerno, M., & Paik, J. (2017). Stiffness Control With Shape Memory Polymer in Underactuated Robotic Origamis. IEEE Transactions on Robotics.

[65] Niiyama, R., Sun, X., Sung, C., An, B., Rus, D., & Kim, S. (2015). Pouch motors: Printable soft actuators integrated with computational design. Soft Robotics, 2(2), 59-70.

[66] Schulz, A., Sung, C., Spielberg, A., Zhao, W., Cheng, R., Grinspun, E., Rus, D. and Matusik, W., 2017. Interactive robogami: An end-to-end system for design of robots with ground locomotion. The International Journal of Robotics Research, 36(10), pp.1131-1147.

[67] Mehta, A., Bezzo, N., Gebhard, P., An, B., Kumar, V., Lee, I. and Rus, D., 2016. A design environment for the rapid specification and fabrication of printable robots. In Experimental Robotics (pp. 435-449). Springer, Cham.

[68] Sung, C., & Rus, D. (2015). Foldable joints for foldable robots. Journal of Mechanisms and Robotics, 7(2), 021012.

[69] Firouzeh, A., Mirrazavi Salehian, S. S., Billard, A., & Paik, J. (2015, May). An under actuated robotic arm with adjustable stiffness shape memory polymer joints. In Robotics and Automation (ICRA), 2015 IEEE International Conference on (pp. 2536-2543). IEEE.

[70] Paik, J. K., & Wood, R. J. (2012). A bidirectional shape memory alloy folding actuator. Smart Materials and Structures, 21(6), 065013.

[71] Firouzeh, A., & Paik, J. (2015). The design and modeling of a novel resistive stretch sensor with tunable sensitivity. IEEE Sensors Journal, 15(11), 6390-6398.

[72] Sreetharan, P.S., Whitney, J.P., Strauss, M.D. and Wood, R.J., 2012. Monolithic fabrication of millimeter-scale machines. Journal of Micromechanics and Microengineering, 22(5), p.055027.

[73] Felton, S. M., Tolley, M. T., Shin, B., Onal, C. D., Demaine, E. D., Rus, D., & Wood, R. J. (2013). Self-folding with shape memory composites. Soft Matter,9(32), 7688-7694.

[74] Paik, J. K., Hawkes, E., & Wood, R. J. (2010). A novel low-profile shape memory alloy torsional actuator. Smart Materials and Structures, 19(12), 125014.

[75] Shintake, J., Cacucciolo, V., Floreano, D. and Shea, H., 2018. Soft robotic grippers. Advanced Materials, 30(29), p.1707035.

[76] Belke, C.H. and Paik, J., 2017. Mori: a modular origami robot. IEEE/ASME Transactions on Mechatronics, 22(5), pp.2153-2164.

[77] W.M. Huang, Z. Ding, C.C. Wang, J. Wei, Y. Zhao, H. Purnawali, Shape memory materials, Materials Today, Volume 13, Issues 7–8, July–August 2010, Pages 54-61, ISSN 1369-7021.

[78] Zhakypov, Z., Huang, J. L., & Paik, J. (2016). A Novel Torsional Shape Memory Alloy Actuator: Modeling, Characterization, and Control. IEEE Robotics & Automation Magazine, 23(3), 65-74.

[79] Miyashita, S., Onal, C. D., & Rus, D. (2013, November). Self-pop-up cylindrical structure by global heating. In Intelligent Robots and Systems (IROS), 2013 IEEE/RSJ International Conference on (pp. 4065-4071). IEEE.

[80] Shin, B., Felton, S. M., Tolley, M. T., & Wood, R. J. (2014, May). Self-assembling sensors for printable machines. In Robotics and Automation (ICRA), 2014 IEEE International Conference on (pp. 4417-4422). IEEE.

[81] An, S.M., Ryu, J., Cho, M. and Cho, K.J., 2012. Engineering design framework for a shape memory alloy coil spring actuator using a static two-state model. Smart Materials and Structures, 21(5), p.055009.

[82] Sheng, J., & Desai, J. P. (2015). Design, modeling and characterization of a novel meso-scale SMA-actuated torsion actuator. Smart Materials and Structures, 24(10), 105005.

[83] Koh, J. S., Kim, S. R., & Cho, K. J. (2014, August). Self-folding origami using torsion shape memory alloy wire actuators. In ASME 2014 International Design Engineering Technical Conferences and Computers and Information in Engineering Conference (pp. V05BT08A043-V05BT08A043). American Society of Mechanical Engineers.

[84] Tobushi, H., Sakuragi, T., & Sugimoto, Y. (2008). Deformation and rotary driving characteristics of a shape-memory alloy thin strip element. Materials transactions, 49(1), 151-157.

[85] Ho, M., McMillan, A. B., Simard, J. M., Gullapalli, R., & Desai, J. P. (2012). Toward a meso-scale SMA-actuated MRI-compatible neurosurgical robot. Robotics, IEEE Transactions on, 28(1), 213-222.

[86] Yoshida, E., Murata, S., Kokaji, S., Kamimura, A., Tomita, K., & Kurokawa, H. (2002). Get back in shape![SMA self-reconfigurable microrobots]. Robotics & Automation Magazine, IEEE, 9(4), 54-60.

[87] Ryu, S. C., Quek, Z. F., Koh, J. S., Renaud, P., Black, R. J., Moslehi, B., ... & Cutkosky, M. R. (2015). Design of an Optically Controlled MR-Compatible Active Needle. Robotics, IEEE Transactions on, 31(1), 1-11.

[88] Ko, S. H., Bae, J. S., & Rho, J. H. (2014). Development of a morphing flap using shape memory alloy actuators: the aerodynamic characteristics of a morphing flap. Smart Materials and Structures, 23(7), 074015.

[89] Gilpin, K., Torres-Jara, E., & Rus, D. (2014). Controlling closed-chain robots with compliant SMA actuators: algorithms and experiments. In Experimental Robotics (pp. 149-163). Springer Berlin Heidelberg.

[90] Shim, J. E., Quan, Y. J., Wang, W., Rodrigue, H., Song, S. H., & Ahn, S. H. (2015). A smart soft actuator using a single shape memory alloy for twisting actuation. Smart Materials and Structures, 24(12), 125033.

[91] Shin, B. H., Jang, T., Ryu, B. J., & Kim, Y. (2015). A modular torsional actuator using shape memory alloy wires. Journal of Intelligent Material Systems and Structures.

[92] Liang, C., & Rogers, C. A. (1990). One-dimensional thermomechanical constitutive relations for shape memory materials. Journal of intelligent material systems and structures, 1(2), 207-234.

[93] Tanaka, K., Kobayashi, S., & Sato, Y. (1986). Thermomechanics of transformation pseudoelasticity and shape memory effect in alloys. International Journal of Plasticity, 2(1), 59-72.

[94] Brinson, L. C. (1993). One-dimensional constitutive behavior of shape memory alloys: thermomechanical derivation with non-constant material functions and redefined martensite internal variable. Journal of intelligent material systems and structures, 4(2), 229-242.

[95] Song, S.H., Lee, J.Y., Rodrigue, H., Choi, I.S., Kang, Y.J. and Ahn, S.H., 2016. 35 Hz shape memory alloy actuator with bending-twisting mode. Scientific reports, 6, p.21118.

[96] Zhakypov, Z., Belke, C.H. and Paik, J., 2017, September. Tribot: A deployable, self-righting and multi-locomotive origami robot. In 2017 IEEE/RSJ International Conference on Intelligent Robots and Systems (IROS) (pp. 5580-5586). IEEE.

[97] Salerno, M., Tognarelli, S., Quaglia, C., Dario, P., & Menciassi, A. (2013). Anchoring frame for intra-abdominal surgery. The International Journal of Robotics Research, 32(3), 360-370.

[98] Firouzeh, A., Sun, Y., Lee, H., & Paik, J. (2013, November). Sensor and actuator integrated low-profile robotic origami. In Intelligent Robots and Systems (IROS), 2013 IEEE/RSJ International Conference on (pp. 4937-4944). IEEE.

[99] Gosselin, C., Pelletier, F. & Laliberte, T., An anthropomorphic underactuated robotic hand with 15 dofs and a single actuator, IEEE International Conference on Robotics and Automation 2008, pp. 749-754.

[100] Catalano, M.G., Grioli, G., Farnioli, E., Serio, A., Piazza, C. & Bicchi, A., 2014. Adaptive synergies for the design and control of the Pisa/IIT SoftHand. The International Journal of Robotics Research, 33(5), pp.768-782.

[101] Firouzeh, A. & Paik, J., 2017. Grasp Mode and Compliance Control of an Underactuated Origami Gripper Using Adjustable Stiffness Joints. IEEE/ASME Transactions on Mechatronics, 22(5), pp.2165-2173.

[102] Brown, E., Rodenberg, N., Amend, J., Mozeika, A., Steltz, E., Zakin, M.R., Lipson, H. & Jaeger, H.M., 2010. Universal robotic gripper based on the jamming of granular material. Proceedings of the National Academy of Sciences, 107(44), pp.18809-18814.

[103] Kapadia, J. & Yim, M., Design and performance of nubbed fluidizing jamming grippers, IEEE International Conference on Robotics and Automation 2012, (pp. 5301-5306).

[104] Song, S., Drotlef, D.M., Majidi, C. & Sitti, M., 2017. Controllable load sharing for soft adhesive interfaces on three-dimensional surfaces. Proceedings of the National Academy of Sciences, p.201620344.

[105] Kessens, C.C. & Desai, J.P., 2011. A self-sealing suction cup array for grasping. Journal of Mechanisms and Robotics, 3(4), p.045001.

[106] Tai, K., El-Sayed, A.R., Shahriari, M., Biglarbegian, M. & Mahmud, S., 2016. State of the art robotic grippers and applications. Robotics, 5(2), p.11.

[107] Zhakypov, Z., Heremans, F., Billard, A. and Paik, J., 2018. An origami-inspired reconfigurable suction gripper for picking objects with variable shape and size. IEEE Robotics and Automation Letters, 3(4), pp.2894-2901.

[108] Elliott, T.J. & Staines, A.J., Harris-Intertype Corp, 1964. Sheet-gripping sucker. U.S. Patent 3,154,306.

[109] Rus, D. and Tolley, M.T., 2015. Design, fabrication and control of soft robots. Nature, 521(7553), p.467.

[110] Russo, S., Ranzani, T., Gafford, J., Walsh, C.J. and Wood, R.J., 2016, May. Soft pop-up mechanisms for micro surgical tools: Design and characterization of compliant millimeter-scale articulated structures. In Robotics and Automation (ICRA), 2016 IEEE International Conference on (pp. 750-757). IEEE.

[111] R. V. Martinez, C. R. Fish, X. Chen, & G. M. Whitesides, "Elastomeric origami: Programmable paper-elastomer composites as pneumatic actuators," Advanced Functional Materials, vol. 22, p. 13761384, 2012.

[112] Overvelde, J.T., De Jong, T.A., Shevchenko, Y., Becerra, S.A., Whitesides, G.M., Weaver, J.C., Hoberman, C. and Bertoldi, K., 2016. A three-dimensional actuated origami-inspired transformable metamaterial with multiple degrees of freedom. Nature communications, 7, p.10929.

[113] Li, S., Vogt, D.M., Rus, D. and Wood, R.J., 2017. Fluid-driven origami-inspired artificial muscles. Proceedings of the National Academy of Sciences, p.201713450.

[114] Zhakypov, Z., Mete, M., Fiorentino, J. and Paik, J., 2019, April. Programmable Fluidic Networks Design for Robotic Origami Sequential Self-Folding. In 2019 2nd IEEE International Conference on Soft Robotics (RoboSoft) (pp. 814-820). IEEE.

[115] Hibbeler, R.C. and Kiang, T., 2015. Structural analysis. Pearson Prentice Hall.

[116] Miyashita, S., Guitron, S., Li, S., & Rus, D. Robotic metamorphosis by origami exoskeletons. Science Robotics, Vol. 2, Issue 10, 2017.

[117] E.D. Demaine, M.L. Demaine, & J.S.B. Mitchell, Folding flat silhou- ettes and wrapping polyhedral packages: New results in computational origami, Computational Geometry : Theory and Applications, vol. 16(1), 2000, pp. 3-21.

[118] Demaine, E. D., Demaine, M. L., & Rus, D. Edge-Compositions of 3D Surfaces.

[119] Cai, J., Qian, Z., Jiang, C., Feng, J., & Xu, Y. (2016). Mobility and Kinematic Analysis of Foldable Plate Structures Based on Rigid Origami. Journal of Mechanisms and Robotics, 8(6), 064502.

[120] Chen, Y., Peng, R., & You, Z. (2015). Origami of thick panels. Science, 349(6246), 396-400.

[121] Hernandez, E. A. P., Hartl, D. J., & Lagoudas, D. C. (2016). Kinematics of Origami Structures With Smooth Folds. Journal of Mechanisms and Robotics, 8(6), 061019.

[122] Doshi, N., Goldberg, B., Sahai, R., Jafferis, N., Aukes, D., Wood, R. J., & Paulson, J. A. (2015, September). Model driven design for flexure-based Microrobots. In Intelligent Robots and Systems (IROS), 2015 IEEE/RSJ International Conference on (pp. 4119-4126). IEEE.

[123] Yim, S., Miyashita, S., Rus, D., & Kim, S. (2017). Teleoperated Micromanipulation System Manufactured by Cut-and-Fold Techniques. IEEE Transactions on Robotics, 33(2), 456-467.

[124] Faal, S. G., Chen, F., Tao, W., Agheli, M., Tasdighikalat, S., & Onal, C. D. (2016). Hierarchical kinematic design of foldable hexapedal locomotion platforms. Journal of Mechanisms and Robotics, 8(1), 011005.

[125] Delimont, I. L., Magleby, S. P., & Howell, L. L. (2015). Evaluating compliant hinge geometries for origami-inspired mechanisms. Journal of Mechanisms and Robotics, 7(1), 011009.

[126] Nelson, T. G., Lang, R. J., Pehrson, N. A., Magleby, S. P., & Howell, L. L. (2016). Facilitating deployable mechanisms and structures via developable lamina emergent arrays. Journal of Mechanisms and Robotics, 8(3), 031006.

[127] Kim, J., Lee, D. Y., Kim, S. R., and Cho, K. J. (2015, May). A self-deployable origami structure with locking mechanism induced by buckling effect. In Robotics and Automation (ICRA), 2015 IEEE International Conference on (pp. 3166-3171). IEEE.

[128] S. T. Kalat, S. G. Faal, U. Celik and C. D. Onal, "TriBot: A minimally-actuated accessible holonomic hexapedal locomotion platform," 2015 IEEE/RSJ International Conference on Intelligent Robots and Systems (IROS), Hamburg, 2015, pp. 6292-6297.

[129] Tachi, T., & Hull, T. C. (2017). Self-Foldability of Rigid Origami. Journal of Mechanisms and Robotics, 9(2), 021008.

[130] Sun, X., Felton, S. M., Niiyama, R., Wood, R. J., & Kim, S. (2015, May). Self-folding and self-actuating robots: a pneumatic approach. In 2015 IEEE International Conference on Robotics and Automation (ICRA) (pp. 3160-3165). IEEE.

[131] Firouzeh, A., Amon-Junior, A. F., & Paik, J. (2015). Soft piezoresistive sensor model and characterization with varying design parameters. Sensors and Actuators A: Physical, 233, 158-168.

[132] Sun, X., Felton, S. M., Wood, R. J., & Kim, S. (2015, September). Printing angle sensors for foldable robots. In Intelligent Robots and Systems (IROS), 2015 IEEE/RSJ International Conference on (pp. 1725-1731). IEEE.

[133] Paik, J. K., Kramer, R. K., & Wood, R. J. (2011, September). Stretchable circuits and sensors for robotic origami. In 2011 IEEE/RSJ International Conference on Intelligent Robots and Systems (pp. 414-420). IEEE.

[134] R. K. Kramer, C. Majidi, R. Sahai & R. J. Wood, "Soft curvature sensors for joint angle proprioception," 2011 IEEE/RSJ International Conference on Intelligent Robots and Systems, San Francisco, CA, 2011, pp. 1919-1926.

[135] Felton, S. M., Becker, K. P., Aukes, D. M., & Wood, R. J. (2015). Self-folding with shape memory composites at the millimeter scale. Journal of Micromechanics and Microengineering, 25(8), 085004.

[136] Salerno, M., Firouzeh, A., & Paik, J. (2017). A Low Profile Electromagnetic Actuator Design and Model for an Origami Parallel Platform. Journal of Mechanisms and Robotics, 9(4), 041005.

[137] Shigemune, H., Maeda, S., Hara, Y., Hosoya, N., & Hashimoto, S. (2016). Origami Robot: A Self-Folding Paper Robot With an Electrothermal Actuator Created by Printing. IEEE/ASME Transactions on Mechatronics, 21(6), 2746-2754.

[138] Muth, J. T., Vogt, D. M., Truby, R. L., Mengüç, Y., Kolesky, D. B., Wood, R. J., & Lewis, J. A. (2014). Embedded 3D Printing of Strain Sensors within Highly Stretchable Elastomers. Advanced Materials.

[139] Aukes, D. M., Goldberg, B., Cutkosky, M. R., & Wood, R. J. (2014). An analytic framework for developing inherently-manufacturable pop-up laminate devices.Smart Materials and Structures, 23(9), 094013.

[140] Hoover, A. M., & Fearing, R. S. (2008, May). Fast scale prototyping for folded millirobots. In Robotics and Automation, 2008. ICRA 2008. IEEE International Conference on (pp. 886-892). IEEE.

[141] Wood, R. J. (2008). The first takeoff of a biologically inspired at-scale robotic insect. IEEE Transactions on Robotics, 24(2), 341-347.

[142] Chen, Y., Wang, H., Helbling, F., Jafferis, N. T., Zufferey, R., Ong, A., Ma, K., Gravish, N., Chirarattananon, P., Kovac, M., & Wood, R. J., A biologically inspired, flapping-wing, hybrid aerial-aquatic microrobot. Science Robotics, Vol. 2, Issue 11, 2017.

[143] Li, C., Pullin, A. O., Haldane, D. W., Lam, H. K., Fearing, R. S., & Full, R. J. (2015). Terradynamically streamlined shapes in animals and robots enhance traversability through densely cluttered terrain. Bioinspiration and biomimetics, 10(4), 046003.

[144] Linthorne, N. P. (2001). Analysis of standing vertical jumps using a force platform. American Journal of Physics, 69(11), 1198-1204.

[145] Heyman, Y., Shental, N., Brandis, A., Hefetz, A., Feinerman, O. Ants regulate colony spatial organization using multiple chemical road-signs. Nature com., 8, p.15414 (2017). 2. Gordon, D. M. The ecology of collective behavior. PLoS Bio., 12, e1001805 (2014).

[146] Gordon, D. M. The ecology of collective behavior. PLoS Bio., 12, e1001805 (2014).

[147] Franks, N. R. and Richardson, T. Teaching in tandem-running ants. Nature, 439(7073), p.153 (2006).

[148] Sorger, D.M. and Zettel, H. On the ants (Hymenoptera: Formicidae) of the Philippine Islands: V. The genus Odontomachus LATREILLE, 1804. Myrmecological News, 14(14), pp.141-163 (2011).

[149] Rubenstein, M., Cornejo, A., Nagpal, R. Programmable self-assembly in a thousand-robot swarm. Science 345, 795-799 (2014).

[150] Arvin, F., Murray, J., Zhang, C., Yue, S. Colias: an autonomous micro robot for swarm robotic applications. Int. J. of Adv. Rob. Sys. 11, 113 (2014).

[151] Pickem, D., Glotfelter, P., Wang, L., Mote, M., Ames, A., Feron, Egerstsedt, M. The Robotarium: A remotely accessible swarm robotics research testbed. IEEE Rob. Autom. (2016).

[152] Weston-Dawkes, W.P., Ong, A.C., Majit, M. R. A., Joseph, F., Tolley, M. T. Towards rapid mechanical customization of cm-scale self-folding agents. IEEE Intel. Rob. Sys. 4312-4318 (2017).

[153] Kim, Y., Yuk, H., Zhao, R., Chester, S.A. and Zhao, X. Printing ferromagnetic domains for untethered fast-transforming soft materials. Nature, 558(7709), p.274 (2018).

Ce document a été imprimé au Centre d'impression EPFL,
imprimerie climatiquement neutre, certifiée myClimate.